UNIVERSITY OF SOUTHAMPTON

THE STRUCTURE AND PROPERTIES OF SOME INORGANIC PROTON CONDUCTORS

A thesis submitted in partial fulfilment of the requirements for the degree of Doctor of Philosophy

by

ROBERT GLADSTONE BELL

Chemistry Department

University of Southampton

January 1990

CONTENTS

Chapter 4: Structure of Cubic $HSbO_3.xH_2O$

Chapter 5: Quasielastic Neutron Scattering Study of Some Protonic Materials

Chapter 6: Miscellaneous Ion-Exchange and Intercalation Reactions

Part A: Ion-Exchange of Antimonophosphates

Part B: Intercalation Reactions of $MoO_2HPO_4.H_2O$

UNIVERSITY OF SOUTHAMPTON

ABSTRACT

FACULTY OF SCIENCE
CHEMISTRY

Doctor of Philosophy

THE STRUCTURE AND PROPERTIES OF SOME INORGANIC PROTON CONDUTORS

by Robert Gladstone Bell

Studies are presented on a range of proton-containing inorganic oxides and phosphates. Of primary concern is the structure of such materials, particularly the location of protonic species with respect to the oxide frameworks, and the relationship between structure and the mobility of protons which gives rise to conduction. Powder neutron diffraction (PND) was used accurately to locate deuterium atoms, substituted for hydrogen in the studied materials. Compounds were also characterised by powder x-ray diffraction, thermogravimetric analysis, infrared spectroscopy (IR) and nuclear magnetic resonance (NMR). Quasielastic neutron scattering (QENS) was used to study proton dynamics.

A fully deuterated sample of the chain-structured compound $MoO_2HPO_4.H_2O$ was prepared and its structure determined by PND. The material was found to possess an acidic P–O–H group and a water molecule coordinated to the octahedral Mo, in contradiction to a previous model, with the chains bound together by a network of hydrogen bonds. NMR and IR data were consistent with this structure. A.c. techniques yielded a conductivity for this compound of the order of $10^{-5}\,(\Omega cm)^{-1}$.

The structure of the proton-conducting cubic polymorph of $HSbO_3.xH_2O$ was determined by the same method. The 'water' was found to be situated on two distinct sites within cavities formed by the antimonate framework, on one site as H_3O^+ and on the other as H_2O associated with a framework-bound proton. It is proposed that a network of hydrogen bonds and the structural disorder of the material both contribute to proton mobility.

A preliminary study of proton diffusion in cubic $HSbO_3.xH_2O$ and in a series of hydrated and ammonia-containing defect pyrochlores was performed by QENS. For $HSbO_3.xH_2O$, $NH_4HTa_2O_6$ and NH_4TaWO_6 fast dynamic processes on the timescale 10^{-10}s were observed whereas for the hydrated analogues of the last two compounds no process was observed on this timescale. This is consistent with the more restricted rotational freedom of H_2O in the pyrochlore cavity.

$HSb_2PO_8.xH_2O$ was prepared by ion exchange of KSb_2PO_8 and characterised. However $HSbP_2O_8.xH_2O$, known to be a poor bulk conductor, could not be prepared by ion exchange.

Reactions between $MoO_2HPO_4.H_2O$ and a series of organic amines were studied. Characterisation of the products was difficult, but it is thought that a 1:1 intercalation compound with n-ethylamine was prepared as an impure phase.

ACKNOWLEDGEMENTS

I should like first to record my gratitude to Dr M.T. Weller for his supervision and guidance during the period of my studentship.

Next I thank the many members of the inorganic community at Southampton who have at various times offered advice or assistance, whether solicited or otherwise, mentioning particularly my colleagues in the "Weller group": John Grasmeder, Gordon Wong and Dean Lines. Acknowledgement is also due to Professor I.R. Beattie, who first brought me to Southampton.

For the provision of financial resources I am grateful to the Science and Engineering Research Council and to Mr and Mrs L.G. Bell.

For sharing a roof with me for most of my time at Southampton, and providing an agreeable domestic environment, I thank Drs Keith Whiston, Andrew Foakes and Robin Forster.

Finally I thank Professor C.R.A. Catlow for his tolerance during the preparation of this thesis.

CHAPTER 1

INTRODUCTION

1.1 Framework Oxides and Hydroxides [1]

Examples of the variety of structures adopted by the oxides of high oxidation state metals may be found among the ternary oxides $A_xB_yO_z$ where A is a mono- or divalent cation and B is a transition element or metal such as antimony or lead, and among more complex oxides containing two types of "B" atom.

For the stoichiometry ABO_3 the most common structure is the perovskite where the A and B atoms form a body-centred cubic lattice and the O atoms occupy sites along the cell edges such that B is octahedrally coordinated, as shown in figure 1.1a (data taken from structure of $SrTiO_3$ by Hutton & Nelmes[2]). This structure is found in compounds such as $LaMnO_3$, $BaZrO_3$ and $SrTiO_3$ and in various distorted forms as in $KTaO_3$, $BaTiO_3$ and others. In the ilmenite structure (named after $FeTiO_3$) the A and B atoms occupy similar octahedral sites in the hexagonal close-packed oxygen array but these sites are segregated so as to give alternate layers of A and B atoms, perpendicular to the hexagonal *c*-axis.

It is often convenient to describe complex structures in terms of linked MO_x polyhedra which form the structural frameworks. Thus in figure 1.1b, the perovskite structure is shown to be made up of a regular three-dimensional framework of BO_6 octahedra linked by vertex-sharing (i.e. the ReO_3 structure) with the A atoms occupying the 12-coordinate interstices between the octahedra. A third ABO_3 structure, the defect pyrochlore, is shown in figure 1.2 (data from Dickens & Weller[3]) as a framework of vertex-sharing BO_6 octahedra which contains large cavities of tetrahedral symmetry, linked by hexagonal channels. These channels contain the A cations. This

(a)

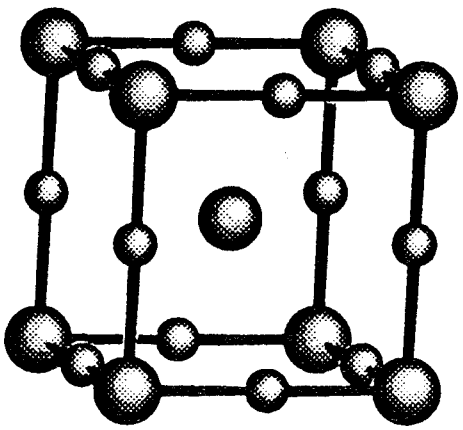

(b)

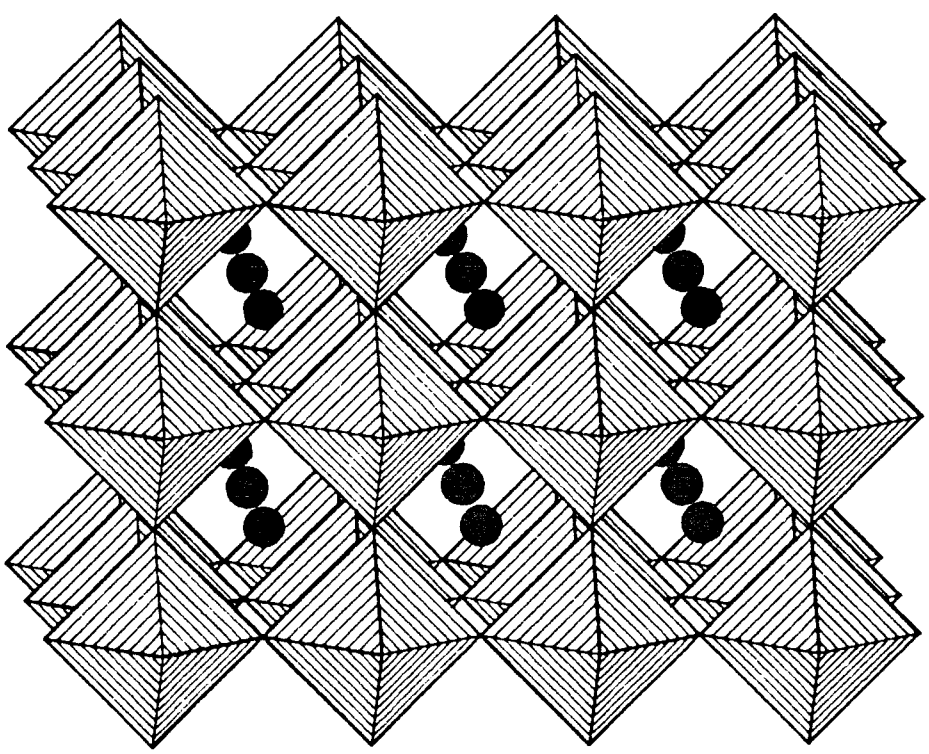

Figure 1.1 The perovskite structure of $SrTiO_3$: (a) the unit cell with Ti at the primitive lattice points, O at the centres of the cell edges and Sr at the body-centred position; (b) polyhedral representation with vertex-sharing TiO_6 octahedra and interstitial Sr atoms.

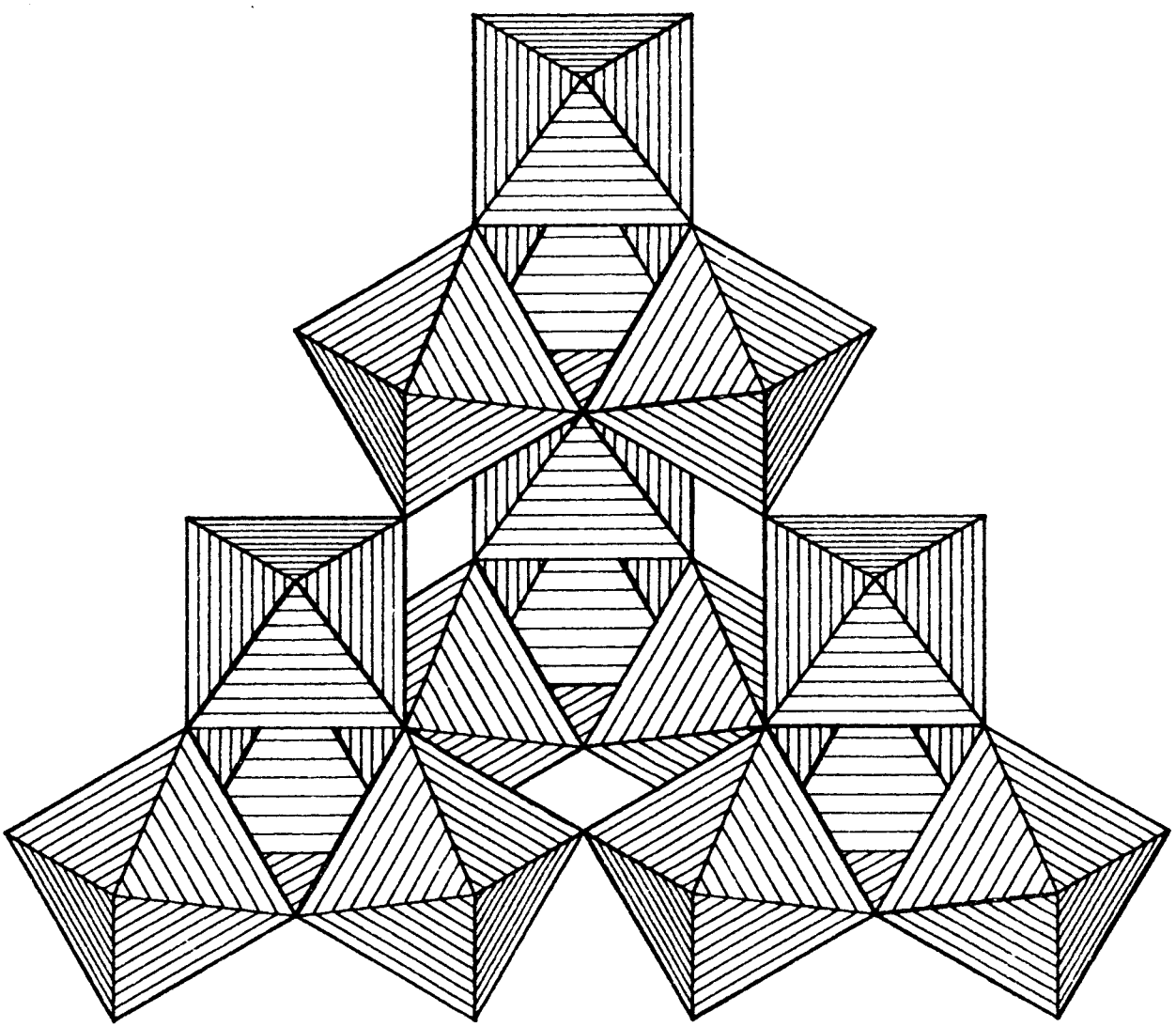

Figure 1.2 Polyhedral representation of the defect pyrochlore structure showing the large tetrahedral cavity.

cubic structure (space group Fd3m), exhibited by $TlTaO_3$, $TlNbO_3$, $KTaWO_3$ and others, is related to the "true" pyrochlore structure by the removal of an oxygen atom from the 8b site at the centre of the cavity. The terms "pyrochlore" and "defect pyrochlore" are however both commonly used in reference to the latter structure.

The compound $KSbO_3$ is known to form three different structures, dependent on the method of preparation[4]. Two of these are the ilmenite and defect pyrochlore. The third is so far unique to $KSbO_3$ and consists, as shown in figure 1.3, of pairs of edge-sharing SbO_6 octahedra with these pairs being themselves linked by vertex-sharing into a three-dimensional SbO_3^- framework. The framework defines a network of intersecting channels which extend in three dimensions diagonally through the cubic (Im3) unit cell. These linear tunnels, in which the K^+ species are located, are illustrated in figure 1.4.

These ABO_3 framework structures are all three-dimensional. However two and one-dimensional framework structures also exist where layers or chains of BO_x oxide are linked to each other only by the more ionic interaction with "A" cations or by hydrogen bonding in the case of hydroxy-containing and hydrated materials. Examples of layered oxides are found among the titanates such as $K_2Ti_2O_5$[5] and $KTiNbO_5$[6]. $K_2Ti_2O_5$ is characterised by 5-coordination of Ti in the $(Ti_2O_5^{2-})_n$ layers. The distorted TiO_5 trigonal bipyramids are linked by edge and vertex-sharing into a two-dimensional framework, with the planes of three "equatorial" oxygens lying perpendicular to the layers. The potassiums are located on 8-coordinate sites between the layers. In figure 1.5 it can be seen that $KTiNbO_5$ has layers made up of pairs of edge-sharing octahedra with the pairs linked by vertex-sharing into a zig-zag pattern. K^+ ions occupy the the interlayer region. Amongst oxyhydroxides many examples of layer structure are found of which that of β-$UO_2(OH)_2$[7] is illustrated in

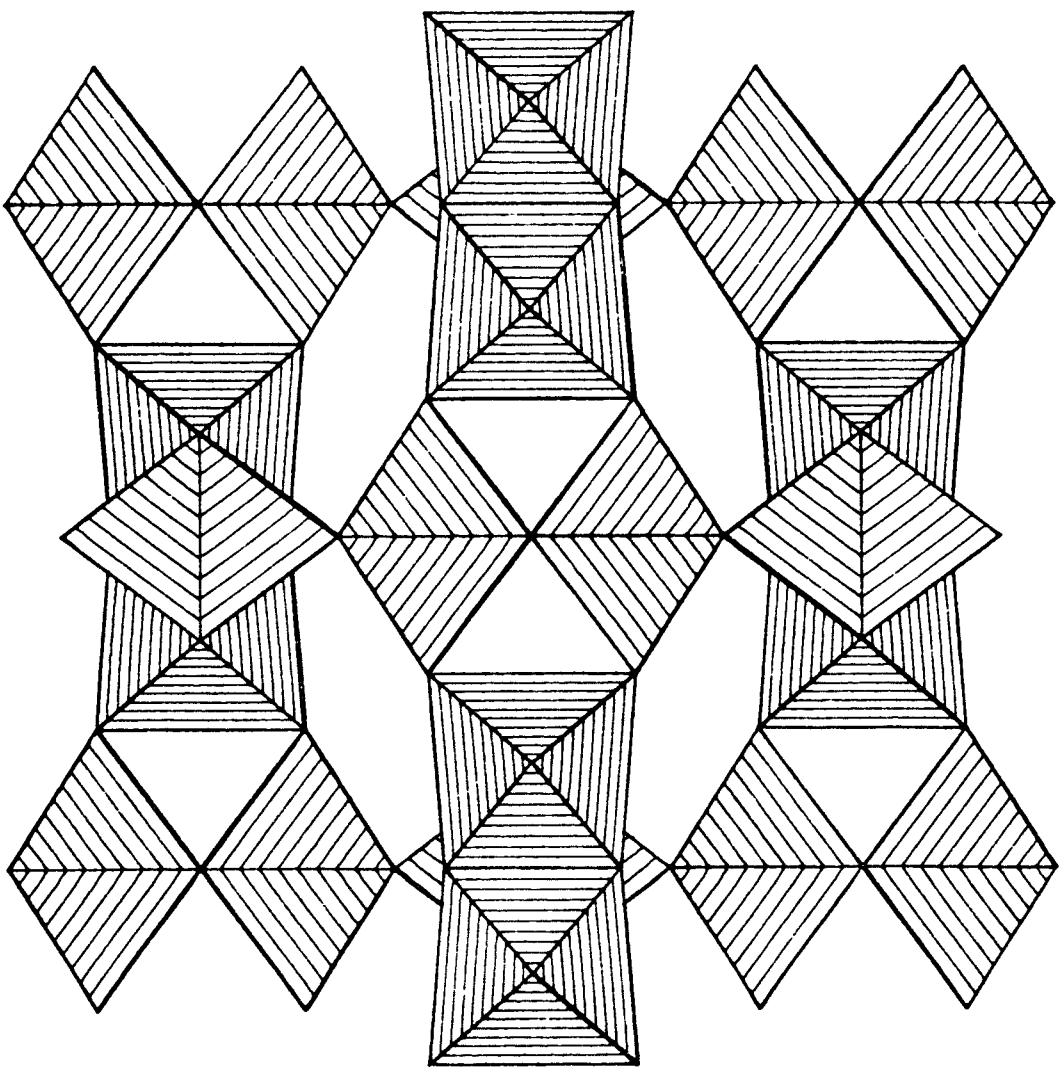

Figure 1.3 [100] Projection of the framework structure of cubic $KSbO_3$.

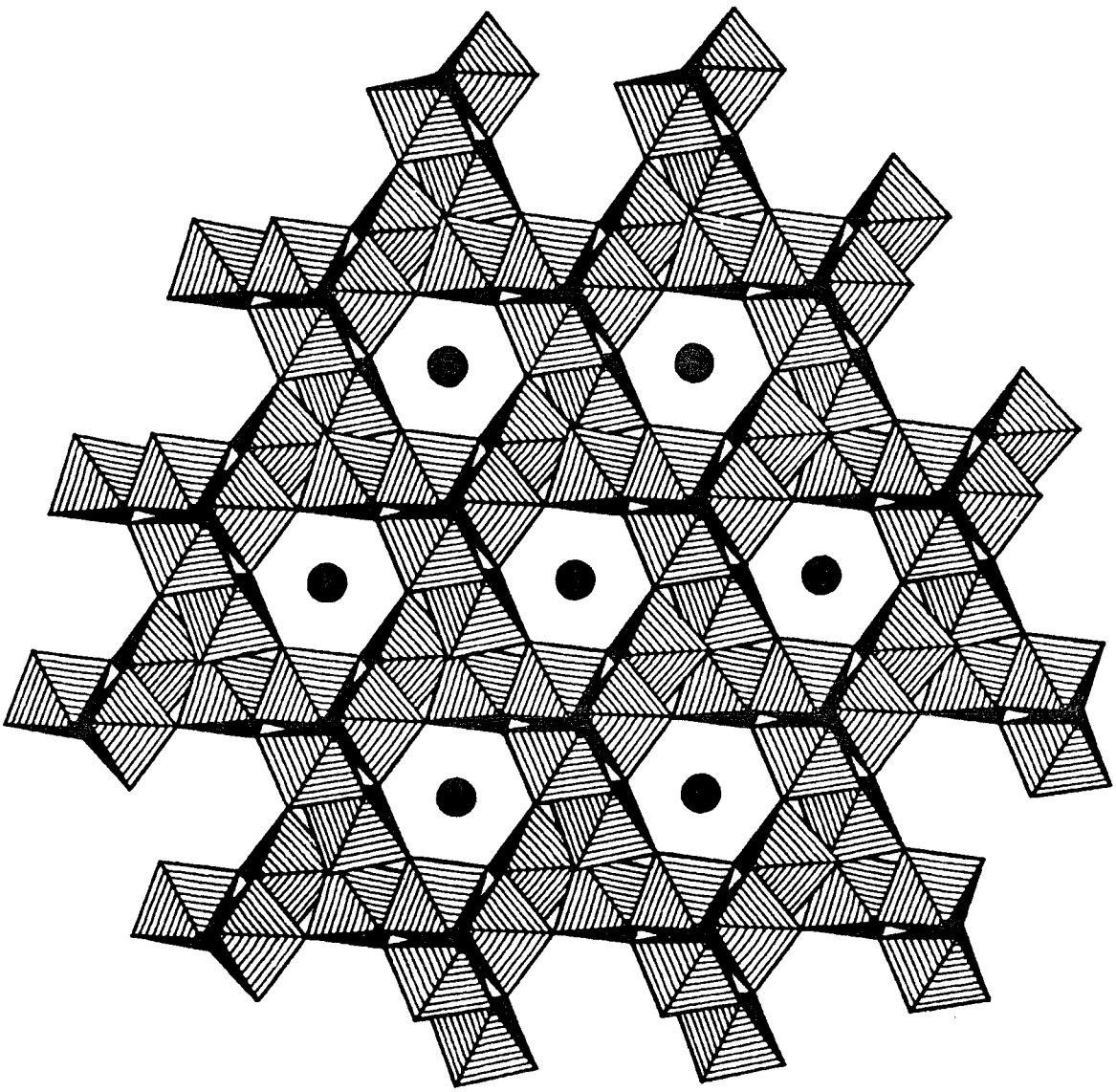

Figure 1.4 [111] Projection of the structure of cubic $KSbO_3$ showing the linear tunnels, with K represented as filled circles.

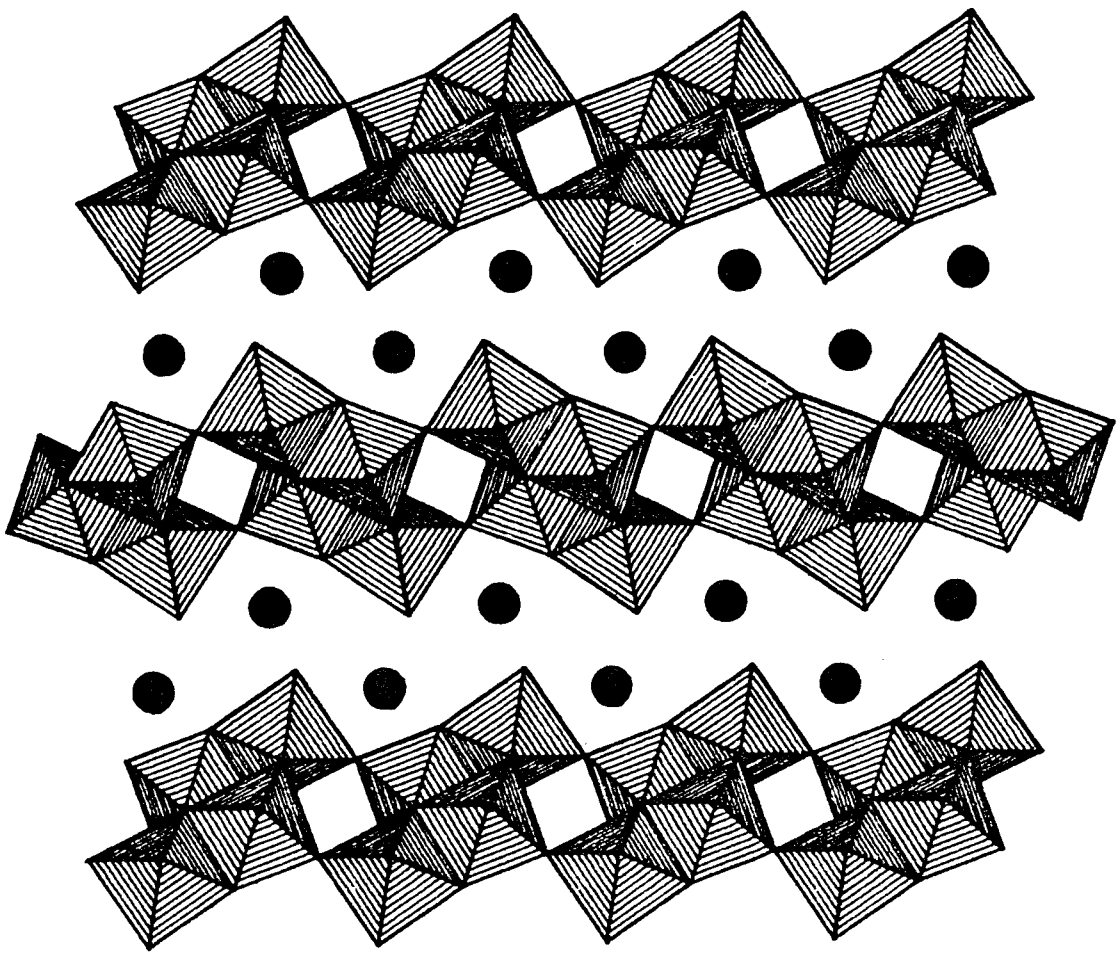

Figure 1.5 The structure of $KTiNbO_5$ viewed parallel to the layers, with potassiums represented as filled circles.

figure 1.6. This structure consists of buckled layers of vertex-sharing UO_6 with the shared OH groups projecting into the interlayer region towards unshared oxygens in the adjacent layer and linking the structure by hydrogen bonding.

One-dimensional, or chain, structures are less common among oxides. An interesting example however is that of $K_2Mo_3O_{10}$ which is thought of as containing both MoO_4 and MoO_6 groups[8,9]. Each octahedron is linked to its neighbour by two bridging tetrahedra which share adjacent vertices of the octahedra. However this structure should properly be described as having 5 and 6–coordinate molybdenum since the "tetrahedral" Mo shares an additional oxygen, forming a very distorted trigonal bipyramid. The Mo–O distances in this compound vary considerably with unshared M–O lying between 1.64 and 1.71 Å and shared Mo–O between 1.90 and 2.14 Å. The longest distance is between octahedral Mo and the "fifth" oxygen. In figure 1.7 it can be seen that the structure of $MoO_2HPO_4.H_2O$ is made up of double chains of linked MoO_6 octahedra and PO_4 tetrahedra thus forming a one-dimensional "framework". This structure is discussed further in chapter 3.

1.2 Framework Phosphates

Closely related to the oxides described above are framework phosphates of the type $A_xB_yP_wO_z$ and hydroxy-containing analogues. Although $MoO_2HPO_4.H_2O$ has already been mentioned, phosphates are for convenience discussed here. The three-dimensional structure of KSb_2PO_8, one of a series of antimonophosphates recently synthesised by Piffard and co-workers, is built up from SbO_6 octahedra sharing edges or vertices and PO_4 tetrahedra sharing corners with the octahedra such that there are no unshared oxygens[10]. The P–O bond distances lie between 1.51 and 1.56 Å. The framework defines a network of intersecting channels (figure 1.8) in which the potassium ions are located, on sites which are not associated with a particular framework

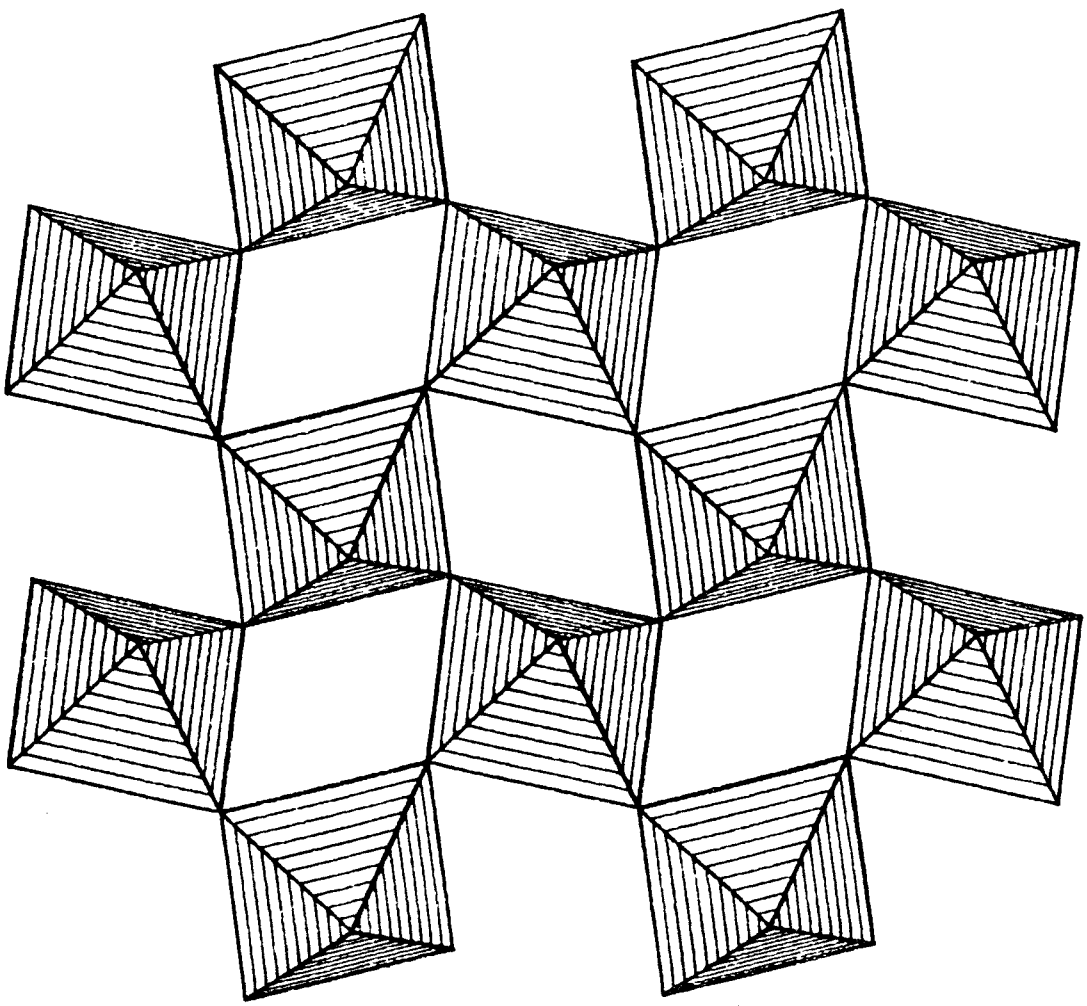

Figure 1.6 A layer of the structure of β–$UO_2(OH)_2$ showing the buckled configuration of UO_6 octahedra. The hydrogens (not shown) are bound to the unshared vertices of the octahedra.

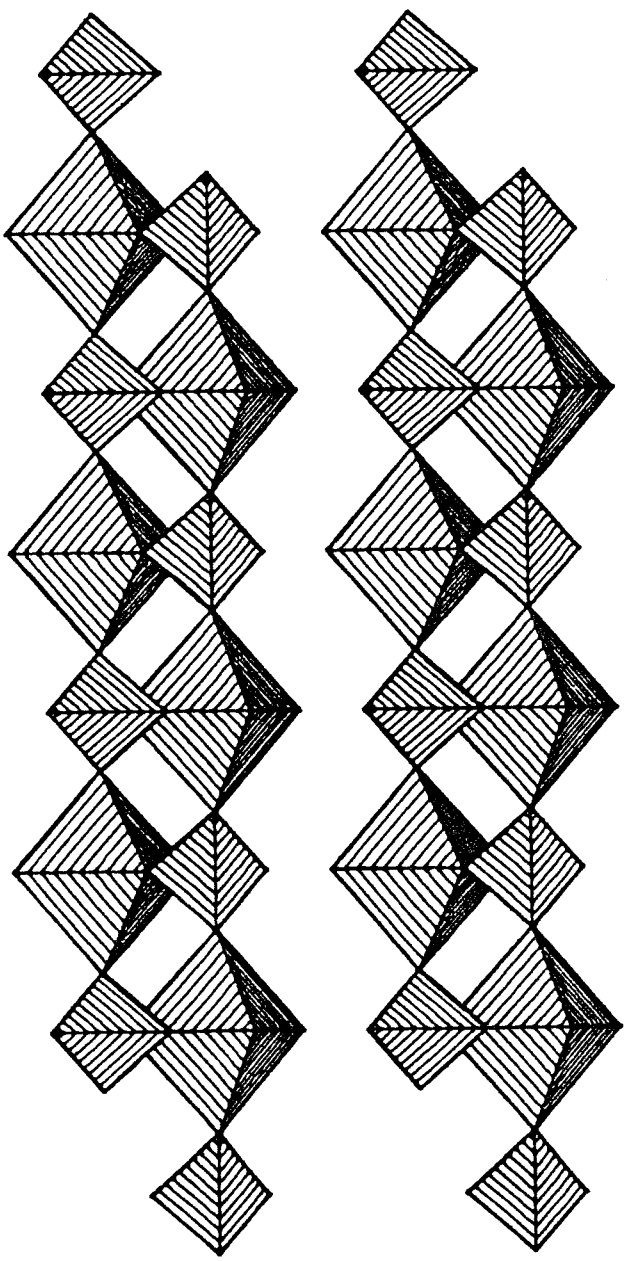

Figure 1.7 The framework structure of $MoO_2HPO_4.H_2O$ showing two of the $MoPO_7$ double chains.

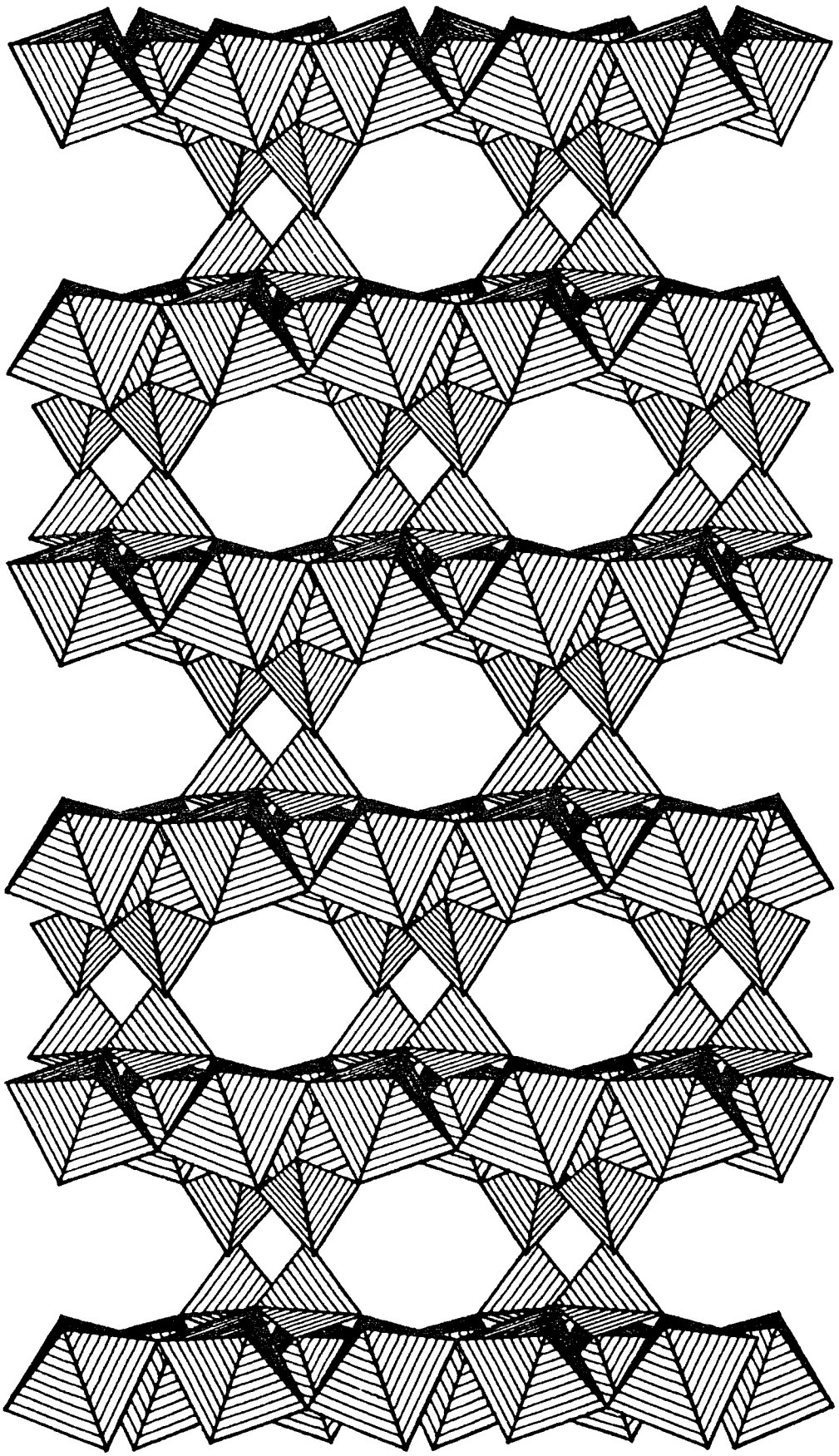

Figure 1.8 The framework structure of KSb_2PO_8 showing the linear tunnels in which the potassiums (not shown) are located.

oxygen. The analogous compound $K_5Sb_5P_2O_{20}$[11] possesses a more complex three-dimensional framework with SbO_6 octahedra sharing edges or vertices and three types of PO_4 tetrahedra sharing respectively four, three and two vertices with the octahedra. The location of the last type of tetrahedron, which protrudes into the large cavity, defines the positions of the potassium ions.

$KSbP_2O_8$[12] possesses a two-dimensional structure consisting of infinite $(SbP_2O_8^-)_n$ layers made from SbO_6 octahedra sharing each of their vertices with a PO_4 tetrahedron, with the layers lying perpendicular to the crystallographic *c*-axis, as may be seen in figure 1.9. Each tetrahedron has three shared oxygens (P–O distance 1.56 Å) and one unshared (P–O 1.47 Å) which points into the interlayer space, with the K^+ ions lying between these layers in such a way that each is octahedrally coordinated to six of the unshared oxygen atoms. The other layered compound in this family of antimonophosphates, $K_3Sb_3P_2O_{14}$, has a more open structure[13], with the polyhedra linked only by vertex-sharing. Not only is there a large interlayer region containing the potassiums but the layers themselves contain hexagonal channels, parallel with the *c*-axis, with a channel width of about 5 Å.

Yet another antimonophosphate, K_2SbPO_6, forms a one-dimensional structure[14]. The infinite chains consist of a single string of edge-sharing SbO_6 octahedra with the PO_4 tetrahedra bridging the unshared vertices of adjacent octahedra, and disposed on opposite sides of the chain in a staggered configuration. In this compound the potassium ions are distinctly coordinated to one of the unshared phosphate oxygens.

Many examples of framework molybdenophosphates are also found, with all the common oxidation states of molybdenum represented. For example the Mo(VI) compound $NaMoO_2PO_4$[15] possesses a three-dimensional framework of vertex-sharing octahedra and tetrahedra with infinite chains of alternating MoO_6 and PO_4 units

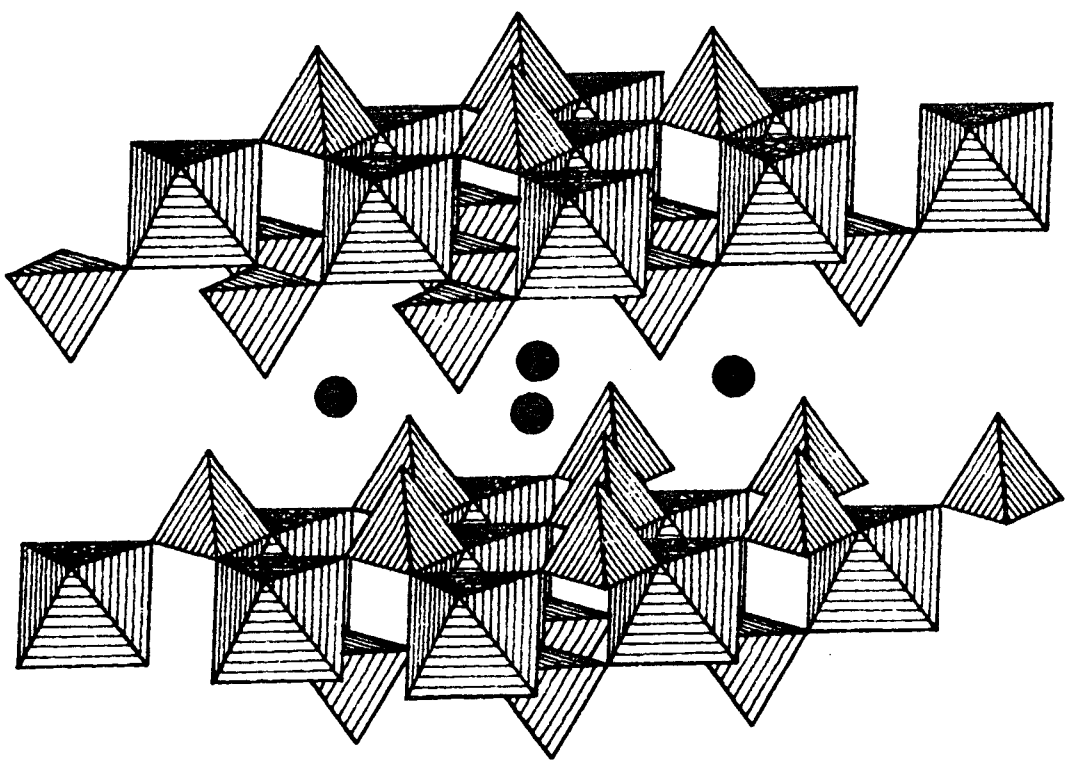

Figure 1.9 Two layers of the structure of $KSbP_2O_8$, with four of the interlayer potassium atoms shown.

along the *z*–direction being further linked to neighbouring chains by bonds in the *xy* plane. Although phosphorus shares all four oxygens with molybdenum, the coordination tetrahedra are somewhat distorted with P–O bonds in the range 1.48 to 1.63 Å. Within the MoO_6 octahedra shared Mo–O bond distances are between 1.91 and 2.17 Å and unshared in the range 1.78 to 1.97 Å.

The molybdenum(V) compound $K_4Mo_8P_{12}O_{52}$[16] has a tunnel structure defined by a network of vertex-sharing octahedra and tetrahedra. Half of the PO_4 groups in this case are linked to each other to form P_2O_7 units. A tendency towards 5-coordination is exhibited by molybdenum, which occupies an off-centre position in the otherwise fairly regular MoO_6 octahedron. Four of the Mo–O bonds are between 1.98 and 2.05 Å in length. The remaining two oxygens, which lie *trans* to each other in the octahedron are situated at distances of 1.66 Å (the only unshared oxygen) and 2.28 Å from Mo. Potassium is found on 8-coordinate sites in the linear tunnels.

$TlMo_2P_3O_{12}$ also possesses a tunnel structure[17], with the framework made up entirely of vertex-sharing polyhedra. In this Mo(IV) compound, however, a higher degree of connectivity is observed with molybdenum sharing all its oxygens, five with phosphorus (Mo–O in the range 2.02 to 2.05 Å) and one with a neighbouring molybdenum (Mo–O 1.85 Å) such that the MoO_6 octahedra are linked in pairs.

Among hydroxy-containing phosphates which fall into the present terms of reference are the two well-studied compounds $HUO_2PO_4.4H_2O$ (HUP) and $Zr(HPO_4)_2.H_2O$ (α-ZrP). In HUP[18], the layers comprise a framework of linear UO_2^{2+} groups linked to the PO_4^{3-} tetrahedra with the water molecules themselves forming two-dimensional networks between the layers. α-ZrP has layers containing a fairly regular corner-sharing arrangement of ZrO_6 and PO_4 units[19].

1.3 Ion Exchange and Hydrated Materials

A feature of many of the framework oxides and phosphates mentioned above is that they undergo ion-exchange reactions in acidic media whereby the non-framework cations are replaced by protons to form oxyhydroxides. For example a ternary oxide may undergo the following:

$$A_xB_yO_z + xH^+ \rightarrow B_yO_{(z-x)}(OH)_x + xA^+.$$

Often the reaction is accompanied by hydration such that water molecules from the acidic solution are included in the channels of the material. Usually the degree of hydration is temperature-dependent with partial or complete dehydration occurring on heating the exchange product, without destroying the framework structure. Compounds containing potassium, thallium and to a lesser extent sodium are particularly suited to this form of exchange due to the size and polarisability of these ions: K^+ and Tl^+ with ionic radii of 1.4 Å and 1.5 Å respectively are often found to be replaced by water species on extra-framework sites. The O–O distance in H_2O is around 1.6 Å. Examples of the ion exchange of materials such as $KSbO_3$, of which all three polymorphs are able to be ion-exchanged, and $Tl_2Ta_2O_6$ are found in later chapters of this work. Few lithium-containing compounds have been found where hydration accompanies ion-exchange since Li^+, at 0.7 Å radius, usually occupies too small a cavity in three-dimensional materials to be replaced by water. Exceptions are found among layered materials such as the trirutile-structured $LiTaWO_6$.[20]

Together with directly synthesised hydrates such as HUP, α-ZrP and $MoO_2HPO_4.H_2O$, these ion-exchange products are often found to exhibit high degrees of proton conductivity, a phenomenon which will be discussed in the next section.

1.4 Proton-Conducting Materials [21,22]

Solid proton conductors have in recent years been investigated for potential applications as fuel cell and battery electrolytes and in sensors, photochemical cells and other devices. A solid proton conductor may be defined as a material in which at least part of the ionic conductivity is ascribed to protons or to protonic species such as oxonium, ammonium or hydroxyl ions. Among the classes of materials which fall in this category are ion-exchanged β-aluminas and zeolites, organic polymers such as polyethylene oxide/NH_4HSO_4 and defective oxides which conduct at high temperatures such as ytterbium-doped $SrCeO_3$. Proton conductivites of a selection of materials are given in table 1.1[23,24,25].

Part of this work is also directed at the class of hydrated materials already described. Channel-containing materials are of interest as model systems for proton conduction since the channels provide a pathway for proton motion, and many techniques have been used to study them.

In order for proton motion to occur two conditions must be fulfilled. First the pathway for such motion must extend continuously throughout the material and secondly there must exist simultaneously charge-carrying species that are free to move and vacancies. These requirements are frequently met by systems which possess a network of hydrogen bonds between the framework and the extra-framework species which assists the process of proton transfer from site to site along the conduction pathway.

In HUP, hydrogen bonds are believed, after the work of Fender, Fitch and others[26,27], to exist between framework oxygens and interlamellar water molecules and between the water species themselves, with O...H distances between 1.6 Å and 1.85 Å

Table 1.1 Room Temperature Conductivities of Selected Proton Conductors

Compound	$\log_{10}[\sigma/(\Omega cm)^{-1}]$
1M HCl	0
$Zr(HPO_4)_2.3\text{-}4H_2O$	-2
$HSbO_3.xH_2O$ (pyrochlore)	-2
$HSbO_3.xH_2O$ (cubic)	-3
$HUO_2PO_4.4H_2O$	-3
H_3OClO_4	-3
α-$Zr(HPO_4)_2.H_2O$	-4
$H_2Ta_2O_6.xH_2O$	-4
$SnO_2.2H_2O$	-4
NH_4^+-zeolite A (11% H_2O)	-5
NH_4HSO_4/PEO	-5
$H_3O^+\beta''$-alumina	-6
$H_3O^+\beta$-alumina	-10

and O-H...O angles in the range 162° to 175°. A similar network is thought to be present in α-ZrP[19]. Amongst three-dimensional conpounds, the defect pyrochlore $H_2Ta_2O_6.xH_2O$ has been shown by powder neutron diffraction to have water molecules situated in the centre of the pyrochlore cavity with the hydrogen of a framework hydroxyl group pointing towards it (O...H distance 2.3 Å)[3].

Two principal mechanisms have been proposed for the transport of protons in such materials. In the Grotthus mechanism[28], protons move in a correlated way between sites in the fixed lattice i.e. sites bound to the framework or to immovable extra-framework species. The "vehicle" mechanism involves concerted migration of two type of polyatomic species in opposite directions. Only one type of species carries the proton e.g. in hydrated materials the two species involved may be H_2O and H_3O^+. Any mechanism which involves the motion of polyatomic species is obviously restricted by the minimum size of the channels. However direct evidence for the Grotthus mechanism in inorganic compounds has not so far been obtained.

A problem with the conductivity observed in many proton-containing solids is that, in addition to its being due to the bulk transport of protons in the material, a contribution may also arise from water and acid molecules adhering to the particles of the solid. This surface conduction might be expected to be particularly pronounced in compounds prepared as polycrystalline samples, either by acid exchange or, as in the case of HUP, directly from an acidic precursor. It is therefore important when characterising proton conduction to distinguish between bulk and surface effects.

Taking HUP as an example, the large body of evidence built up in recent years has shown that bulk processes form the major contribution to protonic conductivity. In the original work of Shilton and Howe[29], which found a room temperature conductivity of $4\times10^{-3}\,(\Omega cm)^{-1}$, studies were carried out where samples were

equilibrated with solutions of phosphoric acid of varying pH. In each case the conductivity was unaltered, contrary to what would be expected if surface-adsorbed acid were responsible for conduction. Three further pieces of evidence also support a high value for bulk conductivity in HUP. First, the results of NMR relaxation time studies[30] were consistent with the bulk motion of protons, in terms both of the dynamic process observed and the intensity of the signal. Secondly both the conductivity and NMR measurements showed a marked discontinuity at 274 K, corresponding to a known phase transition in HUP, with the disordered high-temperature phase being the more highly-conducting. Thirdly the conductivity of the ammonium-containing analogue is some three orders of magnitude lower that that of HUP[31], and this may be interpreted in terms of the vacant hydrogen sites, which contribute to proton transport in HUP, being occupied in NH_4UP.

1.5 Protonic Conduction and Experiment [32,33,34,35]

Ionic conductivity in solids arises from the translational motion of the ions. The diffusion process can be considered as a series of jumps from occupied sites to unoccupied sites in the lattice. The self-diffusion coefficient for this process, measured at chemical equilibrium, can be associated with the jump distance, a, and the average time between jumps (residence time), τ, using random walk theory to give

$$D = \frac{pa^2}{n\tau}$$

where n is the possible number of jump sites and p, a correlation factor for successive jumps, is unity for a truly random process. The temperature dependence of D is generally of the form

$$D = D_0 \exp\frac{-E_a}{RT}$$

where E_a is the activation energy for the process.

Bulk conductivity may be related to particle diffusion by the Nernst-Einstein equation

$$\sigma = \frac{D_\sigma C z^2}{kT}$$

where C is the concentration of the mobile species, z is their charge number (unity for protons) and D_σ is the diffusion coefficient obtained. The ratio D/D_σ is commonly called the Haven ratio, H_R, and has a particular value for a given mechanism.

Information on the bulk transport properties on ion-conducting materials may be obtained from conductivity measurements. To investigate the microscopic processes which give rise to conductivity, and specifically protonic conductivity, two widely used techniques are nuclear magnetic resonance and incoherent neutron scattering.

Pulsed proton NMR techniques can, by measurement of the charateristic relaxation times, yield information on proton dynamics. T_1, commonly called the spin-lattice relaxation time, and T_2, the spin-spin relaxation time, are measured in variable-temperature experiments, enabling characteristic times for motions in the range 10^{-6} to 10^{-11} s and associated activation energies to be obtained. In some cases translational and localised motions may be distinguished by studying the temperature dependence of the relaxation times. Although this method essentially only probes the local environment of protons, the pulsed field gradient technique by contrast is sensitive to much larger domains of space and can lead to the direct determination of diffusion coefficients for fast translational processes.

Incoherent neutron scattering has the advantage that it can probe simultaneously a wide range of volumes giving information on both long-range and localised processes. In addition it is highly sensitive to the ^1H nucleus. Random motion of protons gives rise to quasielastic scattering, essentially a Doppler broadening of the elas-

tic peak. In an experiment the magnitude of this energy broadening, which may be dependent on the reduced wavevector, $\underline{Q}$, as well as on temperature, is determined.

For the case of translational motion a number of models have been developed to relate the nature of the diffusional process to the observed quasielastic spectrum. In the simplest case of continuous random diffusion of an atom in three dimensions the halfwidth of the quasielastic component is equal to DQ^2_{el} where D is the self-diffusion coefficient. This is a result of Fick's law. In fact it can be shown that the energy spectrum takes the form of a Lorentzian of halfwidth DQ^2_{el} i.e. the incoherent scattering function is given by

$$S_{inc}(\mathbf{Q},\omega) = \frac{1}{\pi}\frac{DQ^2_{el}}{(DQ^2_{el})^2+\omega^2}$$

Chudley and Elliott[36] took into account a jump mechanism to describe diffusion in a simple ordered system. It is assumed that the time taken for the jump is negligible compared to the mean residence time and that the jump distance is large in relation to the amplitude of thermal vibration of the atom. The broadening then also takes the shape of a Lorentzian and the model scattering function is given by

$$S_{inc}(\mathbf{Q},\omega) = \frac{1}{\pi}\frac{f(Q)}{[f(Q)]^2+\omega^2}$$

The halfwidth f(Q) depends both on the residence time and on the geometry of the lattice sites. At low Q_{el} i.e. where the observed volume is sufficiently large that the exact mechanisms of diffusion are not revealed, f(Q) reduces to DQ^2_{el} where

$$D = \frac{a^2}{n\tau}$$

as at the beginning of this section. If the possible jump sites consitute the points of a Bravais lattice then n=6. If the diffusion is further restricted n will be reduced, and the situation bceomes more complex when inequivalent jump sites are considered. However in all cases the DQ^2_{el} relation holds at sufficiently low Q_{el}

If a protonic motion is localised, for example if it represents a rotation of a water or ammonia molecule, then the quasielastic width is not dependent on Q. In this case the quantity of interest is the ratio of the intensity of elastic scattering to the total intensity of elastic and quasielastic scattering. This quantity is known as the elastic incoherent structure factor (EISF) and can, by its Q-dependence reveal details of a localised diffusional process.

1.6 Intercalation Chemistry [37]

A well-known feature of the chemistry of layered compounds is that they may undergo intercalation reactions whereby guest species are inserted into the host material in such a way that the structure of its layers remains essentially unchanged. Such reactions are generally reversible and often involve major changes in the physical properties of the material. For example graphite forms a wide range of intercalation compounds[38] both with electron-donating species such as alkali metals and with electron acceptors such as halogens and halides e.g. $FeCl_3$, $SbCl_5$. The alkali metal intercalates are characterised by their metallic properties. Large increases in the basal spacing are commonly observed. Another area of intercalation chemistry concerns the reaction of clays with organic compounds where many examples of chemical conversion of the guest molecules are found i.e. the silicate clays act as catalysts. A simple example is the elimination of ammonia from pairs of *n*–alkylamine molecules intercalated into montmorillonite, yielding the secondary amine[39].

Intercalation has been studied in acid phosphates of the type described in the previous sections. In particular α-ZrP has been widely investigated by the groups of Constantino, Clearfield and others. Since α-ZrP is a Brønsted acid, organic amines intercalate particularly well as do to a lesser extent alcohols, glycols and esters. The reactions may be thought of as acid-base interactions where each

function of the intercalate liberates a proton from the acid framework.

A wide range of *n*-alkylamines and diamines has been intercalated into α-ZrP. In the case of monoamines, high intercalant content (up to one molecule per phosphate group) results in the formation of bilayers of amine molecules between the layers of α–ZrP, with the carbon chains aligned at around 60° to the plane of the layers[40,41]. Similarly for α,ω–alkyl diamines, "tilted" layers of single molecules are observed in intercalates[42]. Amine intercalation has also been found to have an effect on the proton conductivity of the material with, for example, conductivity increased by an order of magnitude on intercalation of hydrazine[41]. *n*–Alkanols and glycols intercalate in a very similar way[43] with, as also in the case of the amines, a linear increase in interlayer spacing with respect to carbon chain length being observed. For smaller alcohol molecules, intercalation is easily reversible by heating. This does not occur with the more strongly-bound amine intercalates, where thermal decomposition of the phosphate occurs before all the intercalant is expelled.

The intercalation chemistry of HUP has also been investigated. In a recent study[44], crystalline intercalates were found with hydrazine and with the cyclic amines piperidine, pyridine and pyrazine. X-ray diffraction showed that the structure of the layers was unchanged, but the increase in the interlayer spacing indicated that the aromatic intercalates were oriented with their planes parallel to the host layers. Dimethylaminomethyl ferrocene was also intercalated, with a 10 Å increase in the basal spacing being consistent with a bilayer of the molecule forming in the interlamellar region. Infrared spectroscopy highlighted the acid-base nature of the intercalation reactions with characteristic ionic vibration bands for the intercalants indicating proton transfer from the host.

CHAPTER 2

EXPERIMENTAL TECHNIQUES

2.1 Powder X-Ray Diffraction

Powder x-ray diffraction, used routinely for the characterisation of solid samples and for the determination of unit cell parameters, was carried out using an INEL position sensitive detector system. The X-ray source in this system made use of Cu K radiation which passed through a single quartz crystal monochromator to exclude all but the Cu K_{α_1} line (λ=1.54056 Å) and was collimated to ensure minimum beam divergence at the sample surface. The angle of incidence of the beam onto the plane surface of the sample, ordinarily contained in a recessed aluminium holder, was typically 85°. Data collection times were of the order of 30 min. The curved INEL CPS-120 detector covered a 2θ range of approximately 120°, and data was collected into a Silena Cato multichannel analyser with 8192 channels. This gave a resolution of 0.015°. The spectra collected by the multichannel analyser were transferred to an IBM PC-AT and there analysed by a Gaussian peakshape program which identified the Bragg peaks and minimised for each, using a χ^2 method, the difference between observed integrated intensity and that calculated for a Gaussian. This has the effect of giving accurate peak positions and intensities and of deconvoluting overlapping peaks. The system was periodically calibrated using α–alumina as a standard, with the channels corresponding to approximately 20 of the accurately-known Bragg peaks of the calibrant being identified and related by a sixth-order polynomial. The calibration data was then stored for future reference on the IBM PC.

Earlier work was carried out using a Philips moving-arm diffractometer. On this instrument data were ordinarily collected up to a 2θ value of 80° since the low

signal to noise ratio above this angle precluded any meaningful analysis of the data.

Unit cell parameters were refined using the program CELL which minimises the expression

$$M = \sum_i w_i (\sin^2\theta_i^{obs} - \sin^2\theta_i^{calc})^2$$

where i is a single reflection *hkl*, using an iterative least squares method. In addition, powder patterns for a given unit cell and its contents could be simulated using the program LAZY-PULVERIX[1], and attempts at indexing the patterns of unknown phases could be performed using an autoindexing program due to Visser[2]. These three programs were available on an IBM3090 computer at Southampton.

2.2 Infrared Spectroscopy

Infrared absorption spectra were recorded using a Perkin Elmer 1710 Fourier-transform instrument (range 4000-400 cm^{-1}), a Perkin Elmer 580B (4000-200 cm^{-1}) or a Perkin Elmer 599 (4000-200 cm^{-1}). Samples were normally in the form of a pressed CsI disc produced by intimately grinding together pure sample with an excess (between 20 and 50 times by volume) of dried CsI (BDH,SpectrosoL) and pressing the 15 mm diameter disc under 10 tonnes. Occasionally spectra were recorded of samples as Nujol mulls, held between CsI plates

2.3 Thermogravimetric Analysis (TGA)

TGA was carried out using a Stanton Redcroft TG1000 thermobalance. Samples in the weight range 15-20 mg were used, enabling high resolution to be obtained on the balance's most sensitive scale (precision 0.5 μg). Samples were contained in a platinum crucible and were able to be heated up to 1000 °C. A temperature program unit allowed a number of temperature ramp and isotherm steps to be pre-programmed as required. The data was presented graphically via a chart recorder and for each

sample this included a plot of the differential of weight loss against time (DTG).

2.4 Elemental Analysis

(a) Quantitative Methods

Various titrimetric and gravimetric methods have been used. These are described in the later sections of this work to which they are relevant.

(b) Semi-Quantitative Methods

Scanning Electron Microscopy/X-Ray Analysis

One of the well-known effects of bombarding a chemical sample with high energy electrons is the generation of x-rays. The energy spectrum of these x-rays is a characteristic solely of the elements present in the sample. Therefore if the x-rays emitted from a sample in an electron microscope are analysed and a suitable calibration technique employed, it is possible to determine the elemental composition of the sample. The technique is however usually only appropriate to elements heavier than and including fluorine.

In this work a Cambridge Stereoscan 150 scanning electron microscope was used in conjunction with an EDAX energy-dispersive x-ray analysis unit. Samples were mounted on an aluminium stub using a conductive paste and a thin layer of gold sputtered onto the surface using an Agar Aids PS3 coating unit. The microscope had a resolution of the order of 100 nm enabling particles of a polycrystalline sample to be identified and the x-rays emitted from an approximately circular surface area of 2-4 μm in diameter to be collected and analysed. The data were presented in the form of a ratio by percentage mass of the various elements which are analysed. The accuracy in elemental analysis is usually taken to be no better than 2-3% of the total. The cumulative efffect in analysing for several elements therefore means that small per-

centages should be taken as an approximate figure only.

Flame Photometry

A Corning 300 flame photometer was used to determine the amount of alkali metals present in an aqueous solution. The solution to be analysed was diluted so that the content of the desired element fell in the region 20-100 ppm. Prior to each analysis the instrument was calibrated using a range of standard solutions of between 0 and 100 ppm concentration. The precision of results was found to be ±2 ppm.

2.5 Nuclear Magnetic Resonance

Magic Angle Spinning Solid-State-NMR spectra were recorded on the S.E.R.C. national facility Varian VXR300 spectrometer at Durham. Approximately 0.5 g of material was used and rotator speeds of 5000 rev s^{-1} were sufficient to give good resolution spectra but with reasonably low intensity spinning side bands.

2.6 A.C. Conductivity [3,4]

The ionic conductivity of a solid is related to the activation energy for ionic motion by the following equation

$$\sigma = \frac{A}{T}\exp\left[-\frac{E_a}{RT}\right]$$

where A is a constant factor and E_a is the activation energy.

It follows that by measuring the temperature dependence of conductivity, the activation energy may be determined by plotting $\ln(\sigma T)$ against T^{-1}. The gradient of the straight line is given by $-E_a/R$.

In a.c. methods conductivity is determined by a complex impedance technique. The frequency dependence of the impedance, z, is analysed by plots of z' (real part of impedance) against z'' (complex part) where

$$\mathbf{z} = z' + z''$$

The intercept of the plot on the z′ axis is taken as the resistance of the sample.

In this work proton conductivity was determined using a Solartron 1250 frequency analyser and a Solartron 1286 electrochemical interface in conjunction with a specially designed cell. The sample was in the form of a pressed pellet of known dimensions whose opposite faces were ground smooth and coated with gold to a depth of about 200 Å.

In the simplest representative circuit, a sample whose conductivity is solely due to protons is assumed to act as a capacitor, C_1, in parallel with a resistor R and a second capacitor, C_2. Capacitance C_1 represents the bulk capacitance of the sample, C_2 is the interfacial double layer capacitance and R is the resistance associated with the bulk protonic conductivity.

2.7 Theory of Diffraction [5,6]

The contribution of a given stationary atom to the structure factor is determined by multiplying its scattering amplitude by an appropriate phase factor, giving an expression of the form

$$F = f_j \exp\left[i\,\alpha_j\right]$$

where f_j is the scattering amplitude and α_j the phase factor of the jth atom. When the phase factor is evaluated, the structure factor for the reflection *hkl* becomes

$$F_{hkl} = \sum_j f_j \exp\left\{2\pi i\,(hx_j + ky_j + lz_j)\right\}$$

where x_j, y_j, z_j are the coordinates of the jth atom and *h,k,l* are the Miller indices denoting the plane from which scattering occurs. It can be shown that the intensity of the reflection is proportional to the square of the structure amplitude $|F_{hkl}|^2$.

It should be noted that the above equations relate only to perfectly ordered crystals in which the atoms are static. Thermal motion and crystal disorder however cause reality to depart from the ideal. At any finite temperature thermal motions cause time-dependent displacement of atoms about their mean positions. In addition, lattice defects and substitutional disorders will occur, particularly in non-stoichiometric compounds. In this case the defects will tend to cluster leading to lattice relaxation. The net result of these effects is that the average unit cell contents will differ from those of a true unit cell.

The degree of thermal motion is determined in terms of temperature factors for the individual atoms in the unit cell. The temperature factor, B, is a function of the mean square displacement of an atom from its mean position and, if this is assumed to be isotropic, is usually expressed as part of the coefficient

$$T_{hkl} = \exp\left[-B\frac{\sin^2\theta_{hkl}}{\lambda^2}\right]$$

where, for a single atom,

$$B_j = 8\pi^2\bar{u}_j$$

$\bar{u}_j$ is the mean-square displacement of the scattering atom from the plane *hkl*. Taking into account also the effect of crystal defects, the structure factor becomes

$$F_{hkl} = \sum_j n_j f_j \exp\left[-B_j\frac{\sin^2\theta_{hkl}}{\lambda^2}\right]\exp\left\{2\pi i\,(hx_j+ky_j+lz_j)\right\}$$

where n_j is the average occupation number of the jth atom (i.e. n_j is unity for a defect-free, stoichiometric structure). If the treatment is extended to take into account anisotropic motion it can be shown that the exponential correction factor may be written as

$$T_{hkl} = \exp-(\beta_{11}h^2+\beta_{22}k^2+\beta_{33}l^2+\beta_{12}hk+\beta_{23}kl+\beta_{31}lh)$$

where the coefficients β are the six independent components of a symmetric second-

order tensor, although they may be constrained by unit cell and site symmetry. The anisotropic temperature factors are often taken to define an ellipsoid representing the mean square motion of an atom.

2.8 Powder Neutron Diffraction [7]

Neutron diffraction has two major advantages over x-ray methods which are of interest in conventional structure determination. First, atomic scattering amplitude does not increase with atomic number but varies in a more random fashion, enabling in certain cases atoms of similar atomic number to be distinguished and also very light atoms to be determined in the presence of heavier ones. In particular, the use of deuterium substitution allows detailed structures to be determined for hydrogen-containing materials since the scattering amplitude (i.e. coherent scattering length) of deuterium is of the same order of magnitude as, for example, of antimony or molybdenum. Secondly, since neutrons are scattered by atomic nuclei, and not by electrons, intensity of scattering does not fall off with 2θ, thus enabling accurate data to be collected at high angles. This last advantage enables polycrystalline samples to be used in detailed structural studies, although it should be pointed out that until very recently powder methods have only been used for the refinement of structures which have been partially solved already by other techniques.

2.8.1 Instrumentation [8]

Powder neutron diffraction profiles were collected on the instrument D2B at the Institut Laue-Langevin (I.L.L.), Grenoble, France. This diffractometer has been designed to permit investigation of samples with unit cell volumes of up to 2000 Å^3 and up to 250 structural parameters. Owing to its situation close to the reactor core, the instrument is able to make use of a high flux of neutrons thus shortening collec-

tion times. Other special features include a large monochromator take-off angle of 135° to obtain good resolution at high angles, a wide choice of wavelengths between 1 Å and 6 Å and a bank of 64 high-efficiency ^{3}He counters at intervals of 2.5°. This last feature permits a maximum of eight profiles to be collected simultaneously and summed, with each profile representing a pass of the detector bank of 2.5°, and thus producing improved statistics. The instrument can operate in two modes: a high flux mode where scan times are of the order of 4 to 6 h and a high resolution mode involving a more highly collimated neutron beam where collection times are generally beteen 15 and 20 h. The collection and initial treatment of data were controlled by a PDP 11/24 computer. Samples were contained in thin-walled vanadium cans and sealed with an indium wire gasket, allowing them to be cooled as far as liquid helium temperatures in an I.L.L. "Orange" cryostat. In this work the neutron wavelength used was 1.595 Å and samples were between 5 and 10 g in mass. A diagram of the instrument is shown in figure 2.1.

2.8.2 Profile Refinement

The use of polycrystalline samples presents two principal disadvantages over single crystal methods. First the random orientation of crystallites results in an inevitable loss of information since each reflection is only described by one 2θ value and secondly finite peakwidths, caused by imperfect monochromatisation of the neutron beam, lead in practice to overlap between closely separated reflections for all but highly symmetric structures, making the accurate determination of intensities difficult.

This latter problem is being alleviated in part by the use of very high resolution instruments such as HRPD at the Rutherford-Appleton Laboratory and D2B at the I.L.L.. In addition, structural refinement is commonly carried out by a profile method, first developed by Rietveld[9], whereby it is assumed that each individual diffraction

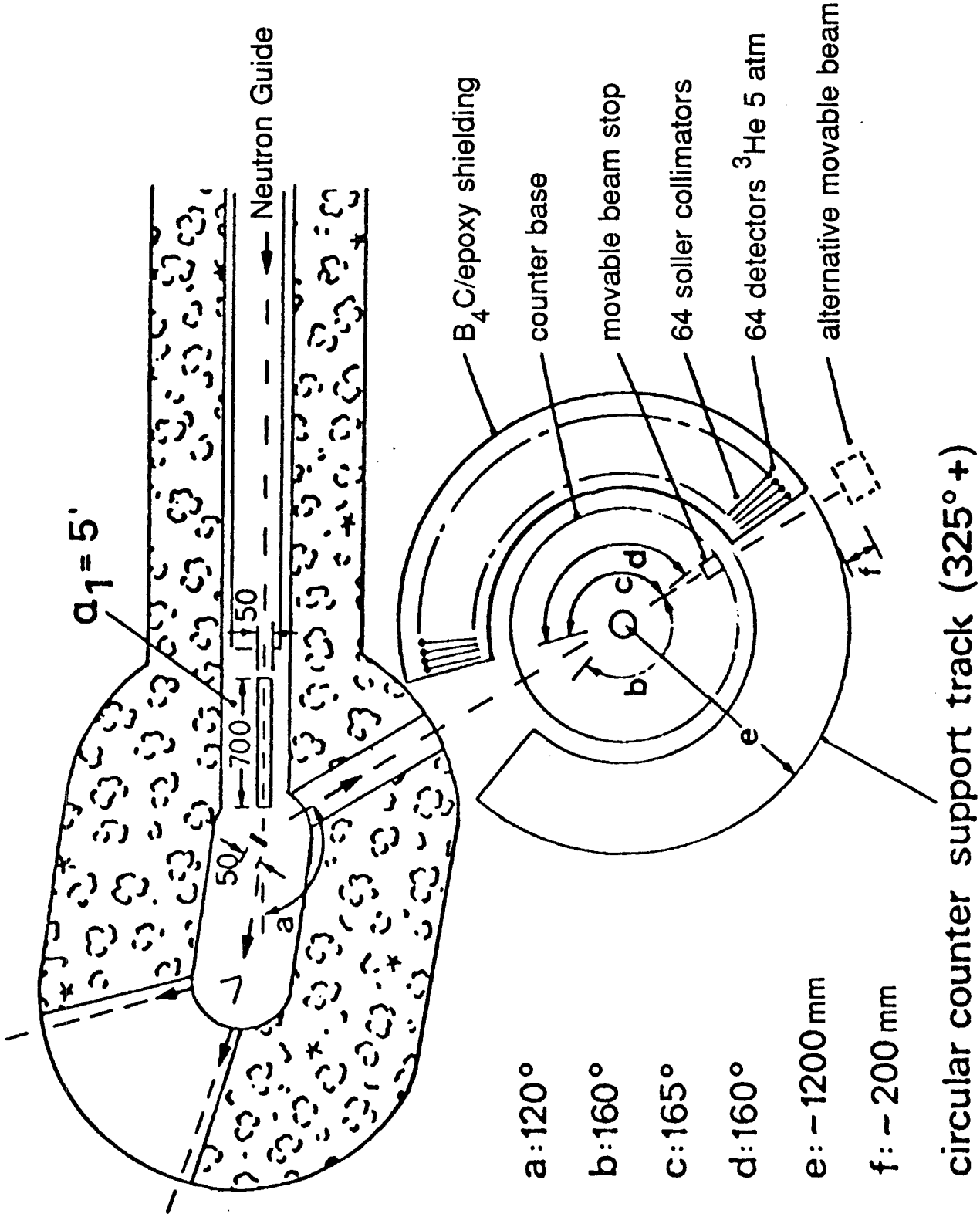

Figure 2.1 Plan view of the powder neutron diffractometer D2B.

peak corresponds almost exactly to a Gaussian in shape. This approximation is only valid for single wavelength techniques.

After manual subtraction of a background, the observed counts, y_i^{obs}, are compared with those for a trial structure, y_i^{calc}, for each point in the profile (in the case of D2B at every 0.025° of 2θ). The parameters y_i^{calc} are then adjusted to minimise

$$M = \sum_i w_i (y_i^{obs} - c y_i^{calc})^2$$

where w_i is a weighting factor given by $1/y_i^{obs}$ and c is the overall scale factor. The contribution of a Gaussian peak of integrated intensity I_k to the count y_i at $2\theta_i$ is given by

$$y_i = I_k \exp\left\{-b_k (2\theta_i - 2\theta_k)^2\right\}$$

where $2\theta_i$ is the Bragg angle of the peak, and

$$b_k = \frac{4\ln 2}{H_k^2}$$

The halfwidth, H_k, of a peak varies with scattering angle θ_k empirically, but accurately, as

$$H_k^2 = U\tan^2\theta + V\tan\theta + W$$

U, V and W depend on the instrumental geometry and are refinable parameters.

At very low scattering angles the peaks show a distinct asymmetry due to the use of finite slit widths and sample heights. This effect causes the maximum of a peak to shift to a lower angle but leaving its integrated intensity unchanged. A semi-empirical correction factor may be introduced into the refinement to account for this. In addition since the tails of a Gaussian diminish rapidly it is assumed that the contribution from a particular peak extends no further than $1.5H_k$ either side of $2\theta_k$.

The parameters defining a trial structure thus consist first of those which deter-

mine peak position and shape, including the unit cell parameters, the three halfwidth parameters, the asymmetry factor and a counter zero point, and secondly those defining the unit cell contents i.e. for each atom its scattering amplitude (scattering length in the case of neutrons), coordinates, occupation number and thermal factors, and finally the profile scale factor.

The difference between the observed and calculated profiles is then minimised by an iterative least squares method and involving some or all of the above parameters.

The degree of agreement between the observed and calculated profiles after a refinement may be expressed quantitatively by a residual or R-factor. The profile R-factor is given by

$$R_p = 100\left\{\frac{\sum_i (y_i^{obs} - c^{-1} y_i^{calc})^2}{\sum_i (y_i^{obs})^2}\right\}^{\frac{1}{2}}$$

The more commonly quoted weighted profile R-factor is given by

$$R_{wp} = 100\left\{\frac{\sum_i w_i (y_i^{obs} - c^{-1} y_i^{calc})^2}{\sum_i w_i (y_i^{obs})^2}\right\}^{\frac{1}{2}}$$

This may be compared with a theoretical R-factor defined as

$$R_{expected} = \frac{100 N^{\frac{1}{2}}}{\sum_i W_i (obs)}$$

where N is the number of degrees of freedom. A fourth R-factor, R_I, based on the difference between observed and calculated intensities and analogous to that produced by least squares intensity methods is given by

$$R_I = \frac{\sum |I_{obs} - I_{calc}|}{\sum I_{obs}}$$

Deviations from the ideal peakshape and errors in angular calibration invariably cause R_{wp} to increase relative to R_I. However refinements which produce a large difference between the two should be treated with caution.

2.8.3 Fourier Synthesis

A further technique which is appropriate to this type of structural work is the use of Fourier synthesis to obtain maps of nuclear density distribution. The nuclear density at the point in real space x,y,z is given by an expression of the form

$$\rho_{xyz} = \frac{1}{V}\sum_h\sum_k\sum_l F_{hkl}\exp\left\{-2\pi i\,(hx+ky+lz)\right\}$$

where V is the unit cell volume. It follows that since the structure factor F_{hkl} is involved, the phase factors for each reflection should be known before this technique can be applied. In practice this means that a substantial part of the structure should have already have been solved in order to obtain meaningful results.

In a simple Fourier summation the expression is evaluated by taking the observed magnitudes of F_{hkl} together with the estimated phase factors. A Fourier difference map may also be obtained for a trial structure in which the differences in magnitude between observed and calculated structures are employed. This is of particular use in locating weakly scattering centres.

It should be noted however that for neutron scattering the accuracy of Fourier techniques is limited. Since scattering amplitude does not include a term dependent on 2θ, the limits of data collection inevitably introduce a termination error into the summation.

2.9 Quasielastic Neutron Scattering [8,10]

Inelastic neutron scattering data were recorded on the spectrometer IN6 at the I.L.L., Grenoble. This is a time-focussing time-of-flight spectrometer capable of

operating over a range of wavelengths between 4.1 Å and 5.9 Å. As can be seen in figure 5.2, the neutron beam was extracted from the beam guide by means of three monochromators, each consisting of crystals of pyrolytic graphite. The monochromators were aligned such that the neutron beam was directed onto the sample by reflection from the 002 plane of graphite. After passing through a cooled beryllium filter to remove the second order graphite reflection, the beam was collimated and then pulsed by a Fermi chopper capable of rotating at between 2000 and 20000 rev min^{-1}. An additional chopper prevented frame overlap at high speeds of rotation by turning in phase with the Fermi chopper at a lower speed. The sample area consisted of an evacuated chamber which may contain a cryostat or furnace. In order to minimise the effects of absorption and self-shielding a solid sample is ordinarily contained in a thin-walled aluminium can (aluminium having a very low ratio of absorption to scattering) such that the sample has a thickness of 1 mm. The sample is aligned at an angle of 135° to the incident beam. The curved detector bank consisted of 337 ^{3}He detectors covering a range of 10° to 115° 2θ and a vertical angle of ±15° out of the plane of scattering. The distance from sample to detectors was 2.466 m and the volume between the two filled with helium in order to minimise background scattering. A low-efficiency monitor placed in the path of the beam between the choppers and the sample permitted the number of neutrons incident on the sample during the course of an experiment to be evaluated. A second monitor situated in the line of the beam after the sample area allowed the transmission of a sample to be measured. For this purpose the sample was aligned at 90° to the incident beam. Data collection and control of the instrument were carried out by a PDP 11/34 computer. At 5.1 Å the elastic peak resolution of the instrument was of the order of 80 μeV (full width at half maximum).

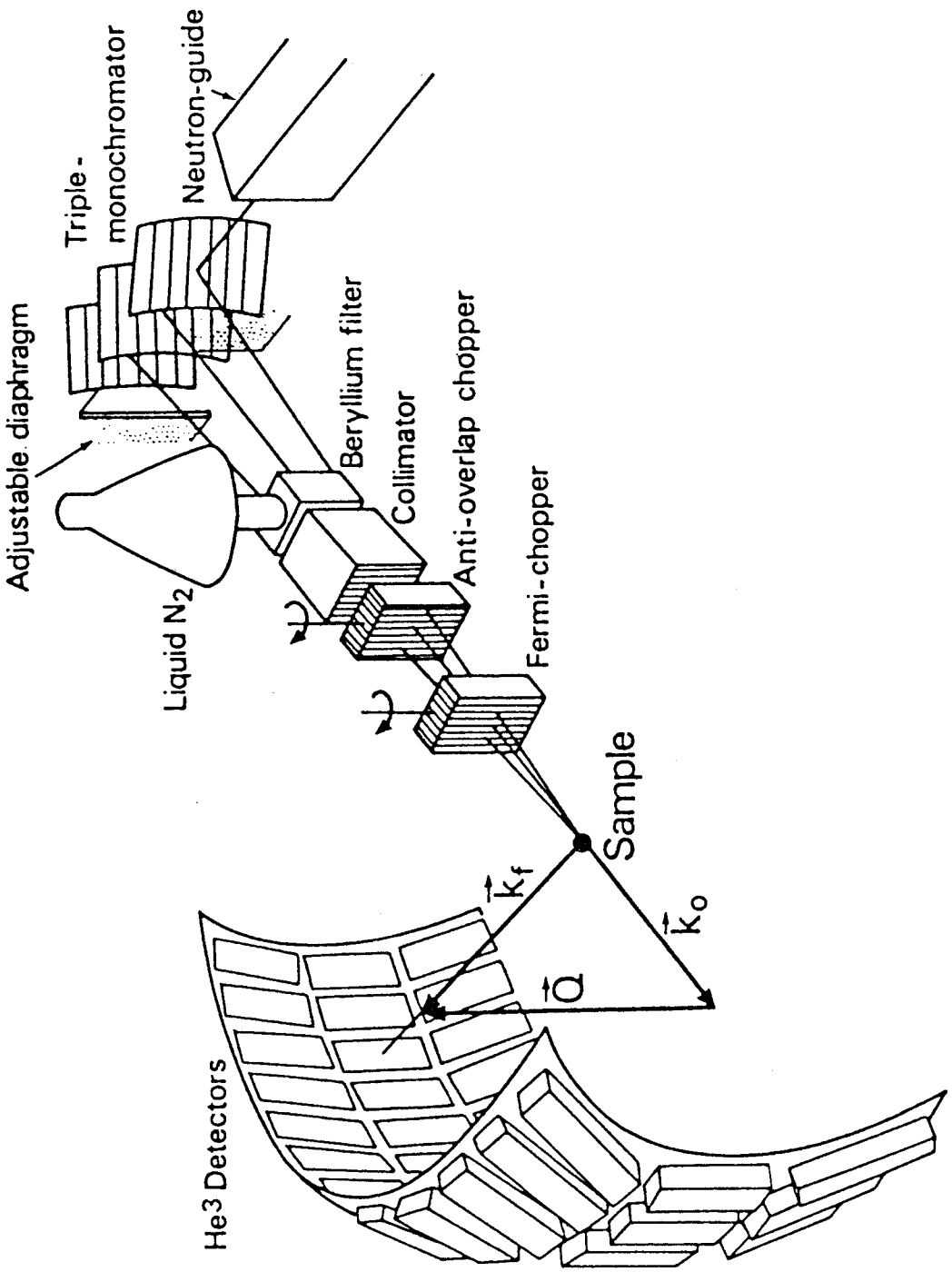

Figure 2.2 Diagram of the time-of-flight inelastic neutron scattering spectrometer IN6.

CHAPTER 3

STRUCTURE AND PROPERTIES OF $MoO_2HPO_4.H_2O$

3.1 Introduction

A compound of the composition $2MoO_2.P_2O_5.3H_2O$ was first reported by Schulz in 1955[1]. It was described as forming rod-shaped crystals and as being slightly soluble in cold water but dissolving in hot water to form a strongly acidic yellow solution which lost its colour on cooling. Its properties led Schulz to describe it as an orthophosphate and since it decomposed as 300 °C to form a pyrophosphate she concluded that at least one of the three H_2O units must exist as part of P–O–H groups and suggested the formula $MoO_2HPO_4.H_2O$.

Kierkegaard[2] shortly afterwards studied this material by single crystal x-ray diffraction and found that its structure consisted of double chains of linked MoO_6 octahedra and PO_4 tetrahedra running parallel to each other and to the *y*-axis of the monoclinic unit cell (figure 1.7). The refinement was unable to locate hydrogen atom positions and there was some uncertainty in the oxygen atom positions. Nevertheless Kierkegaard thought it most likely that the three H atoms were bound to the three unshared oxygens in the MoO_6 octahedron giving a fairly regular octahedral coordination for molydenum, linked by $O\text{-}PO_2\text{-}O$ units. He therefore described the compound as $Mo(OH)_3PO_4$.

The infrared spectrum of the compound however shows a very strong absorption at $1620\,cm^{-1}$ indicating the presence of discrete water molecules in the structure[3] (the symmetric bend, ν_2, of H_2O occurs at *ca.* $1600\,cm^{-1}$).

The structure of $MoO_2HPO_4.H_2O$ is similar in some respects to those of other acid salts of highly charged metals. In these types of compound high values of proton

mobility have often been found. In particular the well-studied compounds hydrogen uranyl phosphate (HUP), $HUO_2PO_4.H_2O$ and the zirconium phosphates e.g. α–$Zr(HPO_4)_2.H_2O$, as described in chapter 1, have been found to have room-temperature conductivities of the order of 10^{-3} and $10^{-4}\,(\Omega cm)^{-1}$ respectively. Both these materials contain metal atoms bound to oxygen and linked into two-dimensional networks by phosphate groups. The interlayer region is occupied by water molecules hydrogen-bonded to the phosphate layers. Proton mobility is thought to occur in these compounds by a Grotthus-type mechanism in which the acidic proton normally coordinated to the layer phosphate group is transported along the interlayer region.

Although strictly a one-dimensional rather than lamellar structure, $MoO_2HPO_4.H_2O$ contains molybdenyl groups linked by phosphate, analogous to the linear uranyl groups in HUP, and contains acidic protons. It is thus reasonable to speculate that protonic conductivity is possible in this material.

In this work the structure of $MoO_2HPO_4.H_2O$ has been determined by powder neutron diffraction using a fully deuterated sample. The deuterium positions obtained in the refinement resolve unambiguously the previous uncertainty concerning the structure of this compound. In addition, a study of the proton conductivity of $MoO_2HPO_4.H_2O$ has been performed using an a.c. impedance method.

3.2 Synthesis

$MoO_2HPO_4.H_2O$ was prepared according to the method of Kierkegaard. 10 g of dried MoO_3 (Hopkin and Williams, AnalaR) was dissolved in $30\,cm^3$ H_3PO_4 (Interchem, 88% w/v) by refluxing a mixture at 180 °C for three hours. The pale green viscous solution was then cooled and diluted with $270\,cm^3$ HNO_3 (May & Baker, 70% w/v). The mixture was then refluxed for a further six hours. On cooling again to

room temperature fine white crystals of $MoO_2HPO_4.H_2O$ separated out slowly. The compound dissolves slightly in cold water and so, after filtering, it was washed with either acetone or dry ether. Approximately 15 g of product was usually obtained.

For powder neutron diffraction a fully deuterated sample was prepared using D_3PO_4 (Aldrich, 85% w/v, >99% D) and DNO_3 (Koch-Light, 50% w/v, >98.5% D). All manipulation of the reactants was carried out in a glove box under an atmosphere of dry nitrogen, and the reaction itself took place in a three-necked round-bottomed flask through which a current of dry nitrogen was maintained. The scale of the reaction was chosen so as to produce about 5 g of solid product which was washed with sodium-dried ether, thereby minimising any proton-deuteron exchange.

Both protonated and deuterated samples were characterised by powder x-ray diffraction, infrared spectroscopy and thermogravimetric analysis. A solid state NMR spectrum of $MoO_2HPO_4.H_2O$ was also recorded.

3.3 Powder X-Ray Diffraction

The diffraction pattern of $MoO_2HPO_4.H_2O$ showed a pure crystalline phase. All the reflections could be indexed on a monoclinic unit cell of similar dimensions to those reported by Kierkegaard, and in the space group $P2_1/m$:

a=6.774(2), b=6.369(2), c=7.073(2) Å and β=110.09(2)°

(literature: a=6.731(5), b=6.319(5), c=7.034(5) Å and β=110.16(5)°).

Observed and calculated diffraction peak positions are tabulated in table 3.1. Similarly, the pattern for $MoO_2DPO_4.D_2O$ showed no evidence of crystalline impurity and could be completely indexed using the monoclinic cell parameters

a=6.723(4), b=6.326(2), c=7.038(4) Å and β=110.12(3)°.

Table 3.1 Observed and Calculated Powder Diffraction Data for $MoO_2HPO_4.H_2O$

h k l	*2θ(obs)*	*2θ(calc)*	*h k l*	*2θ(obs)*	*2θ(calc)*
1 0 -1	15.66	15.62	2 0 -4	52.65	52.65
0 1 1	19.32	19.29	1 1 -4	53.94	53.97
1 1 0	19.72	19.71	4 0 -1	54.49	54.47
1 1 -1	20.96	20.96	2 1 -4	54.73	54.73
1 0 1	22.42	22.41	4 1 -1	56.45	56.50
1 0 -2	25.60	25.62	4 1 -2	56.75	56.74
1 1 1	26.52	26.46	0 1 4	57.31	57.29
2 0 -1	"	26.57	4 0 0	57.91	57.93
0 0 2	26.82	26.82	1 3 -3	58.51	58.45
0 2 0	28.02	28.00	4 0 -3	"	58.64
2 1 -1	30.13	30.10	3 1 -4	59.45	59.46
0 1 2	30.33	30.33	1 4 0	59.81	59.82
2 1 0	31.41	31.41	1 4 -1	60.38	60.33
2 0 -2	31.53	31.53	0 3 3	"	60.35
1 2 -1	32.21	32.21	2 3 -3	"	60.45
1 0 2	34.53	34.46	3 1 2	61.10	61.08
2 1 -1	"	35.61	3 3 0	61.78	61.78
1 2 1	36.14	36.14	1 0 4	62.39	62.41
1 1 2	37.30	37.32	2 3 2	64.27	64.24
2 1 1	37.99	38.00	1 1 4	"	64.29
2 2 -1	38.98	38.98	2 4 -1	64.80	64.76
0 2 2	39.17	39.16	4 2 0	65.59	65.55
2 2 0	40.01	40.03	1 3 3	66.00	65.97
0 0 3	40.72	40.72	2 0 -5	66.22	66.22
3 0 -2	41.87	41.90	4 1 1	66.64	66.57
3 1 -1	42.44	42.45	3 2 2	"	66.69
3 0 0	42.61	42.60	2 1 -5	68.06	68.04
0 1 3	43.19	43.22	1 1 -5	68.59	68.56
3 1 0	45.06	45.02	5 0 -2	69.37	69.37
1 3 -1	45.67	45.59	2 3 -4	69.92	69.91
2 0 2	"	45.74	3 1 -5	71.01	71.10
3 0 -3	48.05	48.11	0 3 4	72.24	72.16
3 2 -1	49.42	49.45	2 4 -3	73.27	73.24
0 3 2	50.14	50.14	3 3 -4	74.12	74.09
3 2 -2	51.10	51.15	5 0 0	74.53	74.51
1 0 -4	51.85	51.87	5 2 -2	76.40	76.39

λ=1.5406 Å

a=6.774(2) Å, b=6.369(2) Å, c=7.073(2) Å, β=110.09(2)°

3.4 Powder Neutron Diffraction

The powder neutron diffraction spectrum of the 5 g sample was recorded on the instrument D2B at the I.L.L., Grenoble. The sample was contained in a thin-walled vanadium can and cooled to 5 K at atmospheric pressure. The diffractometer was operating in high-flux mode at a wavelength of 1.595 Å and the profile was obtained in 2θ steps of 0.025° between 0 and 160°. All the peaks in the profile with the exception of seven widely spaced reflections could be indexed using the lattice parameters obtained from powder x-ray diffraction in the space group $P2_1/m$. The additional peaks were found to be the result of diffraction by the aluminium cryostat tail. These peaks were displaced slightly from the expected 2θ positions owing to the off-centre nature of the diffraction. The data were fitted using a version of the Rietveld refinement program described in chapter 2. The background was determined between peaks wherever possible at low angles and estimated at 5° intervals at higher 2θ values. Sections of the profile containing the aluminium diffraction peaks were placed in excluded regions. The atomic scattering lengths were taken as

Mo 0.695, O 0.581, D 0.667 and P 0.513 (all $\times 10^{-14}$ m).

Initial refinements were performed on a restricted section of the profile, starting at low 2θ, and were based on the structure determined by Kierkegaard but with no deuterium positions included. The parameters varied were the scale factor, halfwidth parameters, cell constants and zero point. This produced R_{wp} in excess of 30%. The Mo, P and O positional parameters were then refined, reducing R_{wp} to around 25%. At this stage a Fourier difference map was calculated. A deuterium position was located in proximity to the oxygen, O(3), which is bound to P. Of the other possible sites two were approximately 1 Å distant from O(6), an unshared oxygen in the MoO_6 octahedron. Deuterium atoms were introduced into the refinement on these

sites, yielding R_{wp} of 12% and producing chemically reasonable D-atom positions. Lastly anisotropic temperature factors were introduced. The final refinement thus included a total of 69 atomic parameters, the scale factor, the three halfwidth parameters, four cell constants and the zeropoint. The profile used was between 30° and 140° of 2θ, containing 516 reflections. R_I was 4.49% R_{wp} 9.20% and R_{exp} 3.56%. A full list of observed and calculated intensities is given in appendix 1, and a plot of the observed and calculated diffraction profiles may be seen in figure 3.1. The final atomic parameters are given in table 3.2. All the atoms except O(1) lie on 2e sites in the y=0.25 plane. Attempts to refine the structure in the lower symmetry space group $P2_1$, which allows the atoms to move out of this plane, produced no stable refinement and no improvement in R-factors.

3.5 Discussion of the Structure

A thermal ellipsoid plot of the structure is shown in figure 3.2 and bond distances and angles are given in table 3.3. The planes containing most of the atoms are linked together by the O1 oxygens, and each plane is related to its nearest neighbour in the *y*-direction by the twofold axis. The oxygen atom positions determined here in some cases differ significantly from those obtained by Kierkegaard. The molybenum environment consists of two short bonds (*ca.*1.7 Å) to O(4) and O(6) typical of a bent molbydenyl group, three normal Mo-O bonds of around 2.0 Å linking to phosphate groups and a weakly bound D_2O molecule with a Mo-O distance of 2.71 Å. The geometry of the MoO_6 unit is somewhat distorted from that of a regular octahedron, with angles between neighbouring oxygens varying from 79° to 97°. This environment is similar in some respects to that found in molecular $Mo[(CH)_2NCHO]_2O_2Cl_2$ where a bent molybdenyl group (Mo-O=1.68 Å) is coordinated to the ligand oxygen (Mo-O=2.20 Å) and to chlorine in an approximately octahedral coordination sphere[4].

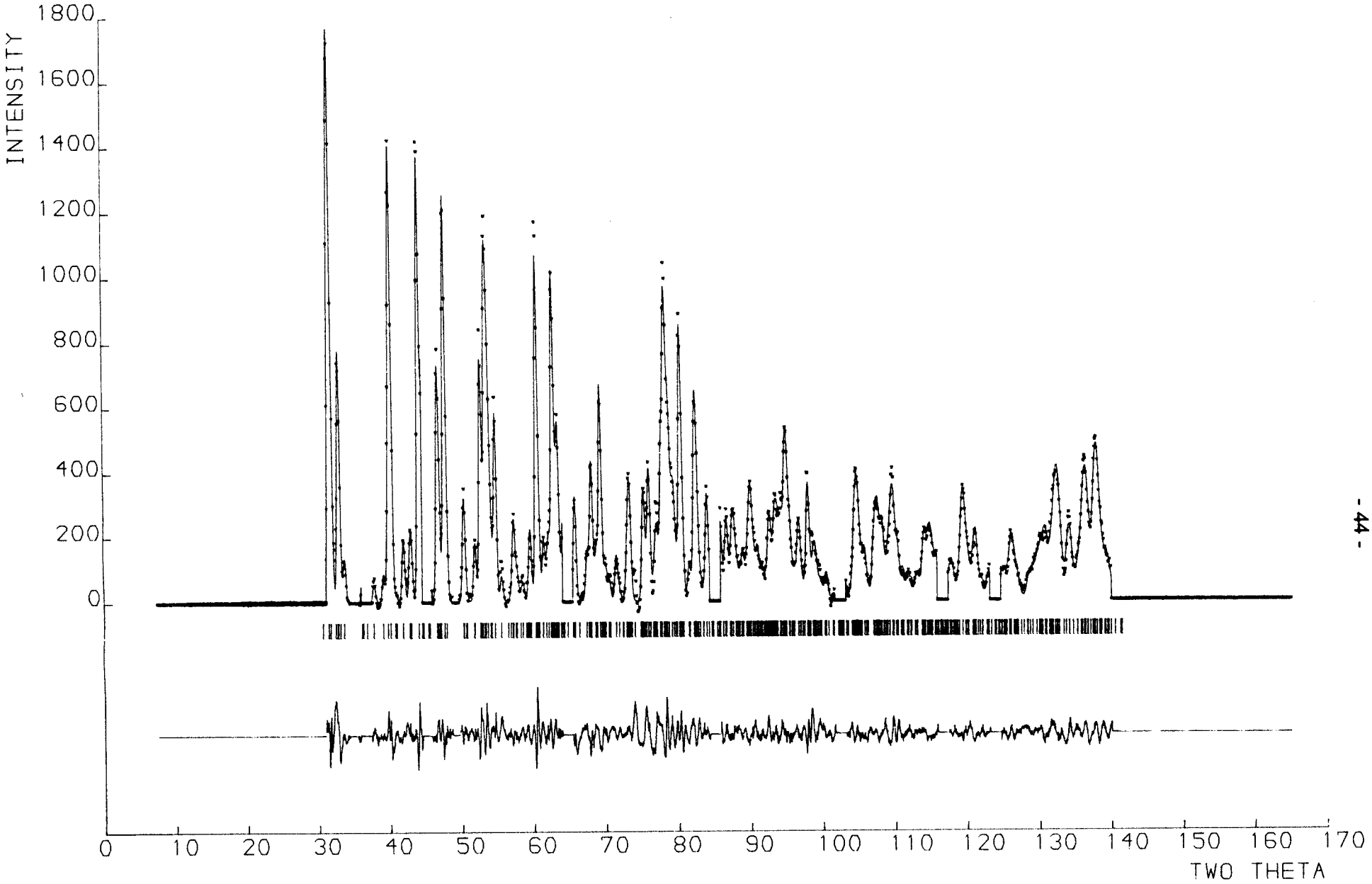

Figure 3.1 Observed (points), calculated (upper continuous line) and difference (lower continuous line) profiles for $MoO_2DPO_4.D_2O$. Vertical strokes mark the position of each reflection in the profile.

Table 3.2 Structure of $MoO_2DPO_4.D_2O$

(e.s.d.'s in parentheses)

Space Group $P2_1/m$ (No. 11 International Tables).
Unit Cell Dimensions: a=6.7104(2) Å, b=6.3437(2) Å, c=6.9864(2) Å
$\alpha=\gamma=90°$, $\beta=109.892(1)°$

Atom	Position	x	y	z	$^{\dagger}B_{eq}/Å^2$
Mo	2e	0.27699(43)	0.25	0.17815(53)	2.12(13)
P	2e	0.66761(46)	0.25	0.66691(48)	1.88(14)
O(1)	4f	0.67911(39)	0.43443(34)	0.81103(29)	1.52(10)
O(2)	2e	0.46572(44)	0.25	0.48227(41)	2.65(17)
O(3)	2e	0.84126(55)	0.25	0.56977(53)	0.92(13)
O(4)	2e	0.20143(48)	0.25	0.91289(41)	1.25(14)
O(5)	2e	0.60644(56)	0.25	0.15486(87)	2.77(18)
O(6)	2e	0.04725(54)	0.25	0.22267(46)	2.25(17)
D(1)	2e	0.98517(48)	0.25	0.68544(40)	2.05(17)
D(2)	2e	0.73357(58)	0.25	0.28638(59)	2.66(17)
D(3)	2e	0.65392(71)	0.25	0.03969(67)	4.16(23)

Anisotropic Thermal Parameters

Atom	β_{11}	β_{22}	β_{33}	β_{12}	β_{13}	β_{23}
Mo	0.0080(8)	0.0137(9)	0.0202(9)	0.0	0.0195(8)	0.0
P	0.0084(8)	0.0207(15)	0.0063(7)	0.0	0.0010(6)	0.0
O(1)	0.0074(7)	0.0134(7)	0.0038(4)	0.0110(5)	-0.0053(3)	0.0010(5)
O(2)	0.0008(8)	0.0368(24)	0.0085(5)	0.0	-0.0035(4)	0.0
O(3)	0.0102(10)	0.0040(9)	0.0033(7)	0.0	0.0056(7)	0.0
O(4)	0.0127(10)	0.0019(9)	0.0015(7)	0.0	-0.0135(6)	0.0
O(5)	0.0038(9)	0.0193(17)	0.0258(13)	0.0	0.0080(9)	0.0
O(6)	0.0074(9)	0.0285(17)	0.0044(8)	0.0	0.0003(7)	0.0
D(1)	0.0030(9)	0.0308(14)	0.0019(7)	0.0	-0.0046(7)	0.0
D(2)	0.0133(11)	0.0070(10)	0.0205(10)	0.0	-0.0073(8)	0.0
D(3)	0.0247(13)	0.0435(23)	0.0108(10)	0.0	0.0171(10)	0.0

$R_I=4.49\%$, $R_{wp}=9.20\%$, $R_{exp}=3.56\%$.

$$^{\dagger}B_{eq} = \frac{4}{3}[a^2\beta_{11}+b^2\beta_{22}+c^2\beta_{33}+ab(\cos\gamma)\beta_{12}+ac(\cos\beta)\beta_{13}+bc(\cos\alpha)\beta_{23}]$$

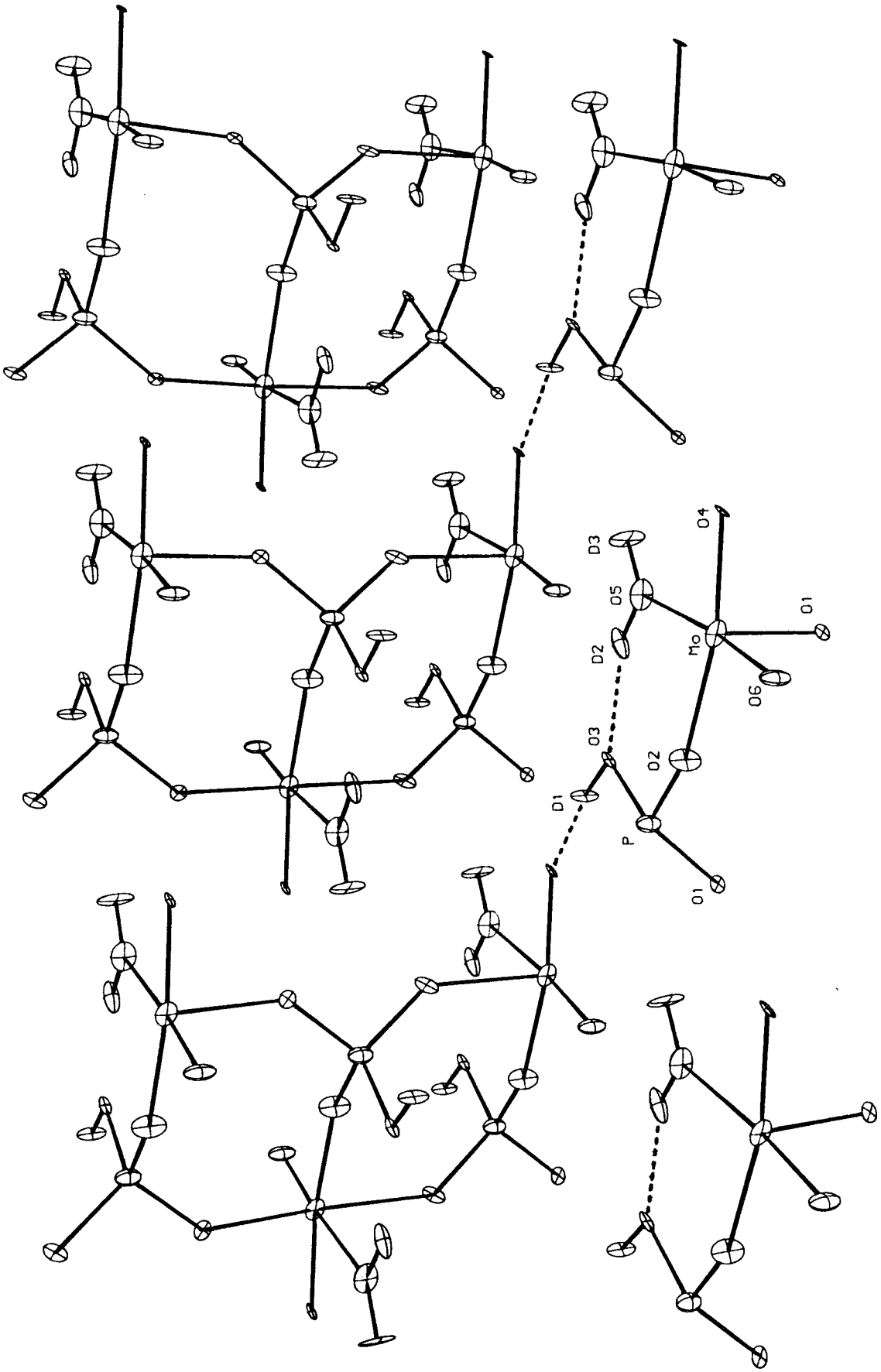

Figure 3.2 Portion of the structure of $MoO_2DPO_4.D_2O$ viewed obliquely to the y=0.25 plane. The hydrogen bonds are represented by broken lines.

Table 3.3 Interatomic Distances and Angles in $Mo_1^{O_2}DPO_4.D_2O$

(e.s.d.'s in parentheses)

Mo-O(1)	2.021(4)	P-O(1)	1.528(3)
Mo-O(2)	2.071(4)	P-O(2)	1.520(4)
Mo-O(4)	1.747(3)	P-O(3)	1.535(4)
Mo-O(5)	2.271(6)		
Mo-O(6)	1.673(3)	O(3)-D(1)	1.027(4)
		O(5)-D(2)	1.019(6)
D(1)...O(4)	1.750(4)	O(5)-D(3)	0.961(6)
D(2)...O(3)	1.862(4)	D(2)...D(3)	1.621(4)
O(4)-Mo-O(6)	104.1°	D(2)-O(5)-D(3)	109.9°
O(6)-Mo-O(2)	95.2°	P-O(3)-D(1)	107.7°
O(4)-Mo-O(5)	82.1°	O(3)-D(1)...O(4)	169.1°
O(2)-Mo-O(5)	78.6°	O(5)-D(2)...O(3)	149.5°
O(1)-Mo-O(2)	86.1°	O(1)-P-O(2)	112.9°
O(1)-Mo-O(4)	91.5°	O(1)-P-O(3)	114.6°
O(1)-Mo-O(5)	82.5°	O(2)-P-O(3)	102.5°
O(1)-Mo-O(6)	97.2°		

All distances are given in Ångströms

The presence of the D_2O moiety accounts for the strong absorption at 1620 cm^{-1} in the infrared spectrum of $MoO_2HPO_4.H_2O$ and its geometry is typical of that of water in hydrated inorganic compounds. It is held in the y=0.25 plane by a weak hydrogen bond between D2 and O3. The distance between D1 and O4 in the neighbouring chain also suggests the presence of a hydrogen bond which thus links together the infinite chains in one direction perpendicular to the *b*-axis.

3.6 Thermogravimetric Analysis

Approximately 19 mg of sample was analysed by heating from 20 to 500 °C in air. The TGA and DTG plots for $MoO_2DPO_4.D_2O$, using a heating rate of 8 °C min^{-1}, are shown in figure 3.3. The plots for the protonated material were essentially identical. It can be seen that weight loss occurs in three stages. In the first stage, starting at *ca.* 60 °C interparticular water is lost, leaving pure $MoO_2DPO_4.D_2O$. Taking this to be the case, then the second stage, starting at *ca.* 150 °C, and the third, starting at *ca.* 260 °C, correspond almost exactly to the loss of half a mole and one mole of water respectively. i.e. the following process occurs:

$$\tfrac{1}{2}[2MoO_3.P_2O_5.3H_2O]$$

$$\downarrow 150\,°C$$

$$\tfrac{1}{2}[2MoO_3.P_2O_5.2H_2O]$$

$$\downarrow 260\,°C$$

$$\tfrac{1}{2}[2MoO_3.P_2O_5].$$

Considering the structure of the compound at 5 K, it might be expected that the mole of water corresponding to the H_2O group is more easily lost than the other half mole, since this requires breaking only one Mo–O bond. At higher temperatures however migration of protons may make the loss of water from the phosphate group more favourable.

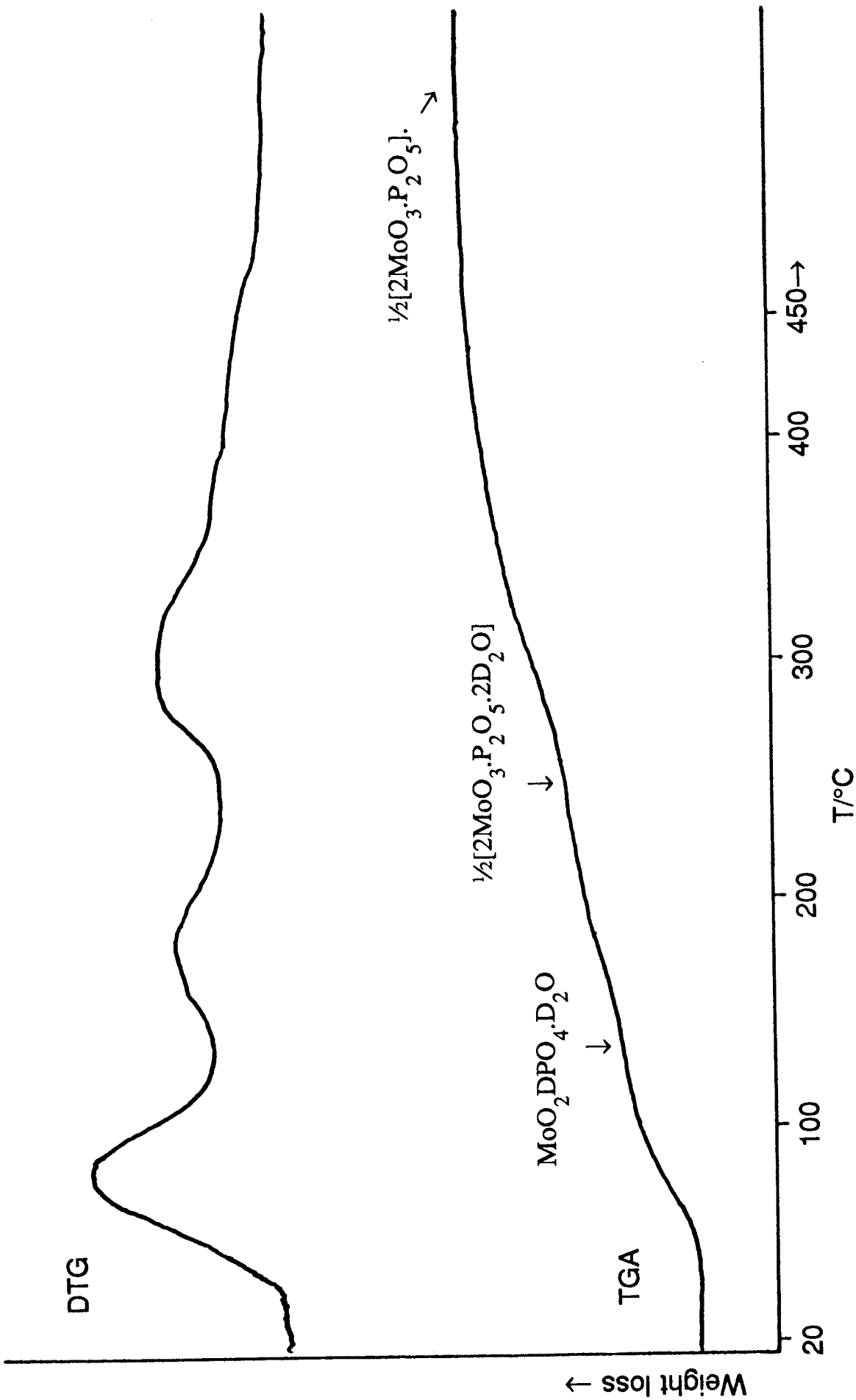

Figure 3.3 Thermogravimetric analysis results for $MoO_2DPO_4.D_2O$, showing weight loss (TGA) and differential weight loss (DTG) curves.

3.7 Nuclear Magnetic Resonance

The ^{31}P magic angle spinning solid state NMR spectrum of $MoO_2HPO_4.H_2O$, recorded at 121.4 MHz, is shown in figure 3.4. A single peak is observed with a chemical shift of –6.26 ppm (referenced to δ=0 for H_3PO_4). Typical values observed for phosphate groups in the solid state lie in the range 0 to –30 ppm. Recent work by Clayden[5] on the ^{31}P MAS-NMR of zirconium hydrogen phosphates has suggested that for $P(OM)_{4-n}(OH)_n$ groups, there is a relationship between n and the chemical shift value. For instance $P(OZr)_4$ has a resonance at -29 ppm whereas $P(OZr)_2(OH)_2$ moieties have chemical shifts of the order of -10 ppm. The value of -6.26 for $MoO_2HPO_4.H_2O$ would suggest that on this basis that the phosphorus tetrahedron is of the form $P(OMo)_2(OH)_2$ or $P(OMo)_3(OH)$, as determined by powder neutron diffraction, rather than the $OP(OMo)_3$ suggested by Kierkegaard.

3.8 Infrared Spectroscopy

The infrared spectrum of $MoO_2HPO_4.H_2O$ is shown in figure 3.5. Between 3000 and 3600 cm^{-1}, three absorption bands due to O–H stretching are observed. A strong, sharp absorption at 1620 cm^{-1} is due to the symmetric bend of water, as discussed previously, and below 1300 cm^{-1} a series of bands due to P–O modes may be observed. Mo–O stretching modes are of no higher energy than 700 cm^{-1}. Using a one-dimensional potential for the hydrogen bond, Lippincott and Schroeder[6] have produced a model which relates O...O distances of hydrogen bonds to the associated O–H stretching frequencies, and which corresponds well with experimental data. Of the three O–H stretching bands in the spectrum of $MoO_2HPO_4.H_2O$, the broad absorption of lowest energy is centred at 3190 cm^{-1}. According to Lippincott and Schroeder, this corresponds to an O...O distance of 2.76 Å. From the neutron diffraction study the distance O(3)...O(4) is 2.765 Å and the angle O(3)–D(1)...O(4)

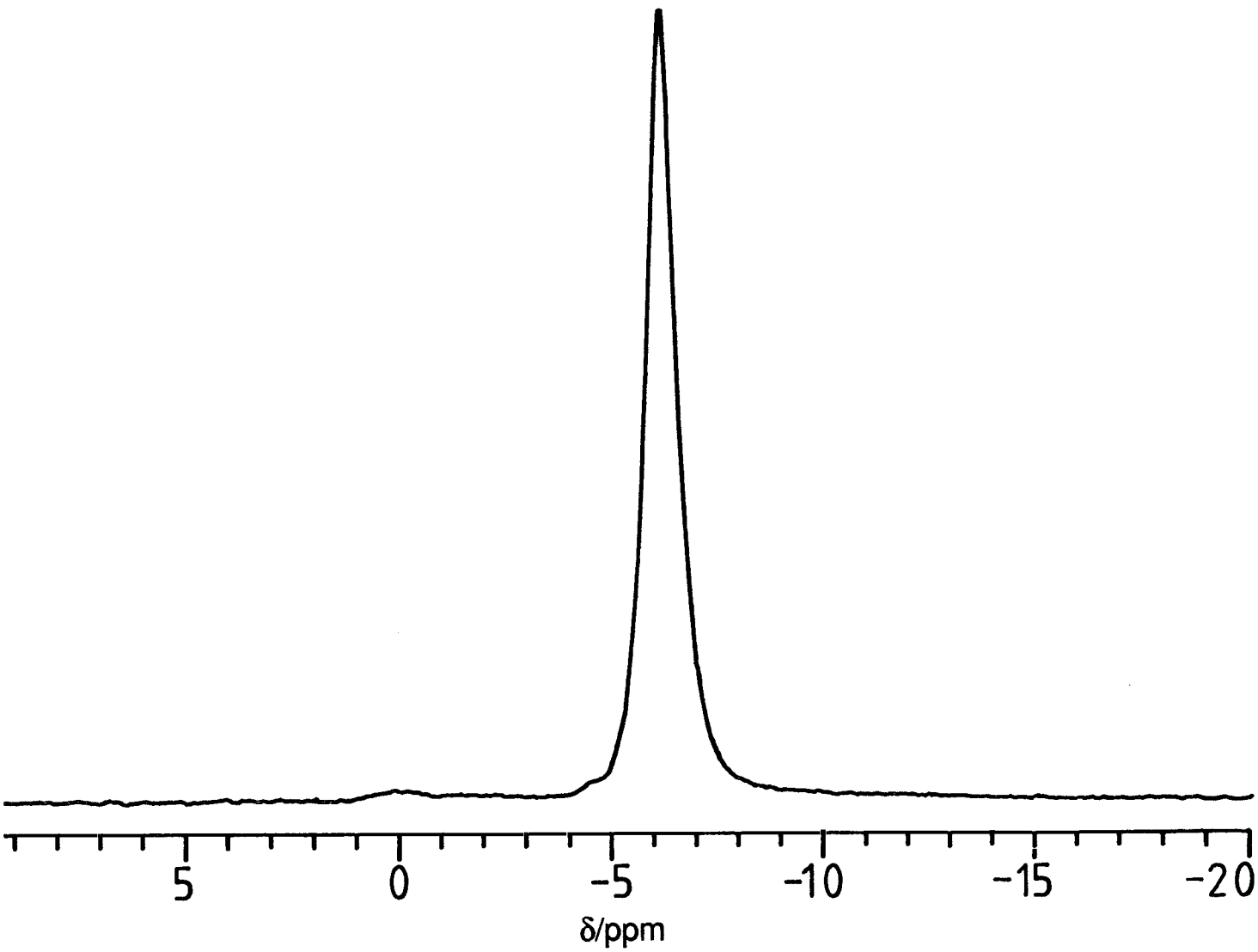

Figure 3.4 Solid State ^{31}P NMR spectrum of $MoO_2HPO_4.H_2O$ (frequency 121.4 MHz, referenced to δ=0 for H_3PO_4).

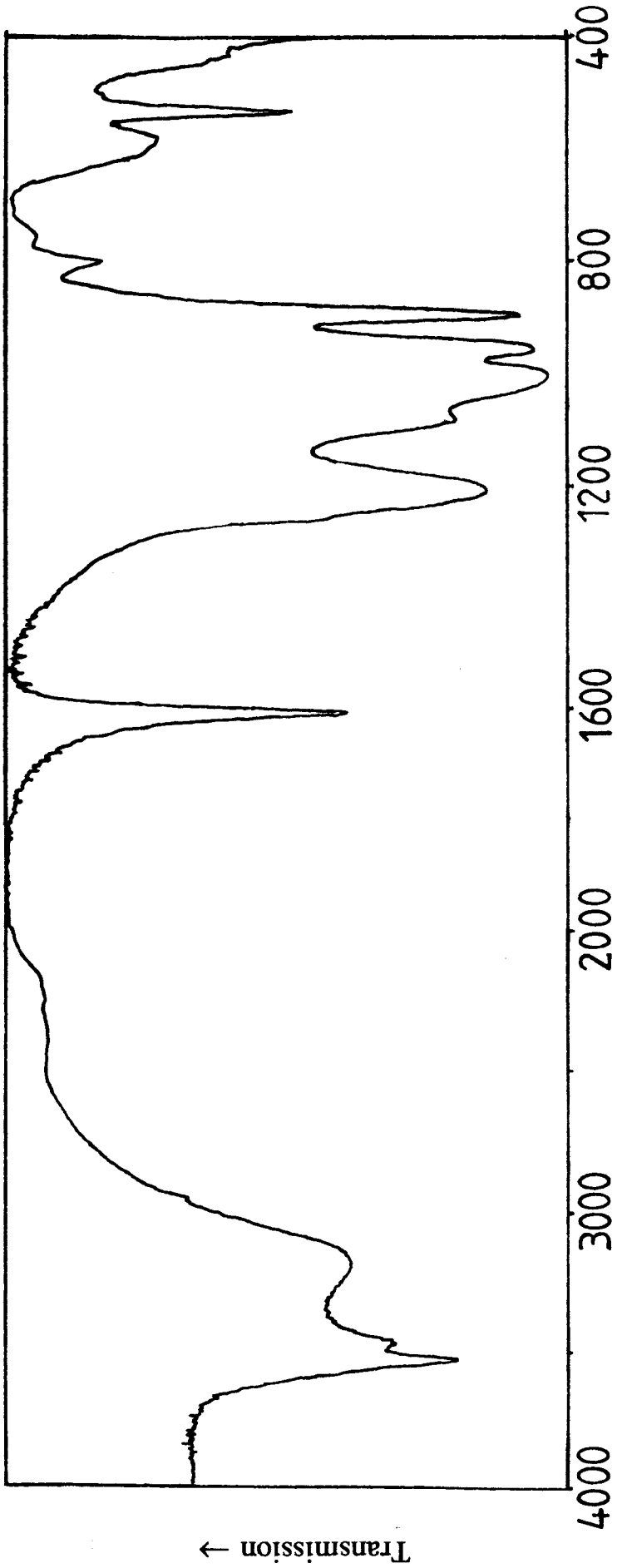

Figure 3.5 Infrared spectum of $MoO_2HPO_4.H_2O$ in the region 4000-400 cm^{-1}, recorded as a pressed CsI disc.

169.1°. This therefore fits well with the assignment of the O(3)–D(1) stretch to this absorption. The other two bands are therefore presumably the symmetric and antisymmetric stretching modes, at 3535 and 3480 cm^{-1} respectively, of the H_2O species in the structure. Since a single isolated O–H group is not involved, the model of Lippincott and Schroeder is invalid, and in fact would predict an O...O distance greater then the 1.788 Å found for O(5)...O(3). In addition the angle O(5)–D(2)...O(3) is, at 149.5°, somewhat lower than that typically found for hydrogen bonding in inorganic compounds.

The spectrum of the deuterated compound, shown in figure 3.6, is essentially identical with that of $MoO_2HPO_4.H_2O$ below 1200 cm^{-1}. At higher frequency, two sharp O–D stretching bands appear at 2642 and 2555 cm^{-1}. These are assigned to the symmetric and antisymmetric stretching modes of D_2O, with the broad absorption at *ca.* 2380 cm^{-1} corresponding to the phosphate O–D stretch. It also seems likely that the symmetric bend of D_2O occurs at around 1190 cm^{-1}, although this is partially masked by a broad P–O stretching band. It can be seen that a certain amount of H_2O adsorption and proton-deuteron exchange has occurred during the preparation of the infrared sample, with absorption in the region 3100-3600 cm^{-1}, at 1610 cm^{-1} and at 1420 cm^{-1} (probably the bending mode of HDO).

3.9 Proton Conductivity

A.c. conductivity measurements, as described in chapter 2, were performed on samples of $MoO_2HPO_4.H_2O$. The samples were pelletised and thin gold films sputtered onto opposite sides. The pellets were then installed in the cell between gold foil electrodes. The sample temperature was controlled using a water bath. Three samples were examined of which two were derived from a single preparation of $MoO_2HPO_4.H_2O$ and had been washed with acetone, and the third of which was

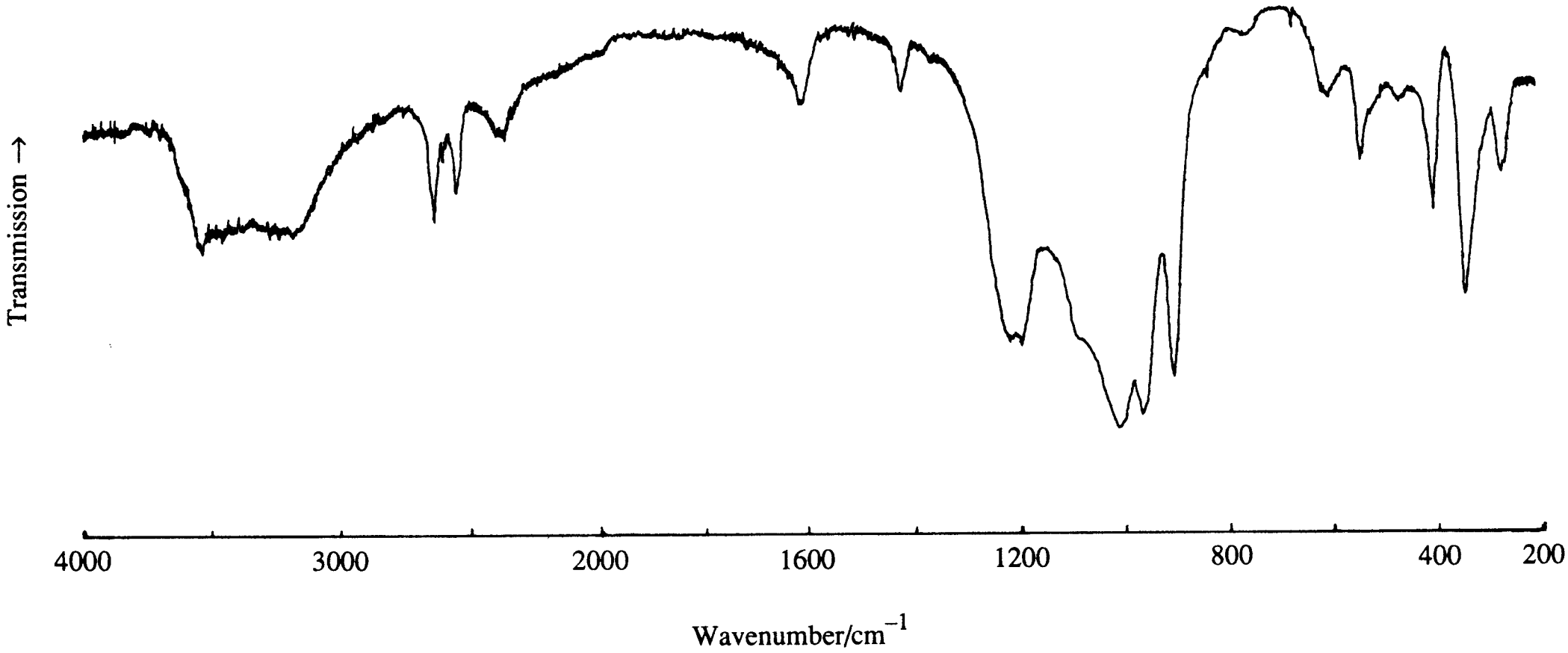

Figure 3.6 Infrared spectum of $MoO_2DPO_4.D_2O$, recorded as a pressed CsI disc.

from a second preparation and washed finally with diethyl ether. Measurements were taken in the region 0 to 50 °C, with low temperature data being recorded initially.

Conductivity data for the three samples are shown in figure 3.7. The data represented by squares and circles are from the two acetone-washed samples, whereas the diamonds refer to the ether-washed preparation. Typical room temperature conductivities were of the order of $1.5\times10^{-5}\,(\Omega\text{cm})^{-1}$. This lies towards the lower end of the range typical for hydrated inorganic conductors (see section 1.4), being lower than the values for HUP or α–ZrP but an order of magnitude higher than that found in $H_3O^+\beta''$–alumina. In the plots, a linear Arrhenius-type behaviour is observed below 25 °C and a least squares fit to these data yielded an activation energy for the conduction process of $37.5(\pm4)\,\text{kJ mol}^{-1}$. Above 30 °C the conductivity begins to fall markedly.

The origin of ionic conductivity cannot be determined by this type of a.c. experiment. It has been suggested that the high conductivities observed are due to phosphoric acid adhering to the crystallites. It is possible that such a mechanism is operating in the case of $MoO_2HPO_4.H_2O$. However the material was washed thorougly with organic solvents, and in addition the high activation energy observed, compared with $20\,\text{kJ mol}^{-1}$ for HUP[7], would seem to preclude a mechanism based on interparticular acid. If proton conductivity is a true bulk property of the material, one possible mechanism could involve a Grotthus-type migration of protons along the hydrogen-bonded network, perpendicular to the crystallographic *c*–axis (see figure 3.2). The absence of free water molecules, which are thought to make an important contribution to bulk proton conduction in HUP and α-ZrP, would account for the higher activation energy in this case, with all the protons in effect bound to the framework.

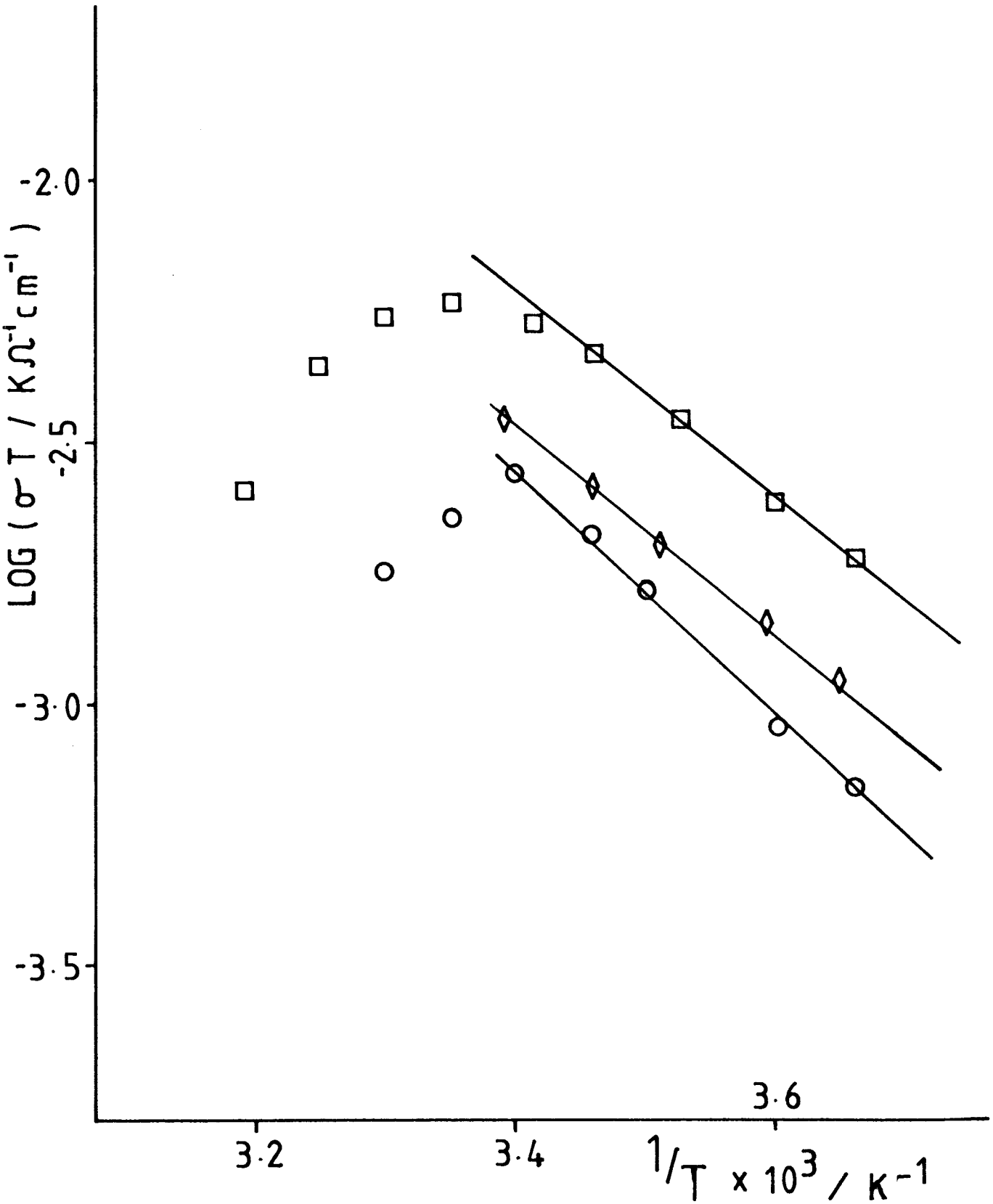

Figure 3.7 Conductivity data for pellets of $MoO_2HPO_4.H_2O$. The three samples comprise two prepared in the same batch and washed with acetone (data represented by squares and circles) and one washed with dried ether (diamonds).

CHAPTER 4

STRUCTURE OF CUBIC $HSbO_3.xH_2O$

4.1 Introduction

As described in chapter 1, three types of hydrated antimonate $HSbO_3.xH_2O$ are known, whose structures are based respectively on the ilmenite, pyrochlore and cubic (Im3) polymorphs of $KSbO_3$. Chowdhry and co-workers[1] have carried out a study of these three types using thermogravimetric analysis, infrared spectroscopy, NMR and proton conductivity techniques and showed that each has a room temperature conductivity of the order of $10^{-3}\,(\Omega cm)^{-1}$ and which is strongly dependent on water content. This suggests that a model for proton mobility based on the Grotthus mechanism is applicable for these hydrates.

Of particular interest is the cubic polymorph of $HSbO_3.xH_2O$ since two distinct sites for cavity water have been identified. The unique framework structure of cubic $KSbO_3$ (space group Im3) is retained on ion exchange to form the hydrated oxide and consists of a network of pairs of edge-sharing SbO_6 octahedra themselves linked by corner-sharing. Tunnel-like cavities extend in three dimensions throughout the structure in the <111> direction, intersecting at the origin and body-centre positions. Three corner-sharing oxygens, situated on 24g sites about the three-fold [111] axis, define the narrowest part of the tunnels where they have a diameter of about 2.5 Å.

Watelet et al.[2] carried out a single crystal x-ray diffraction study on hydrated and partially dehydrated phases of this polymorph and found "H_3O" species in the cavities situated on two partially occupied 16f sites, that is on (x,x,x), one close to the plane formed by the three 24g oxygens and the other closer to the crystallographic origin along the [111] axis. The ratio of the occupancy of the former site

over that of the latter was found to decrease with decreasing water content. From this x-ray work it was impossible to locate the hydrogen positions and it was consequently unclear as to whether the water is present as hydronium ions, as separate water molecules and framework-bound protons or as a combination of both. The proton NMR data of Chowdhry et al. supported the existence of hydronium ions, in contrast to other hydrated oxides such as $H_2Ta_2O_6.xH_2O$[3] and $H_2OHTaWO_6$[4] where low temperature powder neutron diffraction and NMR studies have shown the existence of distinct H_2O and OH groupings.

In order to resolve these possible forms, a powder neutron study was undertaken on fully deuterated samples of cubic $DSbO_3.xD_2O$. A preliminary study of proton motion in $HSbO_3.xH_2O$ by quasielastic neutron scattering is described in chapter 5.

4.2 Synthesis

$HSbO_3.xH_2O$ was prepared by ion exchange of $KSbO_3$ in aqueous sulphuric acid. Cubic $KSbO_3$ was prepared as described by Chowdhry et al.[1]: a mixture containing an approximately 1:1 weight ratio of KF (BDH, AnalaR) and $KSb(OH)_6$ was intimately comminuted and then heated in a platinum crucible at 1000 °C in air for 12 h. The white product was then reground, washed thoroughly with distilled water and dried by heating at 150 °C for 24 h. The ion exchange was effected by reaction of the $KSbO_3$ with a 3M solution of H_2SO_4 (May & Baker, Lab. Reag.), about 250 cm^3 being used for 5 g of $KSbO_3$. The reaction mixture was stirred at *ca.* 50 °C for 3 days and the exchanged product then filtered off and washed thoroughly. A similar procedure was adopted for the preparation of deuterated samples: the $KSbO_3$ was exchanged in an approximately 3M solution of D_2SO_4, made from D_2SO_4 (BDH, >99% D) and D_2O (BDH, >99.96% D), 100 cm^3 of solution being used for 5 g of $KSbO_3$. All operations were carried out in H_2O-free conditions under an

atmosphere of dry nitrogen, with sample handling taking place in a glove box and the ion exchange being effected in stoppered flasks. The white deuterated samples were washed with D_2O. Two samples were prepared of which one was simply stored in a doubly sealed bottle over $CaCl_2$ while the other was first dried by heating at *ca.* 50 °C under vacuum.

4.3 Characterisation

Powder X-Ray Diffraction

The $KSbO_3$ used in this work was found to be a pure, highly crystalline cubic phase of lattice parameter 9.615(3) Å, which compares with a value of 9.56 Å given in the original work of Spiegelberg[5]. All reflections could be indexed on the basis of a body-centred unit cell, and are given in table 4.1. Similarly, samples of $HSbO_3.xH_2O$ gave diffraction patterns which could be indexed using a body-centred unit cell. A typical lattice parameter was 9.526 Å (see table 5.1). The undried deuterated sample used for powder neutron diffraction showed itself to be a pure material with no diffraction peak arising from impurity. The pattern was indexed in the space group Im3 and the lattice parameter refined as 9.549(4) Å.

Flame Photometry

The concentration of potassium in the acidic supernatant after the ion-exchanged product had been filtered off was determined by flame photometry. The instrument was calibrated with standard solutions as described in chapter 2. For the undried sample, the result corresponded to 97(±5)% of the potassium content of the parent compound, assuming that this was a pure phase of $KSbO_3$.

Thermogravimetric Analysis

TGA was carried out using a Stanton thermobalance. About 1.0 g of the undried

Table 4.1 Observed and Calculated Powder Diffraction Data for $KSbO_3$.

h k l	*2θ(obs)*	*2θ(calc)*
1 1 0	13.00	13.01
2 0 0	18.44	18.44
2 1 1	22.64	22.63
2 2 0	26.20	26.19
3 1 0/1 3 0	29.36	29.35
2 2 2	32.25	32.22
3 2 1/2 3 1	34.89	34.89
4 0 0	37.39	37.38
4 1 1/3 3 0	39.73	39.74
4 2 0/2 4 0	41.98	41.99
4 2 2	46.18	46.22
5 1 0/1 5 0/4 3 1/3 4 1	48.20	48.22
5 2 1/2 5 1	52.02	52.05
5 3 0/3 5 0/4 3 3	55.67	55.70
6 0 0/4 2 2	57.47	57.46
6 1 1/5 3 2/3 5 2	59.27	59.19
6 2 0/2 6 0	60.90	60.89
5 4 1/4 5 1	63.53	63.56
6 3 1/3 6 1	65.81	65.83
4 4 4	67.43	67.43
7 1 0/1 7 0/5 5 0/5 4 3/4 5 3	68.99	69.01
6 4 0/4 6 0	70.57	70.58
7 2 1/2 7 1/6 3 3/5 5 2	72.08	72.13

λ=1.5406 Å

a=9.615(3) Å

deuterated sample was heated to 700 °C. A DTG curve was derived which was similar to the one reported by Chowdhry et al.[1] except for the presence of a larger amount of interparticular water, whose loss in the region 40–80 °C partially masked that of the cavity water. However it was possible to determine the composition of the dried sample as $DSbO_3.0.8(\pm0.1)D_2O$. In the structure refinement described below, the composition of best agreement emerges as $DSbO_3.0.81(\pm0.03)D_2O$. For convenience the compound is referred to in this work from now on as $DSbO_3.0.81D_2O$.

Electron Microscopy/EDAX

Using the technique described in chapter 2, the relative proportions of the heavier elements present, in this case potassium and antimony, were determined by analysis of certain x-rays (K_K and Sb_L) emitted whilst the samples were mounted in a scanning electron microscope. As stated previously, the errors inherent in this method are difficult to estimate, but were of the order of 2–3%. The samples analysed were high purity $KSb(OH)_6$ (used in the synthesis of $KSbO_3$), $KSbO_3$ and $DSbO_3.0.81D_2O$. The results were (in percentage ratio by weight):

$KSb(OH)_6$	Sb 77.8,	K 22.2	(theoretical:	75.7, 24.3)
$KSbO_3$	Sb 78.5,	K 21.5	("	75.7, 24.3)
$DSbO_3.0.81D_2O$	Sb 97.9,	K 2.1	("	100.0, 0.0)

Infrared Spectroscopy [6]

Infrared spectra were recorded of $KSbO_3$, $HSbO_3.xH_2O$ and $DSbO_3.0.81D_2O$ as pressed CsI discs, and are shown in figure 4.1. The spectrum of $KSbO_3$ is essentially featureless above 800 cm^{-1}. At lower frequency vibrations of the SbO_3^- framework are observed with strong features at 645, 554 and 373 cm^{-1}. These features are also observed in the other two spectra, although less well-resolved.

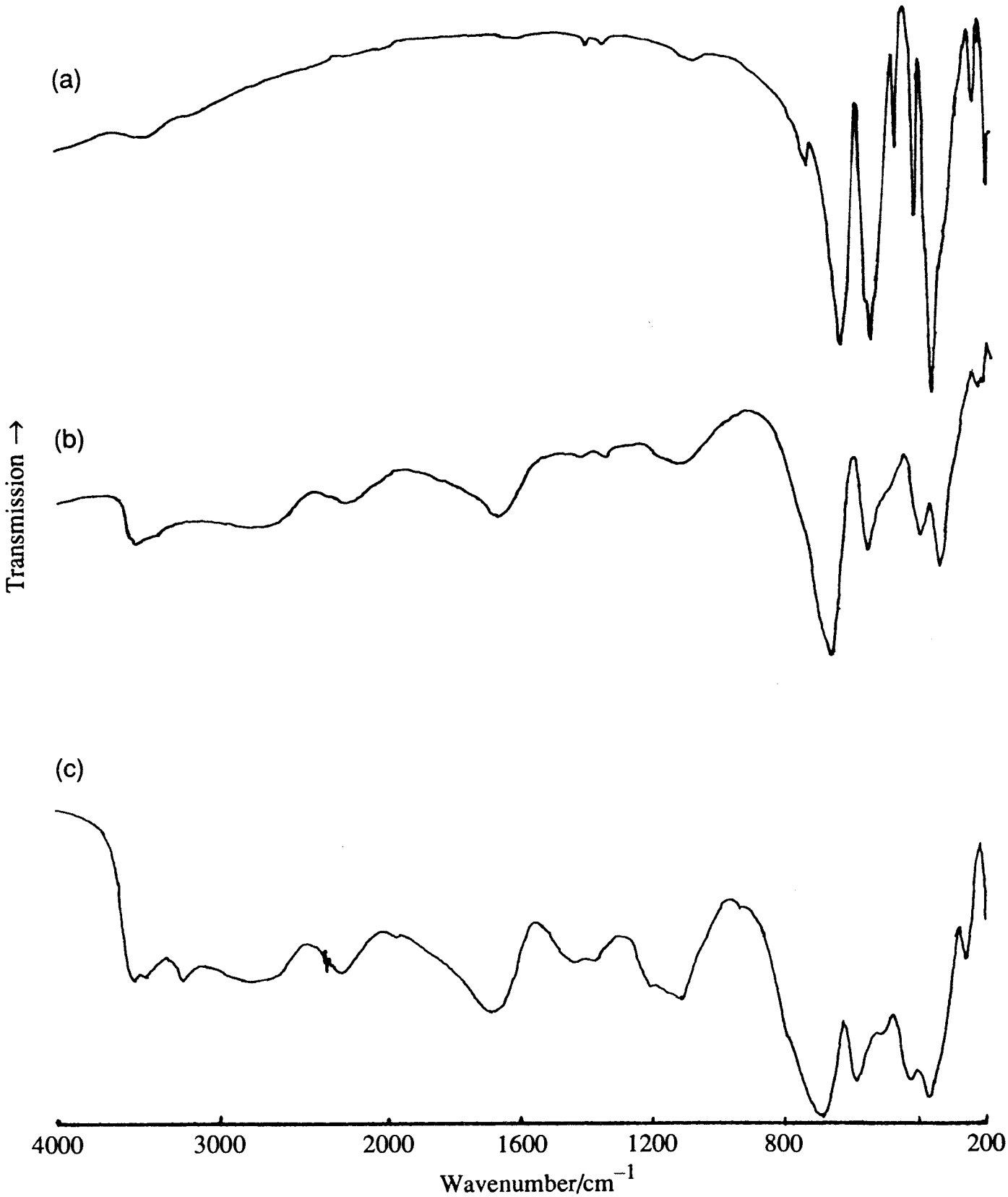

Figure 4.1 Infrared spectra of (a) $KSbO_3$, (b) $HSbO_3.xH_2O$ and (c) $DSbO_3.0.81D_2O$, recorded as pressed CsI discs.

For the protonated compound several broad absorptions are observed at higher frequency with those at *ca.* 3530 and 1680 cm^{-1} corresponding respectively to O–H stretching and to bending modes of H_2O and H_3O^+. The broad band at *ca.* 1140 cm^{-1} may also be ascribed to a bending mode of H_3O^+. Assignment of the other broad features is more difficult since they possibly represent combination bands. However the breadth of all the higher frequency bands indicates the presence of hydrogen bonding and of thermal disorder of the cavity species, as might be expected in this proton-conducting material.

Ths spectrum of $DSbO_3.0.81D_2O$ is very similar to that of $HSbO_3.xH_2O$ demonstrating that substantial proton-deuteron exchange must have occurred during the preparation of the sample disc. However the greater intensity of absorption between 1100 and 1200 cm^{-1} may be assigned to bending modes of the residual deuterated species.

4.4 Powder Neutron Diffraction

Powder neutron diffraction data were collected at room temperature on the D2B diffractometer at the I.L.L, Grenoble. As described previously for $MoO_2DPO_4.D_2O$, the samples, of approximately 5 g mass, were contained in a thin-walled vanadium can sealed with an indium wire gasket. The diffractometer was again operating at a wavelength of 1.595 Å and the profile was collected in 2θ steps of 0.025° between 0° and 180°. The instrument was operating in high resolution mode.

The spectrum obtained for $DSbO_3.0.81D_2O$ is shown in figure 4.2 and is of high quality. All the diffraction peaks could again be indexed on the basis of a cubic unit cell of space group Im3 whose cell parameter, obtained from the profile refinement, was 9.5505(5) Å. Some diffuse scattering was observed at low angles, and data below

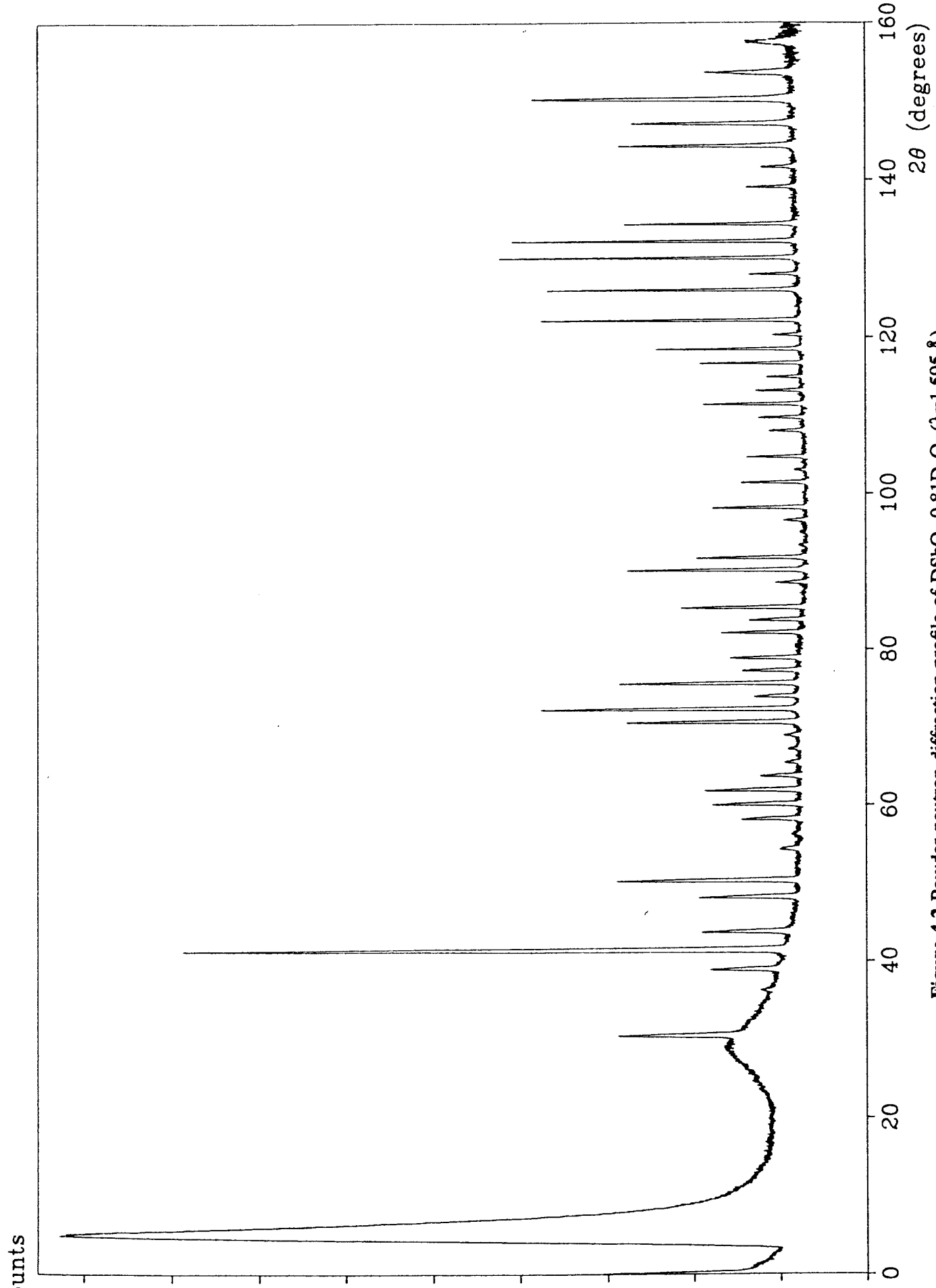

Figure 4.2 Powder neutron diffraction profile of $DSbO_3.0.81D_2O$. (λ=1.595 Å).

30° were accounted for by fitting the background to this "hump".

The data were fitted using the Rietveld refinement program previously described. The background was determined manually at as many points as possible between diffraction peaks by averaging over a short range of data points. The atomic scattering lengths were taken as

$$\text{Sb } 0.564,\ \text{O } 0.580,\ \text{D } 0.667\ (\text{all} \times 10^{-14}\text{m})$$

The refinement was carried out in the space group Im3 with the origin taken at m3. The antimony atoms were first placed on the 12e sites and the framework oxygen atoms on 12d and 24g sites, following the work of Watelet et al. The scale factor, halfwidth parameters, cell parameter and zeropoint were then refined and none produced an unusual value. Atomic positions and temperature factors were then refined and an intensity R factor of about 34% achieved. At this stage a Fourier summation was computed on sections through the asymmetric one eighth of the unit cell (figure 4.3) and from this the two extra-framework oxygen positions were easily identified on 16f sites (x,x,x) close to those found in the previously reported structure (x=0.16 and x=0.10). In addition a strong peak at approximately (0.23, 0.10, 0.24) and equivalent positions could be assigned to deuterium atoms D(1) since they lay at a distance of approximately 1 Å from the cavity oxygen O(3) at (0.16, 0.16, 0.16). These atoms were incorporated into the refinement and all atomic positions and isotropic temperature factors then refined together with the occupancies for the cavity atoms. The best fit was achieved with the occupancy of D(1) having refined to close to three times of that O(3), that is with a symmetrical D_3O species, each D being on an equivalent site related to the other two by rotation about the [111] axis. The occupation factors for O(3) and D(1) were subsequently constrained to be in the ratio 1:3. At this stage R_I fell to 14%. In order to determine the positions of the

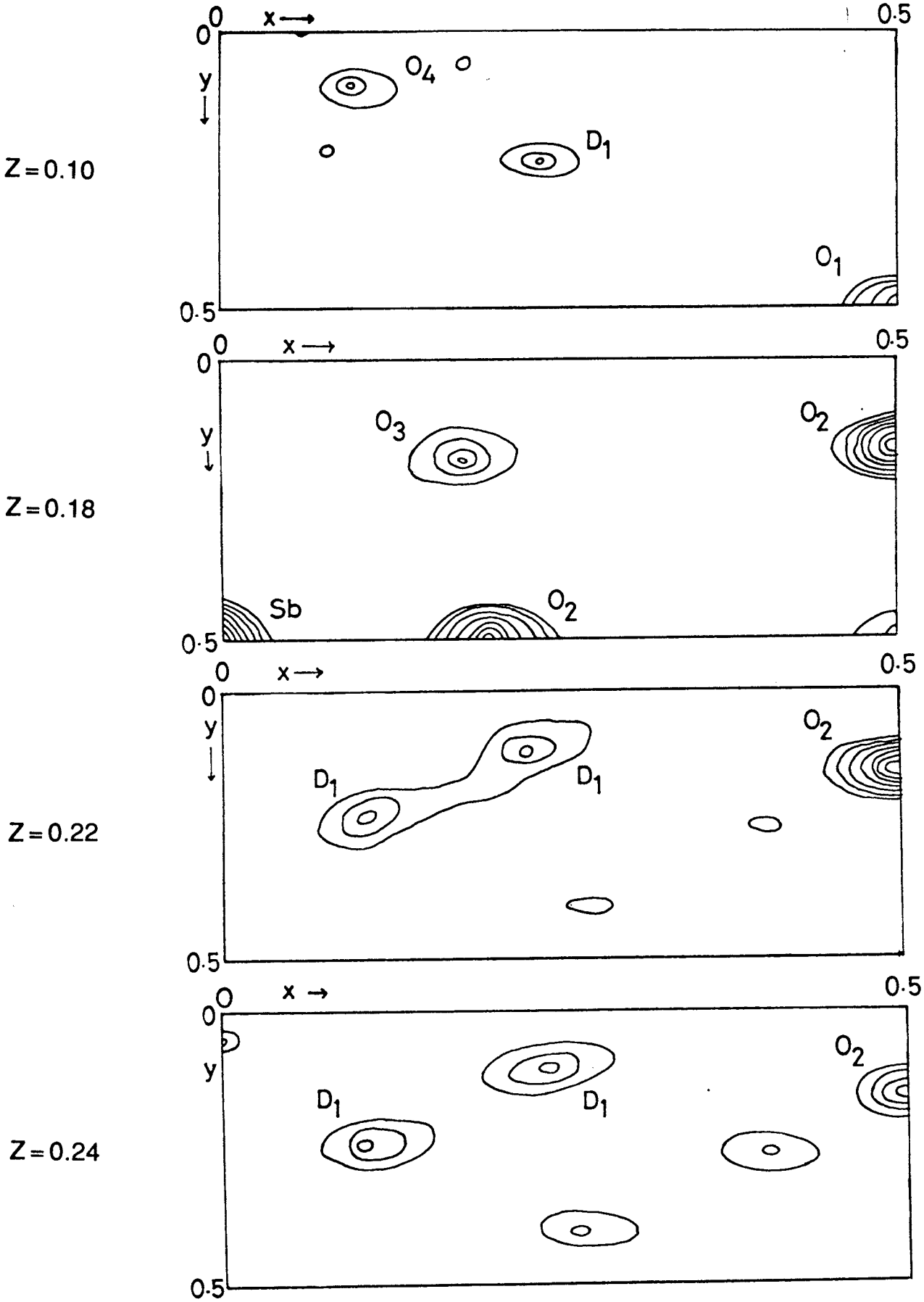

Figure 4.3 Fourier summation maps calculated for *xy* sections of the asymmetric unit of $DSbO_3.0.81D_2O$. (N.b. the diagrams are distorted due to *x* and *y* not being on the same scale.)

deuteriums associated with the other cavity species, Fourier difference maps were then calculated for the same region as before. In the relevant area (figure 4.4), around the [111] axis at x=0.10, new peaks were observed which were however weaker and less well defined than those in the initial Fourier summation, probably due to thermal motion of, or disorder in, this cavity species at room temperature. However it was possible to determine reasonable positions for additional deuterium atoms, D(2) and D(3), at a distance of approximately 1 Å form O(4) on unrelated sites forming a D_2O species with O(4) and another, D(4), bound to the framework oxygen O(1) forming a deuteroxyl group and also at a reasonable hydrogen-bonding distance to O(4). An attempt to fit a second deuteronium ion as an alternative to this model was unsuccessful. Full refinement of this model led to a very close fit to the data, as shown in figure 4.5, and R_I fell to 3.6%. Observed and calculated intensities for the 150 reflections are tabulated in appendix 2.

The final structure, including isotropic atomic temperature factors and occupancies, is given in table 4.2 and bond lengths and interatomic angles are tabulated in table 4.3. As can be seen, the accuracy in position of the deuteriums associated with O(4) is lower than for D(1) and the D_2O bond lengths and angle less well defined but not unreasonable. It should be borne in mind that the interaction of the D_2O species with the lattice is obviously very weak and at room temperature considerable freedom of this species and the hydrogen-bonded D(4) is apparent. It should also be noted that in a non-stoichiometric disordered structure the refined positions represent the average contents of the unit cell.

However an unambiguous definition of the nature of the cavity species has been established together with an accurate framework structure and further improvement would be possible by carrying out neutron diffraction studies at lower temperature.

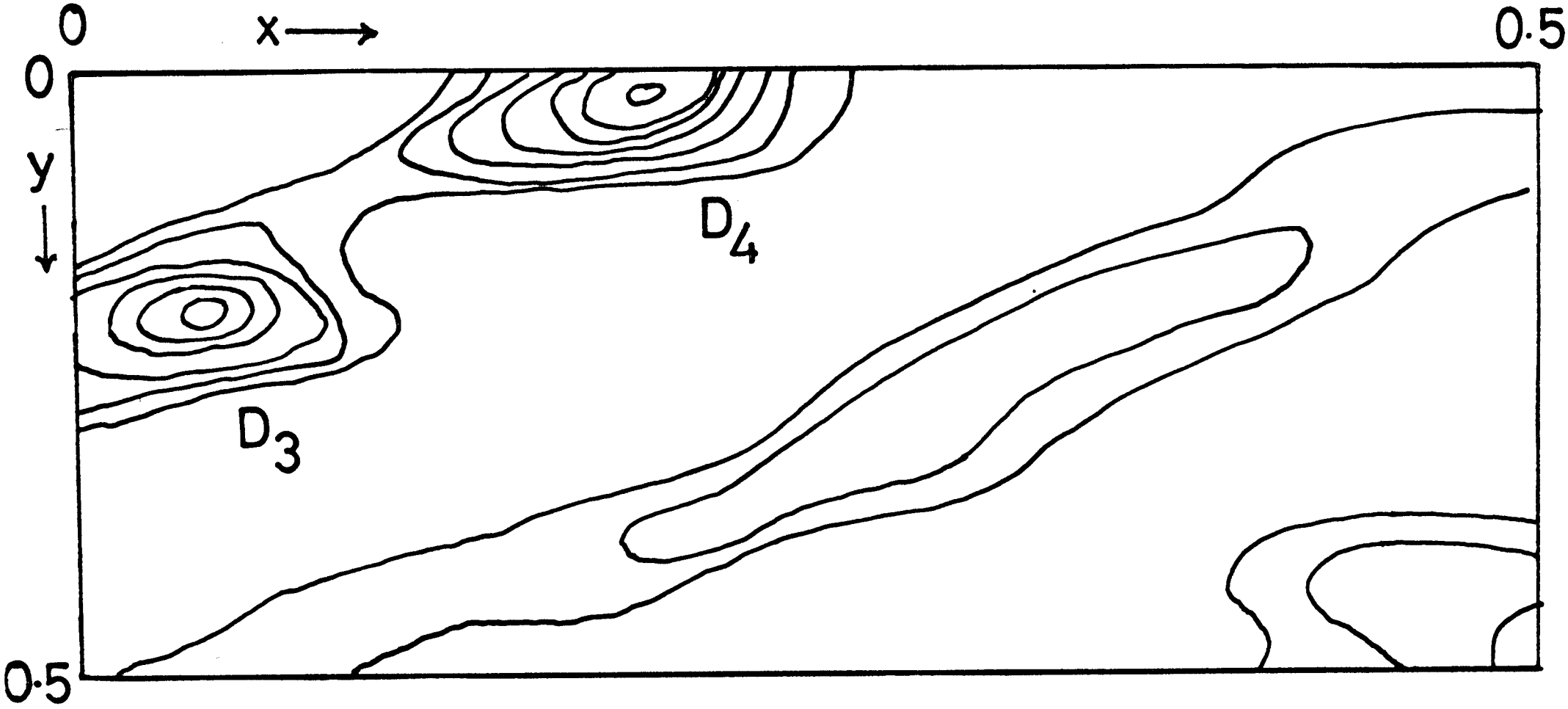

Figure 4.4 Fourier difference map calculated in the plane z=0.16 of the asymmetric unit of $DSbO_3.0.81D_2O$ and showing the positions of D(3) and D(4). (N.b. the diagram is distorted due to x and y not being on the same scale).

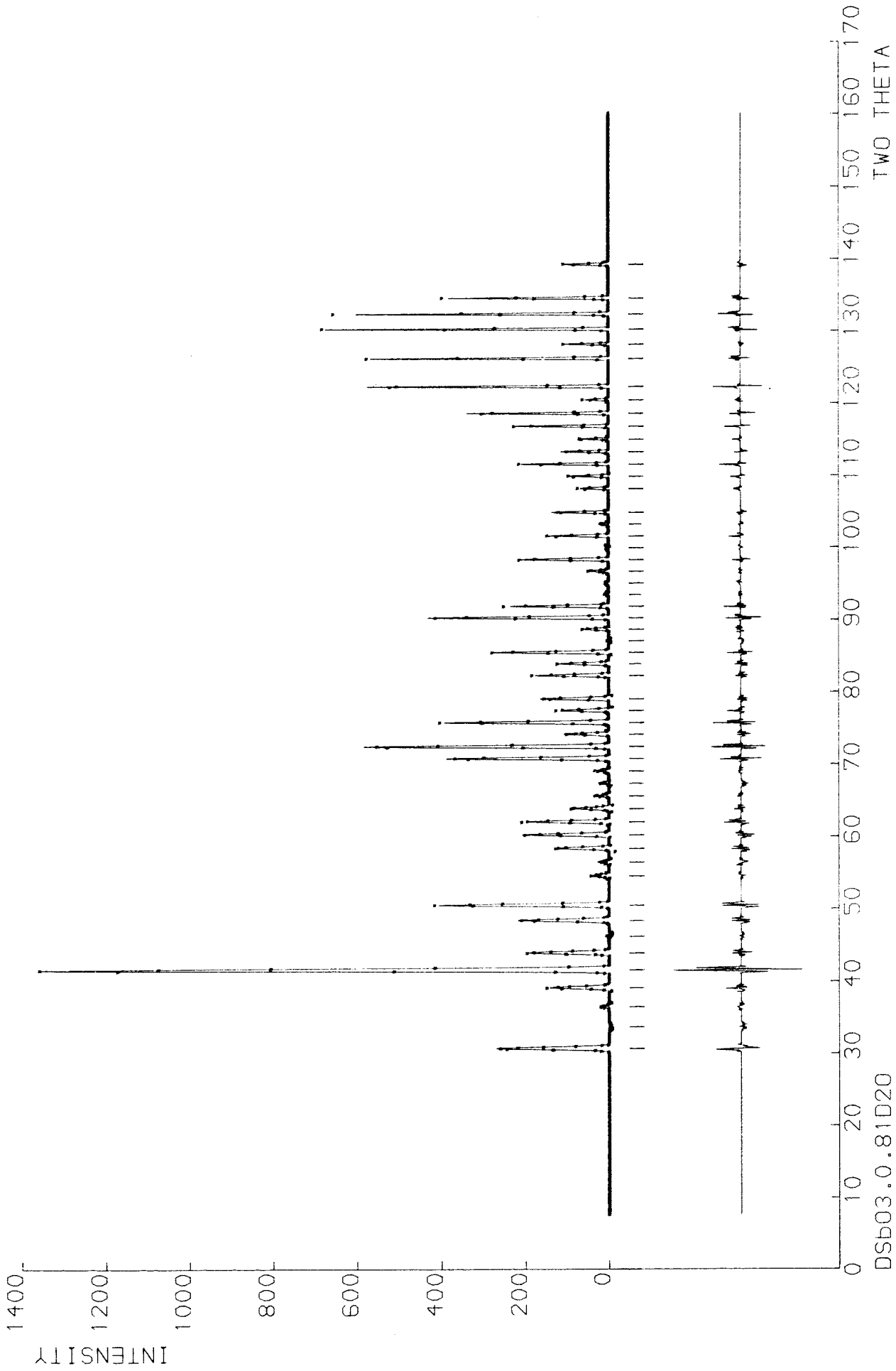

Figure 4.5 Observed (points), calculated (upper continuous line) and difference (lower continuous line) profiles for $DSbO_3.0.81D_2O$. Vertical strokes mark the position of each reflection in the profile.

Table 4.2 Structure of $DSbO_3.0.81D_2O$

(e.s.d.'s in parentheses)

Space Group Im3, Origin at m3 (No. 204 International Tables).
Unit Cell Dimensions: a=b=c=9.5505(1)Å, α=β=γ=90°.

Unit Cell Content			
12	Sb	12e	(x,0,½)
12	O(1)	12d	(x,0,0)
24	O(2)	24g	(0,y,z)
5.30	O(3)	16f	(x,x,x)
15.91	D(1)	48h	(x,y,z)
4.4	O(4)	16f	(x,x,x)
4.4	D(2)	48h	(x,y,z)
4.4	D(3)	48h	(x,y,z)
6.70	D(4)	24g	(0,y,z)

Atom	x	y	z	$B/Å^2$	n
Sb	0.8400(3)	0.0	0.5	0.57(4)	1.0
O(1)	0.3665(3)	0.0	0.0	1.06(6)	1.0
O(2)	0.0	0.3428(3)	0.2912(2)	0.65(3)	2.0
O(3)	0.1671(6)	0.1671(6)	0.1671(6)	0.77(14)	0.442(9)
D(1)	0.2366(5)	0.2244(4)	0.1052(5)	1.89(11)	1.326(26)
O(4)	0.1055(11)	0.1055(11)	0.1055(11)	4.82(46)	0.374(18)
D(2)	0.1919(32)	0.0674(29)	0.1110(37)	4.71(58)	0.374(18)
D(3)	0.0868(19)	0.2016(22)	0.1617(23)	2.60(42)	0.374(18)
D(4)	0.0	0.0480(12)	0.2711(15)	5.62(38)	0.558(9)

R_I=3.60%, R_{wp}=12.78%, R_{exp}=5.88%.

Table 4.3 Interatomic Distances and Angles in $DSbO_3.0.81D_2O$

(e.s.d.'s in parentheses)

(a)	Framework Atoms	
	Sb-O(2) ×2	1.956(4)
	Sb-O(1) ×2	1.990(4)
	Sb-O(2) ×2	1.994(2)
	O(1)-O(1) ×1	2.550(6)
	O(1)-O(2) ×2	2.790(3)
	O(1)-O(2) ×4	2.803(4)
	O(2)-O(2) ×4	2.805(1)
	O(2)-O(2) ×1	3.003(5)
	Sb-Sb	3.056(6)
	O(1)-Sb-O(1) ×1	79.69(3)°
	O(1)-Sb-O(1) ×4	89.43(2)°
	O(1)-Sb-O(1) ×2	89.99(11)°
	O(2)-Sb-O(1) ×4	90.49(14)°
	O(2)-Sb-O(1) ×1	100.28(5)°
(b)	Cavity Species	
	O(3)-D(1)	1.044(11)
	O(3)...O(2)	2.601(6)
	O(3)D(1)...O(2)	1.564(10)
	D(1)-O(3)-D(1)	100.82(11)°
	O(4)-D(2)	0.90(5)
	O(4)-D(3)	1.08(4)
	O(1)-D(4)	1.02(2)
	O(1)...O(4)	0.90(5)
	O(1)D(4)...O(4)	1.954(15)
	D(2)-O(4)-D(3)	118.0(9)°

All distances are given in Ångströms

The sample which had been dried under vacuum gave a very different neutron diffraction profile to that of $DSbO_3.0.81D_2O$, as is shown in figure 4.6. On inspection of the peak positions it was apparent that the greater number of reflections could be accounted for by the formation of a supercell with cell dimensions approximately double those of $DSbO_3.0.81D_2O$. Attempts to index the pattern on tetragonal cells with only one or two parameters doubled left too many peaks unindexed. However using a primitive cubic cell of lattice parameter 18.982(1) Å all but two of the peaks could be accounted for. The data is tabulated in table 4.4.

Unfortunately initial attempts at structure refinement showed that the number of unique atoms required was too large for the profile refinement software at Southampton, and therefore no further structural analysis was carried out.

4.5 Discussion of the Structure

As can be seen from table 4.3, the SbO_3^- framework consists of a network of distorted SbO_6 octahedra in which the angle formed by the two edge-sharing oxygens, O(1), and the central antimony is compressed by about 10° from the ideal 90°. This is complemented by a widening of the corresponding angle involving the two corner-sharing oxygens which lie in the same plane.

The cavity species consist partly as D_3O^+ and partly as D_2O associated with deuterium bound to the lattice. Figure 4.7 shows a portion of the structure viewed approximately perpendicularly to the [111] threefold axis (shown as a broken line). The positions of the deuteronium ion and of the D_2O and associated OD grouping are shown respectively in (a) and (b) in relation to the positions of framework oxygens which lie perpendicular to the axis. It can be seen that the symmetry of the O(3) site and the proximity of the three equivalent framework oxygens O(2) form an ideal

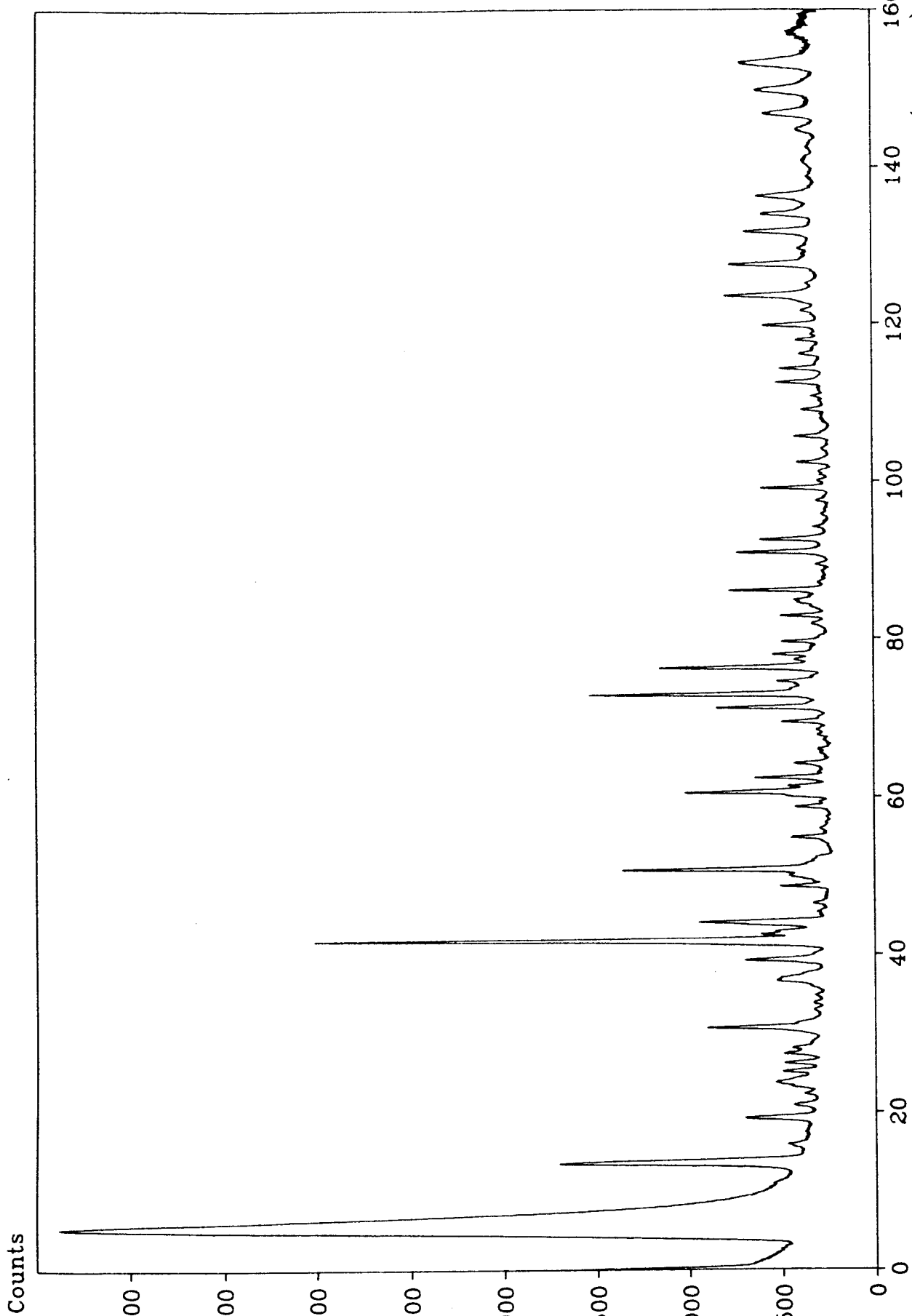

Figure 4.6 Powder neutron diffraction profile of $DSbO_3.xD_2O$ (dried sample). (λ=1.595 Å).

Table 4.4 Observed and Calculated Powder Neutron Diffraction Data for $DSbO_3.xH_2O$ (vacuum-dried sample)

(For clarity only one reflection is given for each observed peak)

h k l	*2θ(obs)*	*2θ(calc)*	*h k l*	*2θ(obs)*	*2θ(calc)*
2 2 0	13.64	13.68	10 8 6	72.93	72.94
3 1 1	15.96	16.05	12 8 0	74.60	74.62
4 0 0	19.31	19.38	10 10 4	76.30	76.30
3 3 1	20.96	21.14	11 8 6	77.33	77.33
4 2 1	22.41	22.23	12 4 4	78.00	77.96
4 2 2	23.88	23.79	14 6 0	79.60	79.61
4 3 0	24.33	24.29	11 11 1	81.93	81.86
3 3 3	25.20	25.25	12 10 2	82.93	82.88
4 3 2	26.29	26.19	10 10 8	86.13	86.13
4 4 0	27.46	27.53	10 10 9	89.47	89.57
5 3 0	28.25	28.39	12 12 0	91.00	90.99
6 2 0	30.84	30.85	14 8 6	92.57	92.61
6 3 1	33.08	33.14	12 12 4	94.22	94.23
4 4 4	33.94	33.88	16 6 6	99.15	99.12
5 5 1	34.91	34.95	12 10 10	102.40	102.41
6 4 2	36.74	36.68	12 12 8	104.13	104.08
7 2 2	37.10	37.02	14 10 8	105.75	105.75
8 0 0	39.34	39.31	14 12 8	109.10	109.14
6 5 3	41.24	41.19	16 8 8	110.88	110.86
6 6 0	41.80	41.80	14 14 0	112.60	112.60
5 5 5	42.58	42.71	20 0 0	114.35	114.37
6 6 2	42.99	43.00	14 14 4	116.20	116.16
8 4 0	44.15	44.18	16 12 4	117.97	117.97
6 6 4	46.51	46.46	18 8 6	119.80	119.82
8 4 4	48.65	48.65	12 12 12	121.70	121.70
8 6 2	50.78	50.77	14 12 10	123.65	123.63
10 4 2	54.85	54.84	14 14 8	127.63	127.61
8 6 6	58.73	58.71	16 12 8	129.68	129.68
12 0 0	60.60	60.58	20 8 4	134.02	134.02
12 2 2	62.45	62.43	16 14 6	136.38	136.31
12 4 0	64.25	64.24	16 15 4	138.80	139.01
10 8 2	66.05	66.02	15 13 11	144.80	144.92
12 4 4	67.78	67.78	18 14 0	146.80	146.72
9 7 7	68.45	68.44	16 16 4	149.80	149.80
12 6 2	69.47	69.52	14 14 12	153.25	153.18
8 8 8	71.25	71.24	16 16 12	157.07	157.02

λ=1.595 Å
a=18.982(1) Å

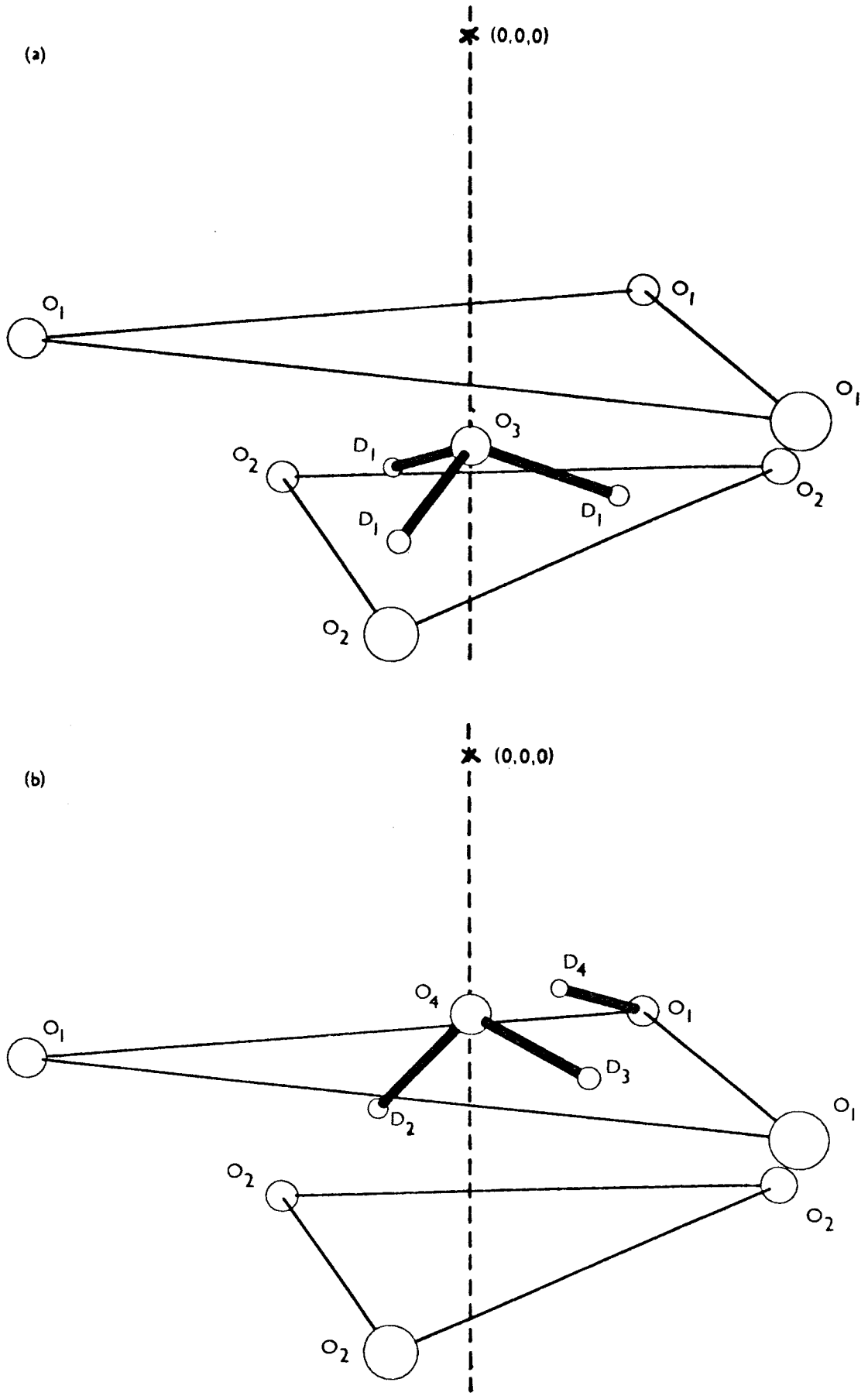

Figure 4.7 A portion of the structure of $DSbO_3.0.81D_2O$, viewed approximately perpendicularly to <111> and showing the positions of the (a) D_3O and (b) D_2O+OD species relative to the framework oxygens O(1) and O(2).

environment for the D_3O^+ ion, with the D(1)–O(2) distance of 1.56 Å indicating the presence of hydrogen bonding. The occupancies of the two oxygen sites O(3) and O(4) are in reasonable agreement with the single crystal work of Watelet et al., who found occupancies of 0.45 and 0.30 respectively for the O(3) and O(4) sites in $HSbO_3.0.75H_2O$. This work also showed that partial dehydration of the material resulted in preferential loss of water from the O(3) site. It is likely that the fully dehydrated material $DSbO_3$ would consist of a similar SbO_3 framework with deuteroxyl groups at O(1).

Bond length/ bond strength calculations following the work of Brown and Wu[7] suggest that O(1) is the preferred site of an OD group. According to the model a cation-oxygen bond distance, R, may be related to its bond valence, S, by the equation

$$S = (R/R_0)^{-N}$$

where R_0 and N are emprically derived parameters. For Sb(V) R_0 is 1.911 Å and N 6.0. In the case of O(2) the sum of the "valences" of the two inequivalent Sb–O bonds is 1.645, whereas two Sb–O(1) bonds contribute 1.586. The inference is that any protons bound to the framework would be more likely to be associated with O(1), especially considering the strong O(2)–D(1) hydrogen bonding. In fact if the relative occupancies of O(1) and D(4) and the bond distance between them are taken into account then the average "valence" of an O(1) atom becomes 1.96, close to the ideal value of 2.

Partial hydration of $HSbO_3$ would thus involve the occupancy of the O(4) site with the formation of a hydrogen bond similar to the arrangement found for example in $H_2Ta_2O_6.xH_2O$. However the relative positions of O(3) and O(4) suggest that as

the level of hydration is increased, the O(3) site would also increasingly be occupied in order to minimise the effect of oxygen-oxygen repulsion: the distance from O(4) to the next nearest O(3) site (obviously neighbouring O(3) and O(4) sites cannot be occupied) is 3.76 Å, compared with 3.49 Å between neighbouring O(4) sites. Occupation of O(3) is thus predicted to occur once there are more than four water molecules in the unit cell, which is in good agreement with the refined occupancy of O(4). This is accompanied by migration of protons to form a hydronium ion, strongly bound to the lattice. The presence of H_3O^+ in fully hydrated samples agrees with the NMR work on these materials[1].

At low levels of hydration there must exist a greater number of protons bound to the framework than in $DSbO_3.0.81D_2O$. On the basis of the arguments presented above this could be expected to result in a distortion of the framework to accommodate the longer Sb–O bonds, one possible effect of which might be the creation of a doubled cell parameter as observed for the vacuum-dried sample.

CHAPTER 5

QUASIELASTIC NEUTRON SCATTERING STUDY OF SOME PROTONIC MATERIALS

5.1 Introduction [1,2]

Neutron scattering can be either coherent or incoherent. Incoherent scattering is caused by random effects such as lattice defects or stochastic motion in solids and liquids whereas coherent scattering is a direct result of the periodicity of the structure. Coherent scattering subdivides into two further categories dependent on whether a transfer of energy takes place between the neutron and the scatterer: coherent elastic scattering corresponds to Bragg scattering and is discussed elsewhere in this work; coherent inelastic scattering occurs, for example, when a fundamental vibrational mode is excited during the scattering process. Indeed inelastic neutron scattering is widely used to study the vibrational spectra of solids.

The technique has two principle advantages over optical methods. First, the selection rules pertaining to infrared and Raman spectroscopy do not apply in the case of neutron scattering. Secondly, in addition to energy, momentum is also transferred during the scattering process. The momentum transfer is described in terms of the reduced wavevector **Q** as follows

$$h\mathbf{Q} = (mv - mv_0)$$

where m is the mass of the neutron and v and v_0 are the velocities of the scattered and incident neutrons respectively. **Q** is itself defined as the difference between the wavevectors of the incident and scattered neutrons

$$\mathbf{Q} = \mathbf{k}_0 - \mathbf{k}$$

Experimentally the momentum range of scattered neutrons is determined by scanning their angular distribution. For example in the case of elastic scattering the magnitude of the incident and scattered wavevectors is equal and therefore

$$Q = |\mathbf{Q}| = 2k_0 \sin\theta$$
$$= \frac{4\pi}{\lambda}\sin\theta$$

where λ is the neutron wavelength and θ is the scattering angle analogous to the Bragg angle 2θ.

Thus using a time-of-flight spectrometer, simultaneous energy spectra may be recorded over a range of scattering angles to give the full scattering law $S(\mathbf{Q},\omega)$ for the scattering system.

In the case of vibrational spectroscopy the availability of a range of Q enables for example phonon dispersion curves to be obtained whereas optical methods only give the energy of modes at Q=0. The neutron scattering spectrum of an ideal crystalline solid at a given Q consists of a strong elastic peak at $\Delta E=0$ corresponding to scattering from fixed nuclei in the sample and whose width is dependent solely on the instrumental resolution. Flanking this peak are others corresponding to inelastic scattering by phonons of energy $\Delta E=\hbar\omega$, with each peak on the energy loss side being "mirrored" by one on the energy gain side (assuming $\Delta E \ll kT$).

Quasielastic scattering is said to occur when the energy transfer is sufficiently small in magnitude that it is not observed as a discrete peak but instead as a broadening of the elastic peak. The energy transfers giving rise to quasielastic scattering are no greater than the order of 1 meV (in terms of optical spectroscopy 1 meV$\cong$8 cm^{-1}). Quasielastic scattering is in fact the result of random translations and rotations in the scatterer and is incoherent. Information about translational and rotational diffusion in

a system may therefore be obtained if the quasielastic part of the scattering is able to be deconvoluted from the elastic component.

Proton-containing materials lend themselves uniquely well to study by such neutron scattering techniques since ^1H has by far the largest neutron scattering cross-section (σ) of any nucleus and of this the dominant component is the incoherent ($\sigma_{tot}= 81.5\times10^{-28}\,m^2$, $\sigma_{inc}= 79.7\times10^{-28}\,m^2$) Amomg the first areas to be studied by quasielastic neutron scattering (QENS) was the behaviour of hydrogen in metals, discussed in a review of Springer[3]. Metals have the advantage that their structures are relatively simple and, for example, in the case of PdH_x, diffusional motion may be accurately represented by the Chudley-Elliot[4] model.

Studies of water-containing complex oxides present a higher order of complexity. Often more than one type of motion is present and studies may be carried out under different experimental conditions to obtain the maximum information. For instance using thermal neutrons with a relatively long wavelength of about 12 Å will result in high angular resolution but only allow a low range of Q (<1 $Å^{-1}$) to be studied, giving information on long-range diffusion, whereas higher values of Q (2 $Å^{-1}$-4 $Å^{-1}$) are needed to probe the microscopic detail of protonic motion. Similarly high energy resolution is not only obtained at the expense of neutron intensity but in addition the element of time probed is inversely proportional to this resolution. Time-of-flight instruments with energy resolutions in the range 10 μeV -200 μeV give information on events in the timescale 10^{-10} -10^{-12} s while higher resolutions allow access to longer time domains; for example 1 μeV, resolution obtainable on a spin-echo spectrometer, corresponds to the order of 10^{-9} s.

An early study using the technique was carried out by Roth and co-workers on $H_3O^+\beta''$-alumina[5]. The observed quasielastic broadening was fitted to a single

Lorentzian. It was not possible unambiguously to identify translational motion, since at low Q the halfwidth did increase as DQ^2 and at high temperature even decreased with Q. However a diffusion coefficient of $1.5\times10^{-13}\,m^2\,s^{-1}$ was estimated at room temperature. Recent work on hydrated inorganic materials using QENS include an investigation of $HUO_2PO_4.4H_2O$ (HUP) by Poinsignon, Fitch and Fender[6] using a range of instruments at the I.L.L., including the time-of-flight spectrometers IN5 and IN6 and the high energy-resolution spectrometer IN10. Three separate types of motion were identified: a rapid H_3O^+ rotation with a residence time of 4×10^{-12} s, a slower reorientation of H_2O with residence time 5.6×10^{-11} s and energy of $20\,kJ\,mol^{-1}$ and translational motion of protons. Work on the analogous compound $NaUO_2PO_4.4H_2O$ (NaUP)[7] also revealed a reorientation of H_2O (residence time 2×10^{-12} s) and a translational motion, involving all the protons and with residence time 2.2×10^{-9} s. Diffusion coefficients for both materials were of the order of $10^{-11}\,m^2\,s^{-1}$. Similarly the technique has been used by Pressman and Slade[8] to study the tungstophosphoric acid $H_3PW_{12}O_{40}.6H_2O$. Using the spectrometer IN13 at the I.L.L. (Q range 1.2 to $5.0\,Å^{-1}$, elastic peak resolution of the order of full width at half height (fwhm)=8 μeV), a twofold reorientation of H_2O groups was identified analogous to the H_2O motion in HUP and with an activation energy of $14\,kJ\,mol^{-1}$ and residence time of 6×10^{-13} s.

In this work a preliminary study has been made of protonic motion in the proton-conducting material $HSbO_3.xH_2O$ ("cubic" $KSbO_3$ structure), and in the defect pyrochlores $H_2OH_2Ta_2O_6$, NH_4TaWO_6 and $NH_4HTa_2O_6$. $H_2OHTaWO_6$ was prepared but not studied by QENS.

As described in chapter 4, cubic $HSbO_3.xH_2O$ has been studied by Watelet et al.[9], who carried out a structural study, and by Chowdhry and co-workers[10] who

measured the conductivity of the material, which was found to be of the order of $10^{-3}\,(\Omega cm)^{-1}$ at room temperature. The conductivity exhibited an Arrhenius-like temperature dependence below 350 K and the activation energy was found to be $38.1(\pm 0.4)\,kJ\,mol^{-1}$. These last workers also carried out a pulsed proton NMR study of the material which suggested that protonic motion at low temperatures is mainly due to an anisotropic reorientation of H_3O^+ whereas above room temperature all protons participate in exchange. An activation energy for this (short range) motion was calculated to be approximately $12\,kJ\,mol^{-1}$.

The defect pyrochlore-structured compounds have been studied by a number of workers, and due to the ease by which they may be ion-exchanged have aroused interest as possible proton-conducting materials.

The group of Raveau and co-workers first reported the synthesis of $Tl_2Ta_2O_6$[11] and $KTaWO_6$[12] and their acidic ion exchange to form $H_2OH_2Ta_2O_6$ and $H_2OHTaWO_6$, as well as the preparation of NH_4TaWO_6[13]. All these materials crystallise in the space group Fd3m. The structures of $H_2OH_2Ta_2O_6$ and $H_2OHTaWO_6$ have been determined respectively by Dickens and Weller[14] and by Groult and co-workers[15], both using powder neutron diffraction. In each case the water molecule was found to be located in the large pyrochlore cavity with the water oxygen on, or close to, the 8b site at the centre of the cavity. This contrasts with the monovalent cations which are believed to exist on 16d sites in the bottleneck between cavities[16]. The extra proton is attached to a framework oxygen. The water molecule is aligned such that its oxygen points towards the individual proton, with a hydrogen-bonding distance of 2.27 Å in $H_2OH_2Ta_2O_6$; distances of 2.32 Å were also found between water proton and framework oxygen in $H_2OHTaWO_6$.

Proton NMR studies of $H_2OHTaWO_6$ were carried out by Butler and Biefeld[17] in order to characterise the protonic motion in this material. They concluded that between 200 K and 300 K protonic motion is dominated by the reorientation of the water molecule and that significant translational motion was in evidence above 300 K. It was determined that this motion was solely due to individual protons and that no translation of the water molecule occurs (but presumably only up to 360 K when the material begins to dehydrate). An activation energy for the proton motion of approximately 24 kJ mol^{-1} was estimated from relaxation data. The use of an incorrect structural model detracted from their analysis of the results, however similar work by Dickens and Weller[14] on $(H_2O)_{0.42}H_2Ta_2O_6$ gave an activation energy of 20 kJ mol^{-1} for proton motion and an estimated diffusion coefficient of 10^{-13} m^2 s^{-1}.

A powder neutron diffraction study by Kuntz and co-workers[18] of NH_4TaWO_6 found that NH_4^+ is also situated at the centre of the pyrochlore cavity. Up to 523 K there was no evidence for translational motion of NH_4^+ and they suggested that the observed protonic conductivity of the material (for which they cited a dissertation by Brunner) was due to a Grotthus-type mechanism. The minimum hopping distance between hydrogens of neighbouring ammonium ions is 2.28 Å at 300 K. NMR work by Butler and Biefeld[19], conducted between room temperature and 580 K, also suggested that only protons participate in translational motion. They estimated an activation energy of *ca.* 25 kJ mol^{-1} and attempt frequency of 1×10^{10} s^{-1} for the process. It is also worth noting that this compound is thermally stable up to 600 K whereas the hydrated pyrochlores begin to lose water at about 360 K.

In these compounds the types of protonic motion which thus would be expected to occur below the temperature range of decomposition fall into two categories. First long-range diffusion of protons is expected, most probably involving a hopping

mechanism from site to site and without translation of NH_4^+ or H_3O^+. Secondly localised motions will occur involving rotation of the protonic cavity species, e.g. for H_2O a two-fold reorientation or "flipping" about the C_{2v} axis. The aim of the present work was an initial characterisation of protonic motion in the materials. It was hoped first to identify any temperature-dependent broadening of the elastic peak and then, if possible, fit the data to a simple Q-dependent diffusional model. The resolution of IN6 enables processes to be observed on a relatively short timescale of the order of 10^{-11} to 10^{-13} s.

5.2 Synthesis and Characterisation

Cubic $HSbO_3.xH_2O$: Synthesis

Cubic $HSbO_3.xH_2O$ was prepared as described in chapter 4 by ion exchange of cubic $KSbO_3$, itself prepared by heating a mixture of $KSb(OH)_6$ and KF. The ion exchange was carried out on this occasion using 3M HNO_3 (May and Baker, Lab. reag.). 400 cm^3 of the aqueous acid was used for approximately 6 g of solid and the mixture stirred in a conical flask for 3 days at 50 °C. The liquid was then filtered off, replaced with fresh acid and the reaction allowed to continue for a further 48 h. After this time the solid was again filtered off, washed thouroughly with distilled water and placed in a desiccator over $CaCl_2$. At the I.L.L. the compound was further dried in air at 70 °C for several hours to remove any remaining surface water.

Cubic $HSbO_3.xH_2O$: Characterisation

$HSbO_3.xH_2O$ and the parent compound $KSbO_3$ were characterised by powder x-ray diffraction and infrared spectroscopy. The infrared spectra were closely similar to those discussed in chapter 4, as was the x-ray powder pattern of $KSbO_3$: a cubic cell parameter of 9.615 Å was determined. The diffraction pattern of $HSbO_3.xH_2O$

could be entirely indexed on the basis of a cubic unit cell, and in the space group Im3. The cell parameter was 9.5255(5) Å and the observed and calculated peak positions are given in table 5.1. In addition the extent of ion exchange was determined by flame photometry of the reaction solution, as described previously. The amount of K^+ found in the solution was equivalent to 96(±4)% of the potassium content of the parent compound, assumed to be a pure phase of $KSbO_3$.

No direct method of determining the water content of the exchanged material was available. It was therefore arbitarily assigned the composition $HSbO_3.0.75H_2O$. There is good deal of agreement among previous work, including the study described here in chapter 4, that for samples prepared under ambient conditions using dilute acid, and not dried under extreme conditions, the amount of water taken up is between 0.7 and 0.8 molecules per SbO_3 unit[9,10].

Pyrochlores : Synthesis

$H_2OH_2Ta_2O_6$ was prepared by ion exchange of $Tl_2Ta_2O_6$. $Tl_2Ta_2O_6$ was synthesised according to the method of Deschanvres et al.[11]: Tl_2CO_3 (fluka, >99%) and Ta_2O_5 (BDH, >99.9%) were intimately ground together in equimolar proportions and then heated in an alumina boat at 600 °C for 16 h under a blanket of dry nitrogen. The nitrogen was necessary to prevent the oxidation of Tl^+ to Tl^{3+} which will not exchange with acids. The mixture was heated up to the reaction temperature at the slow rate of 2 °C min^{-1} in order to minimise crepitation of the sample due to the evolution of CO_2, and at the completion of the reaction cooled at a similar rate to ensure maximum crystallinity of the sample. The quantity of reactants was chosen so as to give about 12 g of product.

The ion exchange was effected by reaction of the brown $Tl_2Ta_2O_6$ with 3M

Table 5.1 Observed and Calculated Powder Diffraction Data for $HSbO_3.xH_2O$

h k l	2θ*(obs)*	2θ*(calc)*
1 1 0	13.14	13.14
2 0 0	18.64	18.62
2 1 1	22.84	22.85
3 1 0/1 3 0	29.62	29.63
2 2 2	32.54	32.54
3 2 1/2 3 1	35.22	35.22
4 0 0	37.76	37.75
4 1 1/3 3 0	40.12	40.13
4 2 0/2 4 0	42.41	42.40
3 3 2	44.65	44.58
4 2 2	46.73	46.67
5 1 0/1 5 0/4 3 1/3 4 1	48.74	48.70
5 2 1/2 5 1	52.60	52.58
5 3 0/3 5 0/4 3 3	56.29	56.27
6 0 0/4 2 2	58.06	58.05
6 1 1/5 3 2/3 5 2	59.80	59.80
6 2 0/2 6 0	61.52	61.52
5 4 1/4 5 1	63.19	63.21
6 3 1/3 6 1	66.54	66.52
4 4 4	68.08	68.15
7 1 0/1 7 0/5 5 0/5 4 3/4 5 3	69.79	69.75
6 4 0/4 6 0	71.40	71.34
7 2 1/2 7 1/6 3 3/5 5 2	72.94	72.92
7 3 0/3 7 0	76.04	76.03
7 3 2/3 7 2/6 5 1/5 6 1	79.10	79.10
8 0 0	80.66	80.62
8 1 1/7 4 1/4 7 1/5 4 4	82.09	82.14
6 5 3/5 6 3	85.20	85.15
6 6 0/8 2 2	86.65	86.66
7 5 2/5 7 2	88.13	88.16
6 6 2	89.59	89.66
9 1 0/1 9 0/8 3 3	94.16	94.16
8 4 2/4 8 2	95.66	95.63
9 2 1/2 9 1/7 6 1/6 7 1/6 5 5	97.19	97.17
6 6 4	98.68	98.68
9 3 0/3 9 0/8 5 1/5 8 1/7 5 4/5 7 4	100.18	100.20
9 3 2/3 9 2/7 6 3/6 7 3	103.23	103.26
8 4 4	104.84	104.81
9 4 1/4 9 1/8 5 3/5 8 3/7 7 0	106.42	106.36
8 6 0/6 8 0/10 0 0	108.10	107.93
9 4 3/4 9 3/9 5 0/5 9 0	112.73	112.73
6 6 6/10 2 2	114.29	114.36
9 5 2/5 9 2/10 3 1/3 10 1/7 6 5/6 7 5	116.02	116.02

λ=1.5406 Å
a=9.5255(5) Å

HNO_3 (May and Baker). Approximately $400\,cm^3$ was used for 12 g of $Tl_2Ta_2O_6$. Although its colour changed from brown to white within a few minutes, the mixture was stirred for 3 days with the acid being filtered off and changed every 24 h. At the completion of the reaction the white product was filtered off, washed with distilled water and placed in a desiccator over $CaCl_2$. Prior to the final washing a small portion of fresh acid was washed through the sample under suction and tested with KI solution to ensure that there was no Tl^+ remaining in the sample (Tl^+ gives a yellow precipitate of TlI).

$NH_4HTa_2O_6$ was prepared by an adaptation of the method of Hervieu et al.[13] $H_2OHTa_2O_6$, obtained as above, was stirred in a 3M solution of NH_4Cl (Biolab, >99%) in 0.880 ammonia (BDH, Lab. reag.). About $400\,cm^3$ was used for 10 g of the solid. After 24 h the solution was filtered off and replaced, and the reaction continued for a further 24 h. At the completion of the reaction the product was filtered off under suction, washed first with 0.880 ammmonia, then sparingly with water and finally further pumped on under the pressure of a water pump for several hours until it had the appearance of a dry white powder. This had the effect of causing any ammonia which may have been adhering to the surface of the particles to evaporate. The product was stored in a sealed bottle in a desiccator.

$H_2OHTaWO_6$ was prepared by ion exchange of $KTaWO_6$. $KTaWO_6$ was prepared by the reaction of K_2CO_3 (BDH, >99.9%), Ta_2O_5 and WO_3 (Fluka, 99.9%). The reactants were intimately ground together in the molar ratio of 1:1:2 respectively and heated in an alumina boat at 800 °C for 48 h. As for $Tl_2Ta_2O_6$, and for the same reasons, the mixture was both heated and cooled at a slow rate. About 12 g of white crystalline product was produced in a single preparation.

To prepare $H_2OHTaWO_6$, The $KTaWO_6$ was stirred in 3M HNO_3 for 48 h. About 400 cm^3 of the acid, which was changed after 24 h, was used for 12 g of solid. At the end of this period, the white product was filtered off, washed thoroughly with distilled water under suction and stored in a desiccator.

NH_4TaWO_6 was prepared in similar manner to $NH_4HTa_2O_6$, described above. $H_2OHTaWO_6$ was stirred in a 3M solution of NH_4Cl in 0.880 ammonia for 48 h with the solution (about 400 cm^3 for 10 g of solid) being changed once after 24 h. The white product was then isolated, washed and dried as for $NH_4HTa_2O_6$.

Pyrochlores : Characterisation

Each of the unexchanged and exchanged samples was characterised by powder x-ray diffraction and infrared spectroscopy. In addition, after each of the acid exchanges, the amount of exchanged ion in the supernatant was determined; in the case of Tl^+ by gravimetry and for K^+ by flame photometry. The ammonium content of the ammonium-containing materials was determined titrimetrically. At the time that this work was carried out, thermogravimetric analysis was not available as a characterisation technique.

Powder X-Ray Diffraction

For each of the six pyrochlore materials synthesised, including the unexchanged oxides, powder x-ray diffraction showed pure phases which could be indexed in the space group Fd3m. In addition, all the lattice parameters obtained were in very close agreement with previously reported values, where available. These results are given in table 5.2. For the individual phases, observed and calculated peak positions are given in tables 5.3 to 5.8.

Table 5.2 Observed Cubic Lattice Parameters for Pyrochlore-Structured Materials

	a/Å(this work)	*a/Å(literature)*	*reference*
$Tl_2Ta_2O_6$	10.631(4)	10.61	11
$H_2OH_2Ta_2O_6$	10.577(4)	10.580(5)	13
$NH_4HTa_2O_6$	10.608(3)	-	-
$KTaWO_6$	10.484(2)	10.469(2)	12
$H_2OHTaWO_6$	10.402(1)	10.401(7)	17
NH_4TaWO_6	10.361(4)	10.362(6)	19

Table 5.3 Observed and Calculated Powder Diffraction Data for $Tl_2Ta_2O_6$

h k l	*2θ(obs)*	*2θ(calc)*
2 2 2	29.06	29.07
4 0 0	33.73	33.70
3 3 1	36.85	36.82
4 2 2	41.57	41.58
4 4 0	48.40	48.39
5 3 1/3 3 3	50.76	50.77
4 4 2	51.54	51.54
6 2 2	57.45	57.45
4 4 4	60.26	60.26
8 0 0	70.85	70.85

λ=1.5406 Å

a=10.631(4) Å

Table 5.4 Observed and Calculated Powder Diffraction Data for $H_2OH_2Ta_2O_6$

h k l	2θ*(obs)*	2θ*(calc)*
1 1 1	14.50	14.49
3 1 1	27.95	27.95
2 2 2	29.22	29.22
4 0 0	33.88	33.87
3 3 1	37.02	37.02
5 1 1/3 3 3	44.49	44.47
4 4 0	48.67	48.66
5 3 1	51.03	51.04
5 3 3	57.03	57.05
6 2 2	57.78	57.78
4 4 4	60.59	60.60
5 5 1/7 1 1	62.66	62.67
5 5 3/7 3 1	68.02	68.03
8 0 0	71.27	71.27

λ=1.5406 Å

a=10.577(4) Å

Table 5.5 Observed and Calculated Powder Diffraction Data for $NH_4HTa_2O_6$

h k l	2θ*(obs)*	2θ*(calc)*
1 1 1	14.44	14.45
3 1 1	27.85	27.87
2 2 2	29.12	29.14
4 0 0	33.79	33.77
3 3 1	36.89	36.90
4 2 2	41.67	41.68
5 1 1/3 3 3	44.34	44.33
4 4 0	48.52	48.50
5 3 1	50.88	50.88
5 3 3	56.88	56.87
6 2 2	57.60	57.59
4 4 4	60.41	60.41
5 5 1/7 1 1	62.48	62.47
5 5 3/7 3 1	67.80	67.80
8 0 0	71.01	71.02

λ=1.5406 Å

a=10.608(3) Å

Table 5.6 Observed and Calculated Powder Diffraction Data for $KTaWO_6$

h k l	*2θ(obs)*	*2θ(calc)*
1 1 1	14.61	14.62
3 1 1	28.20	28.21
2 2 2	29.48	29.49
4 0 0	34.18	34.18
3 3 1	37.37	37.36
4 2 2	42.19	42.20
5 1 1/3 3 3	44.89	44.89
4 4 0	49.10	49.12
5 3 1	51.54	51.53
5 3 3	57.61	57.61
6 2 2	58.33	58.34
4 4 4	61.20	61.20
5 5 1/7 1 1	63.30	63.30
5 5 3/7 3 1	68.73	68.72
8 0 0	71.99	72.00
7 3 3	73.95	73.95

λ=1.5406 Å

a=10.484(2) Å

Table 5.7 Observed and Calculated Powder Diffraction Data for $H_2OHTaWO_6$

h k l	*2θ(obs)*	*2θ(calc)*
1 1 1	14.74	14.74
3 1 1	28.44	28.44
2 2 2	29.73	29.73
4 0 0	34.46	34.46
3 3 1	37.66	37.66
4 2 2	42.54	42.54
5 1 1/3 3 3	45.27	45.26
4 4 0	49.53	49.53
5 3 1	51.97	51.97
5 3 3	58.10	58.10
6 2 2	58.84	58.84
4 4 4	61.73	61.73
5 5 1/7 1 1	63.85	63.85
5 5 3/7 3 1	69.33	69.33
8 0 0	72.65	72.66
7 3 3	74.62	74.62
7 5 1/5 5 5	79.78	79.78

λ=1.5406 Å

a=10.402(1) Å

Table 5.8 Observed and Calculated Powder Diffraction Data for NH_4TaWO_6

h k l	2θ*(obs)*	2θ*(calc)*
1 1 1	14.79	14.80
3 1 1	28.54	28.55
2 2 2	29.84	29.85
4 0 0	34.63	34.60
3 3 1	37.82	37.82
5 1 1/3 3 3	45.45	45.45
4 4 0	49.75	49.74
5 3 1	52.18	52.18
5 3 3	58.36	58.35
6 2 2	59.08	59.09
4 4 4	61.99	62.00
5 5 1/7 1 1	64.11	64.13
5 5 3/7 3 1	69.62	69.65

λ=1.5406 Å

a=10.361(4) Å

Infrared Spectroscopy

Infrared absorption spectra were recorded of the six materials as CsI discs. The spectra for $Tl_2Ta_2O_6$ and its derivatives are shown in figure 5.1. It can be seen that the spectrum of $Tl_2Ta_2O_6$ is characterised by four broad bands centred at 1650, 1400, 570 and 350 cm^{-1} with weaker features at 1170 and 830 cm^{-1}. The broad feature at *ca.* 3200 cm^{-1} and the 1650 cm^{-1} band may be due to some adsorption of water during preparation of the finely powdered sample.

The spectrum of $H_2OH_2Ta_2O_6$ retains a number of the features of the parent compound, although somewhat altered in postion and relative intensity; in particular a strong band is observed at 1060 cm^{-1}. However the main features of interest are sharp bands at 3608 and 1605 cm^{-1}, corresponding respectively to the stretching mode of the (non hydrogen-bonded) framework O–H group and the symmetric bend, ν_2, of the water molecule at the centre of the pyrochlore cavity. The broad band centred at *ca.* 3260 cm^{-1}, with a shoulder on the high frequency side, is due to the O–H stretching modes of the H_2O molecule with the breadth of the absorption indicative of the hydrogen bonding believed to exist between H_2O and the framework-bound proton.

For $NH_4HTa_2O_6$ the framework absorptions are largely unchanged from the spectrum of $H_2OTa_2O_6$, with the exception of the band now at 1156 cm^{-1}. Strong bands due to the NH_4^+ group are observed at 1442 cm^{-1} (asymmetric bend, ν_4) and in the N–H stretching region, where a broad band has three features resolved at 3160, 3030 and 2850 cm^{-1}. According to the model of Kuntz et al. for NH_4TaWO_6, the NH_4^+ species is situated on a site of tetrahedral symmetry, with each hydrogen aligned towards equivalent framework oxygens. Therefore we would expect only one N–H stretching mode, the asymmetric stretch ν_3, in the infrared spectrum. However

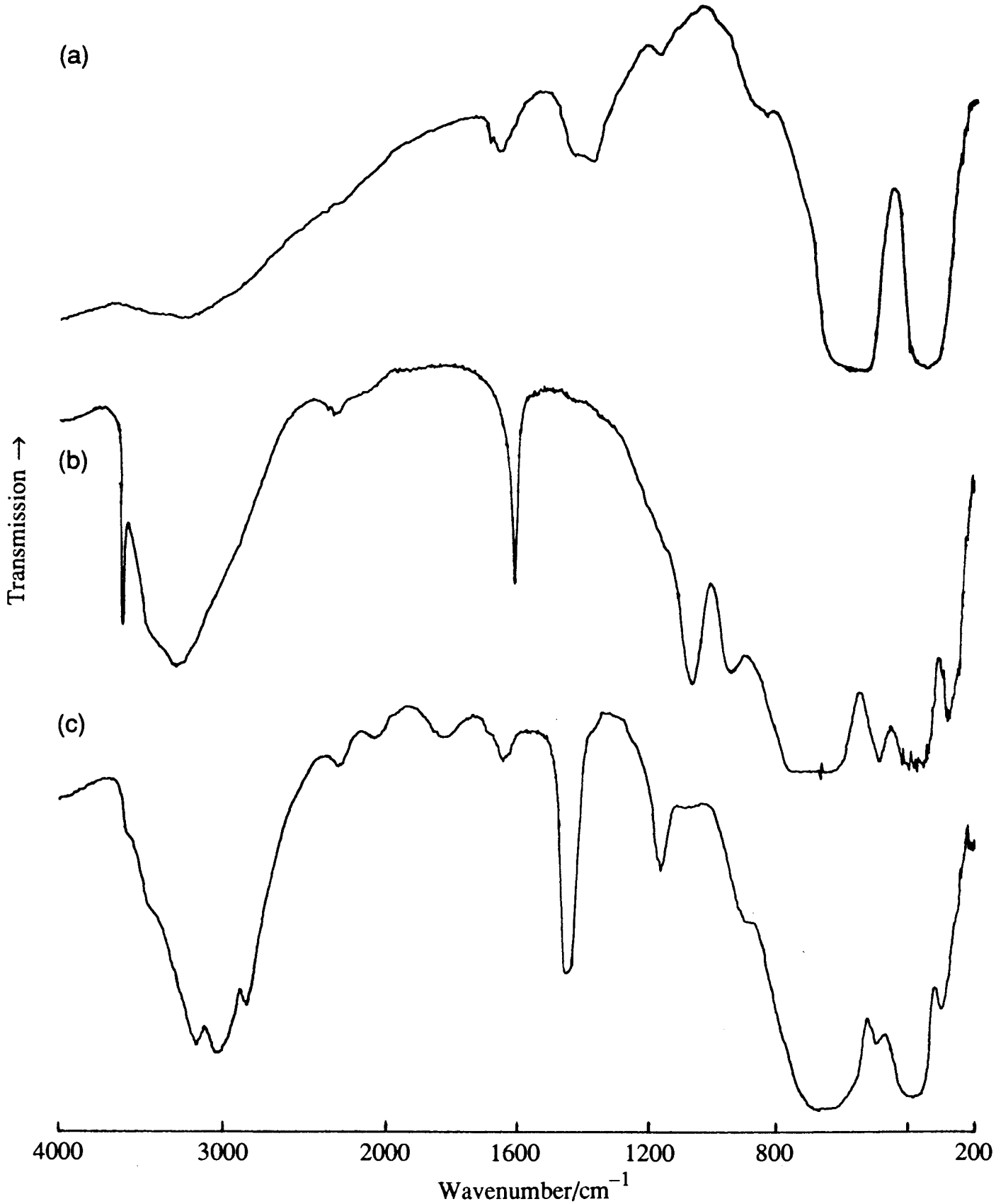

Figure 5.1 Infrared spectra of (a) $Tl_2Ta_2O_6$, (b) $H_2OH_2Ta_2O_6$ and (c) $NH_4HTa_2O_6$, recorded as pressed CsI discs.

thermal disorder of the NH_4^+ group will result in a lifting of the three-fold degeneracy of this mode, in addition to making the symmetric stretch, ν_1, infrared as well as Raman active, accounting for the multiplet observed here. The broadness of the absorption in this region may be due to hydrogen bonding between NH_4^+ and the framework oxygens.

The spectrum of $KTaWO_6$, shown together with those of its derivatives in figure 5.2, is less well resolved than that of $Tl_2Ta_2O_6$. It displays broad features at *ca.* 390 and *ca.* 650 cm^{-1} as well as a weak band at 1350 cm^{-1}, and two absorptions at 1630 and *ca.* 3450 cm^{-1} which may be due to surface-adsorbed water.

$H_2OHTaWO_6$ shows a stronger band at 1612 cm^{-1} due to the bending mode of water in the pyrochlore cavity. There is a "hump" at *ca.* 3550 cm^{-1} corresponding to the O–H stretching region, but no evidence of a sharp framework O–H stretch, as observed for $H_2OH_2Ta_2O_6$. This is accounted for by the fact that in this material every framework-bound proton is involved in hydrogen bonding with the cavity water molecule, whereas in $H_2OH_2Ta_2O_6$ only half are so involved.

For NH_4TaWO_6 the features of $KTaWO_6$ are preserved in the spectrum. In addition, a strong band arising from the asymmetric bend of NH_4^+ is observed at 1420 cm^{-1}, and there is absorption in the N–H stretching region between 2700 and 3400 cm^{-1} although the multiplet is poorly resolved.

Analysis

After the acid exchange of $KTaWO_6$, the reactant solution was analysed for K^+ by flame photometry, The approximately 1500 cm^3 of solution was diluted so that its K^+ content fell between 0 and 100 ppm, and the instrument calibrated with standard solutions containing 0, 25, 50, 75 and 100 ppm K^+. The measured amount of

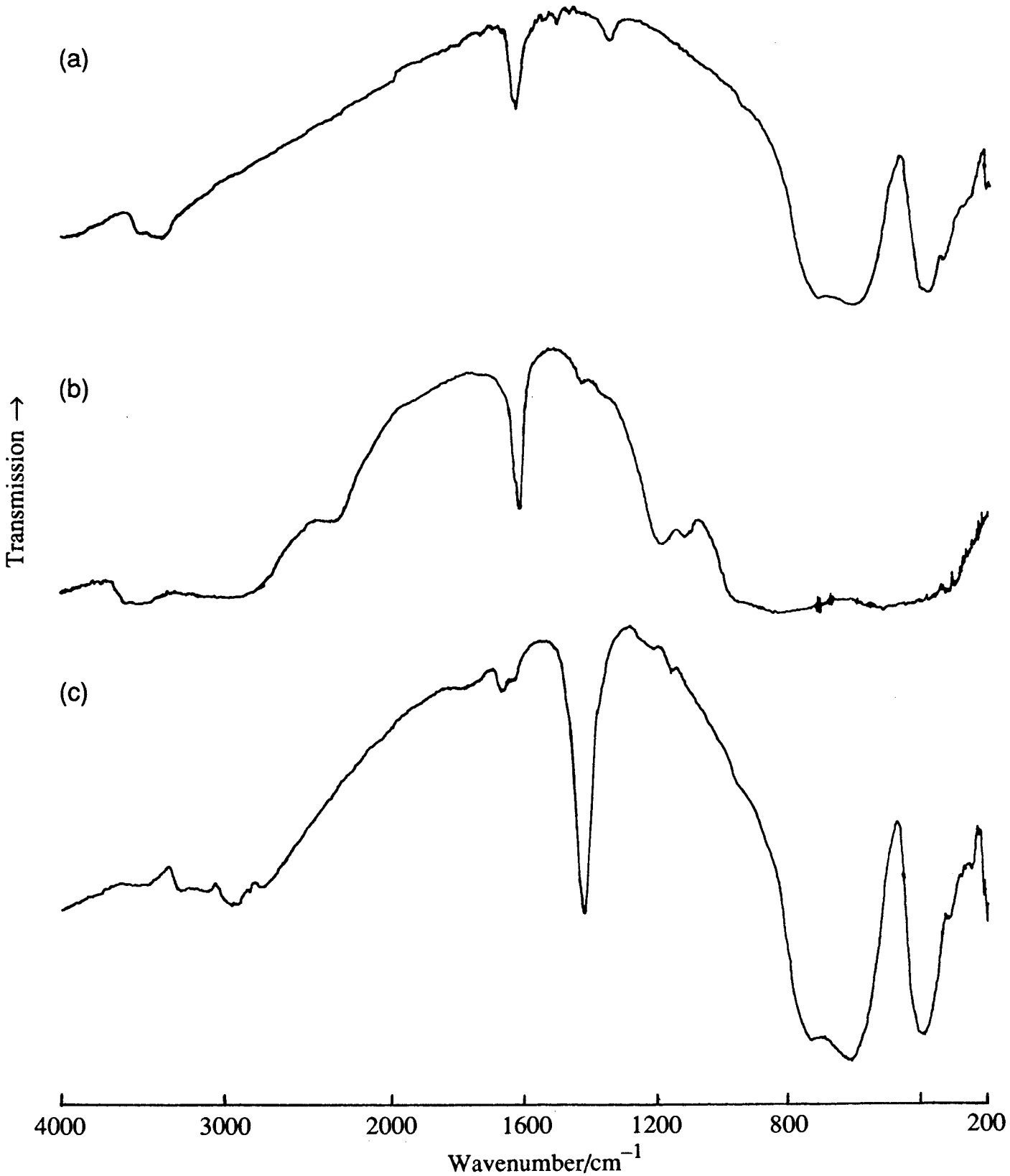

Figure 5.2 Infrared spectra of (a) $KTaWO_6$, (b) $H_2OHTaWO_6$ and (c) NH_4TaWO_6, recorded as pressed CsI discs.

exchanged K^+ represented 95(±6)% of the potassium content of the starting material, assumed for this purpose to be a pure phase of $KTaWO_6$.

For $Tl_2Ta_2O_6$, the amount of Tl^+ which had entered into solution during the reaction with HNO_3 was determined gravimetrically by precipitation as Tl_2CrO_4, using the method described by Vogel[20]: 50.00 cm^3 of the acid solution, containing about 0.15 g Tl^+, was diluted by the addition of 50 cm^3 of 1.5M ammonia, such that it had a pH of 9. The solution was then heated in a beaker to 80 °C and approximately 20 cm^3 of a 10% solution of K_2CrO_4 (fluka, purum) added slowly with stirring. The solution was then allowed to cool to room temperature and left standing for 24 h. After this period the yellow precipitate of Tl_2CrO_4 was filtered through a sintered glass crucible, which had previously been washed and dried to constant weight, washed with 1% K_4CrO_4 solution and then sparingly with 50% ethanol. The procedure was carried out in duplicate and the crucibles dried at 120 °C to constant weight. The amount of Tl^+ determined in this way corresponded to 98(±4)% of the theoretical value, assuming complete exchange and that the starting material was a pure phase of $Tl_2Ta_2O_6$.

The amount of ammonia in the ammonium-exchanged samples was determined titrimetrically using the Kjeldahl method, described in Vogel[20]. About 0.8 g of $NH_4HTa_2O_6$ was "back exchanged" by stirring in 200 cm^3 of HNO_3 solution for 24 h, in a sealed flask. The solid was then filtered off and washed thoroughly with distilled water. The ammonia-containing solution was then made up to a volume of 410.0 cm^3 and a 200.0 cm^3 aliquot of this transferred to a round-bottomed flask.

The remainder of the pyrex apparatus comprised a separating funnel, containing a 10M solution of NaOH (BDH), which was connected into the top of the flask such that a portion of the NaOH solution could be introduced without opening the system

to air. The funnel was connected to the flask by means of a T-piece, of which the side arm led, via a spray trap, to a condenser. The end of the condenser dipped into a receiver containing a solution of 20.00 cm^3 0.100M HCl (East Anglia Chemicals, AnalaR), made up to 150 cm^3.

100 cm^3 of the 10M NaOH was let into the flask and the mixture then boiled for 45 min using an electric isomantle. It was found that a gentle flow of dry nitrogen through the apparatus (using a three-necked flask with one side neck stoppered and N_2 introduced through the other) aided the flow of liberated ammonia through to the condenser. After the apparatus had cooled, the contents of the condenser and other glassware "downstream" from the spray trap (which prevented any of the alkaline reaction mixture splashing over into the condenser) was washed into the receiver. The contents of the receiver were then titrated against a 0.0996M solution of NaOH (BDH, AnalaR), previously standardised with the AnalaR HCl, using methyl red as indicator. The amount of ammonia liberated in the reaction was thus obtained by subtracting the amount of HCl determined from that which had originally been in the receiver. The procedure was carried out in duplicate for both ammonium-containing compounds.

A trial of the method using 0.5 g NH_4Cl gave a result corresponding to 96.5(±0.4)% of the actual ammonia content of the reaction solution. However for $NH_4HTa_2O_6$ and NH_4TaWO_6 the figures were 79(±5)% and 82(±3)% respectively, assuming that the materials had those exact stoichiometries. The large errors are due to the fact that for neither compound did the duplicate determinations agree with the first. It is surmised that in each case some ammonia was lost to the atmosphere during the reaction and therefore that the true ammonia content of the materials was higher than determined here.

Composition of the Exchanged Materials

Despite the result of the ammonia determination given above, and although no direct measurement of the composition of the exchanged pyrochlores was made, they were all assumed to be completely stoichiometric i.e. one mole of $(Ta/W)_2O_6$ framework always contains one mole of H_2O or NH_3. There are two observations to justify this. First, the cell parameters of the exchanged materials are identical, within calculated errors, to previously reported values. Secondly, previous workers have shown that stoichiometric exchange occurs with relative ease in these compounds, and therefore it is reasonable to assume that the same was achieved in this work

5.3 Experimental: Neutron Scattering

Inelastic neutron scattering spectra of the five samples were recorded on the spectrometer IN6 at the I.L.L., Grenoble, described in chapter 2. Each sample was contained in a thin-walled disc-shaped aluminium can such that it formed a slab of thickness 1 mm and diameter approximately 65 mm. The angle between the sample and the incident neutron beam was 135°, and it was found that the proportion of the incident beam scattered by each sample was approximately 10%. Initially spectra of all samples were recorded using a wavelength of 5.1 Å, giving an elastic energy resolution (fwhm) of the order of 70 μeV, at a range of temperatures between 80 and 400 K. Temperature was able to be controlled to ±1 K by means of a liquid nitrogen cryostat with a thermostatted tip heater. The data acquisition time at a given temperature was typically 50 min. Spectra were also recorded under the same conditions of an empty aluminium can over a similar range of temperatures and of a sheet of vanadium of the same dimensions as the sample slabs, at room temperature.

In order to improve counting statistics and to reduce the amount of collected

data to manageable proportions the detectors at 5.1 Å were grouped into 37 blocks covering an elastic Q range $0.255 \leq Q_{el} \leq 2.054$ Å^{-1}, thus giving 37 time-of-flight spectra over the approximate energy range $-2 < \Delta E < 700$ meV.

$HSbO_3.0.75H_2O$ was also studied at 5.9 Å at the temperatures 300, 350 and 400 K. Again spectra were recorded of an empty aluminium can at these temperatures and of vanadium at 300 K. The detectors were grouped into 33 blocks in the range $0.192 \leq Q_{el} \leq 1.776$ Å^{-1}. The time-of-flight spectra covered a similar energy range as for 5.1 Å and the elastic energy resolution was found to be of the order of 40 μeV. Due to the lower flux of neutrons at this wavelength and the greater angular dispersion, data acquisition times were longer, typically 3.5 h.

For each material the total counts, irrespective of time-of-flight, were summed at each collection angle to ensure that no Bragg peaks were contributing to the scattering data.

For an initial inspection at each temperature the raw data were viewed graphically in the form of a time-of-flight spectrum summed over the lowest 11 collection angles. This was also able to be plotted using a Tektronix thermal plotter.

5.4 Correction and Fitting of Data

To obtain the scattering function $S(\mathbf{Q},\omega)$ from an experimental spectrum, a number of corrections must applied to the data and they must be put on a scale of absolute cross-section by comparison with a sample of accurately-known cross-section and whose spectrum was recorded under the same experimental conditions. The usual material employed for this purpose is vanadium which scatters almost entirely incoherently ($\sigma_{inc} = 4.79 \times 10^{-28}$ m^2, $\sigma_{coh} = 0.019 \times 10^{-28}$ m^2 at 293 K), giving an isotropic distribution. Vanadium is also used for determining the instrumental

resolution function. These procedures were carried out using the programs PRIME and CROSSX running on a DEC-10 computer at the I.L.L.

First the vanadium data were used to calibrate the spectra, and to determine the position and shape of the elastic peak. At this stage the sample time-of-flight spectra were truncated such that they covered the range $-2<\Delta E<7$ meV, and for each spectrum a flat background and also the appropriate empty can data were subtracted.

Next, corrections were applied for absorption: the scattering and absorption cross-sections for each sample were calculated assuming the compositions discussed previously. The ratio of total scattering to scattering and absorption, $\sigma_{tot}/(\sigma_{tot}+\sigma_{abs})$ was obtained and used in the calculation together with the measured transmission of the sample. The absorption of the aluminium can was also taken into account.

Multiple scattering was assumed to be isotropic, and no correction was made for it. The efficiency of the detectors at values other than that of the incident energy was represented by a simple exponential function.

The spectra thus corrected were then normalised by comparison with the vanadium data. The normalised cross-section of the sample at a given scattering angle and over the time-of-flight interval $\Delta\tau$, representing one channel, is given by

$$S = \frac{I(s)}{I_{el}(V)} \frac{1}{\Delta\tau} \frac{N_V \sigma_{tot}(V)}{N_s \sigma_{tot}(s)} \frac{\varepsilon_{\tau_0}}{\varepsilon_\tau}$$

where I(s) is the corrected intensity of scattering from the sample over $\Delta\tau$, $I_{el}(V)$ is the corrected integrated intensity of the vanadium elastic peak, N_s and N_V the number of scattering atoms per unit area of sample and vanadium respectively and ε_{τ_0} and ε_τ respectively the efficiency of the detectors at incident energy and at the energy represented by the time-of-flight τ. The ratio $N_V\sigma_{tot}(V)/N_s\sigma_{tot}(s)$ was calcluated by taking the mass and dimensions of the sample and its previously evaluated

scattering cross-section, together with the known density and cross-section of vanadium.

Corrected data were fitted to a theoretical model using the program WLI[21], running in a DEC-10 computer at the I.L.L. A simple diffusional model was chosen where the quasielastic part of the scattering was represented by a single Lorentzian component. The elastic scattering was represented by a δ-function whose intensity was distributed between the two time-of-flight channels closest to the determined peak position. The model scattering function at a given Q was thus

$$S(\mathbf{Q},\omega) = A_0\delta(\omega) + A_L \frac{1}{\pi} \frac{(\Gamma/2)}{(\Gamma/2)^2+(\omega-\omega_0)^2}$$

where A_0 and A_L are the respective integrated intensities of the δ-function and Lorentzian, Γ the width and $\hbar\omega_0$ the energy position of the Lorentzian. The parameters varied in the fitting were A_0, A_L and Γ. In practice ω_0 was not allowed to vary independently of the elastic peak position. In the program both components were convoluted with the instrumental resolution function, obtained from the vanadium spectra, and the difference between the model and experimental spectra minimised by a least squares method.

5.5 Results

$H_2OH_2Ta_2O_6$

Data were collected for $H_2OH_2Ta_2O_6$ at seven temperatures between 83 K and 370 K. No broadening of the elastic peak was observed over this range. This can be seen from figure 5.3 which shows the raw time-of-flight spectra, summed over the lowest 11 angles of collection, at 83 K and 370 K together with the difference of the two. It was decided following this result not to study $H_2OHTaWO_6$ but to use the available instrument time on the other materials.

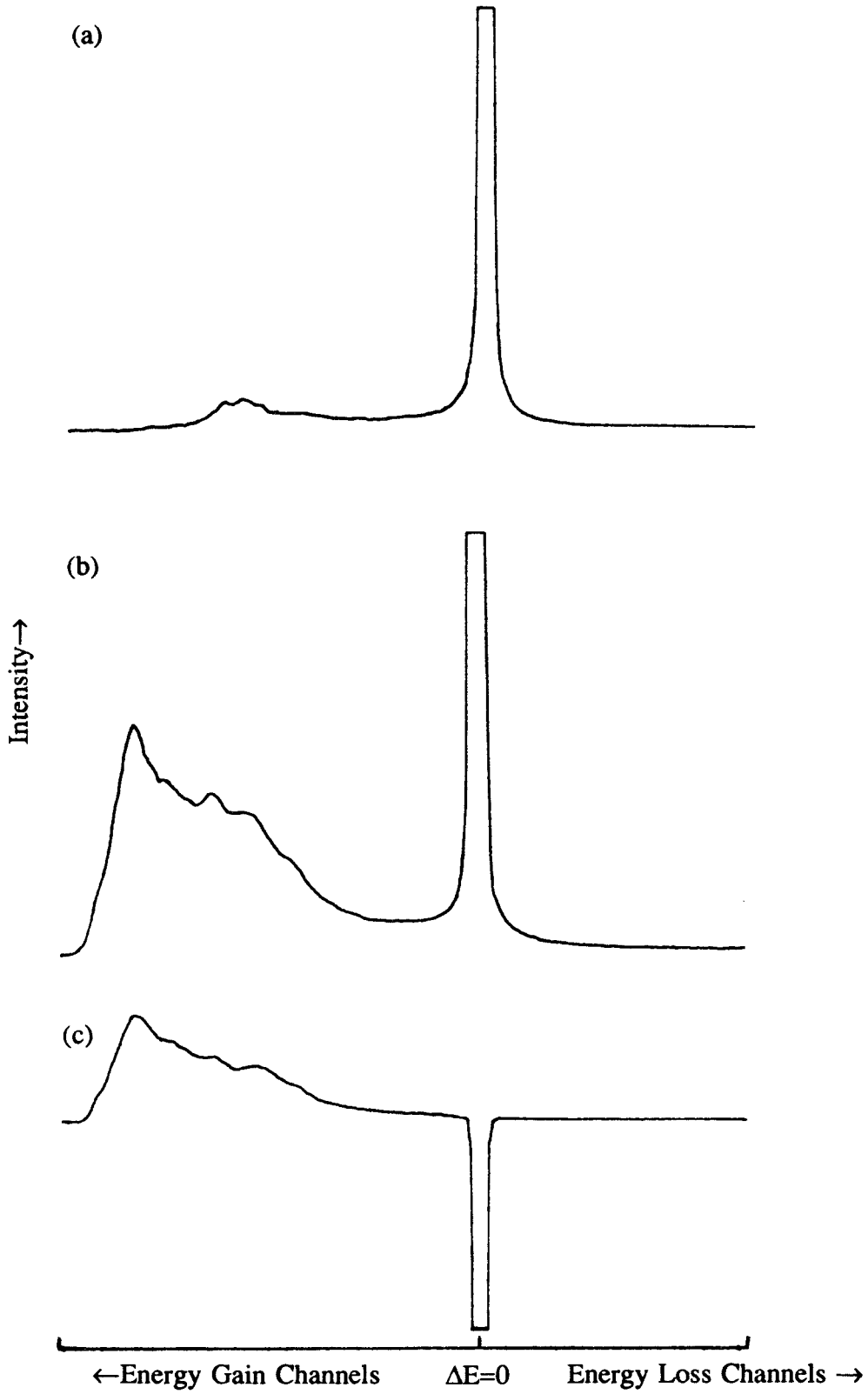

Figure 5.3 Raw inelastic neutron scattering data for $H_2OH_2Ta_2O_6$, showing summed time-of-flight spectra at (a) 83 K and (b) 370 K, with (c) (not on same intensity scale) the difference of the two.

$HSbO_3.0.75H_2O$

Spectra of this compound were similarly run using the wavelength 5.1 Å at five temperatures in the range 80 K to 370 K. In this case a substantial broadening of the elastic peak was observed which increased with temperature up to *ca.* 300 K. Again this is illustrated by a plot of the raw data showing the difference between the 320 K and 80 K spectra (figure 5.4). It was decided to study the material further at a higher resolution with neutrons of wavelength 5.9 Å. Spectra were collected at 300, 350 and 400 K since no broadening was observed between 320 K and 370 K at 5.1 Å. However in this case only a very low intensity broadening was observed between 300 K and 400 K (figure 5.5) which, given the quality of the data, was not analysed.

In order to determine whether the observed broadening was due to long-range diffusion or to localised rotations, the Q-dependence of the broadening was investigated by correcting the data and fitting the quasielastic part to a single Lorentzian component as described previously. Due to pressure of time at the I.L.L., the spectra were only fitted at the temperatures 80 K and 300 K (the latter using the 5.9 Å data) and over a selected range of Q values. At both temperatures a strong Q-dependence of the broadening was apparent. This is illustrated for the 80 K data in figure 5.6, where the fitted components are shown graphically for Q=0.309 and Q=1.954 $Å^{-1}$.

Plots of the halfwidth of the fitted Lorentzian against Q^2 are shown in figures 5.7 and 5.8 respectively for 80 K and 300 K. It can be seen that the broadenings fall in the order of magnitude of 1 meV, indicating a relatively fast diffusive process (1 meV corresponds directly to 4×10^{-12} s). The data do not vary linearly with Q^2, so to obtain an approximate Fick's law diffusion coefficient a linear least squares fit was carried out on data in the range $Q<1$ $Å^{-1}$, i.e. taking in each case four points, including one representing zero broadening at Q=0. The values obtained were

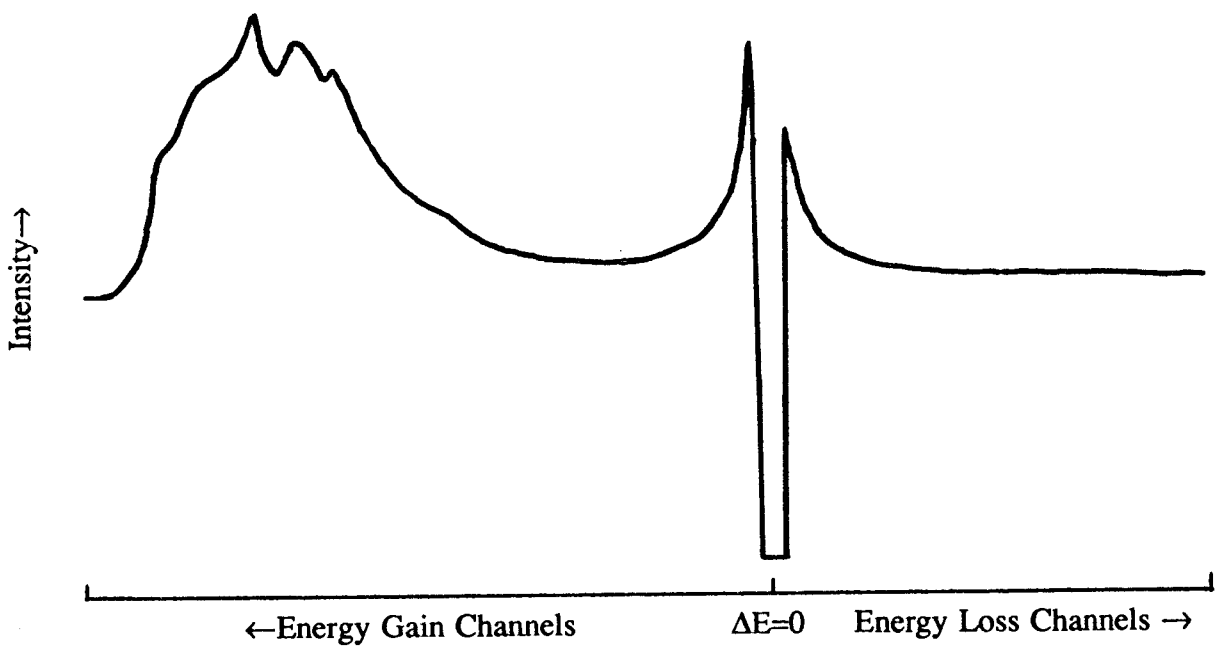

Figure 5.4 Raw inelastic neutron scattering data for $HSbO_3.0.75H_2O$: summed 320 K time-of-flight spectrum with 80 K spectrum subtracted.

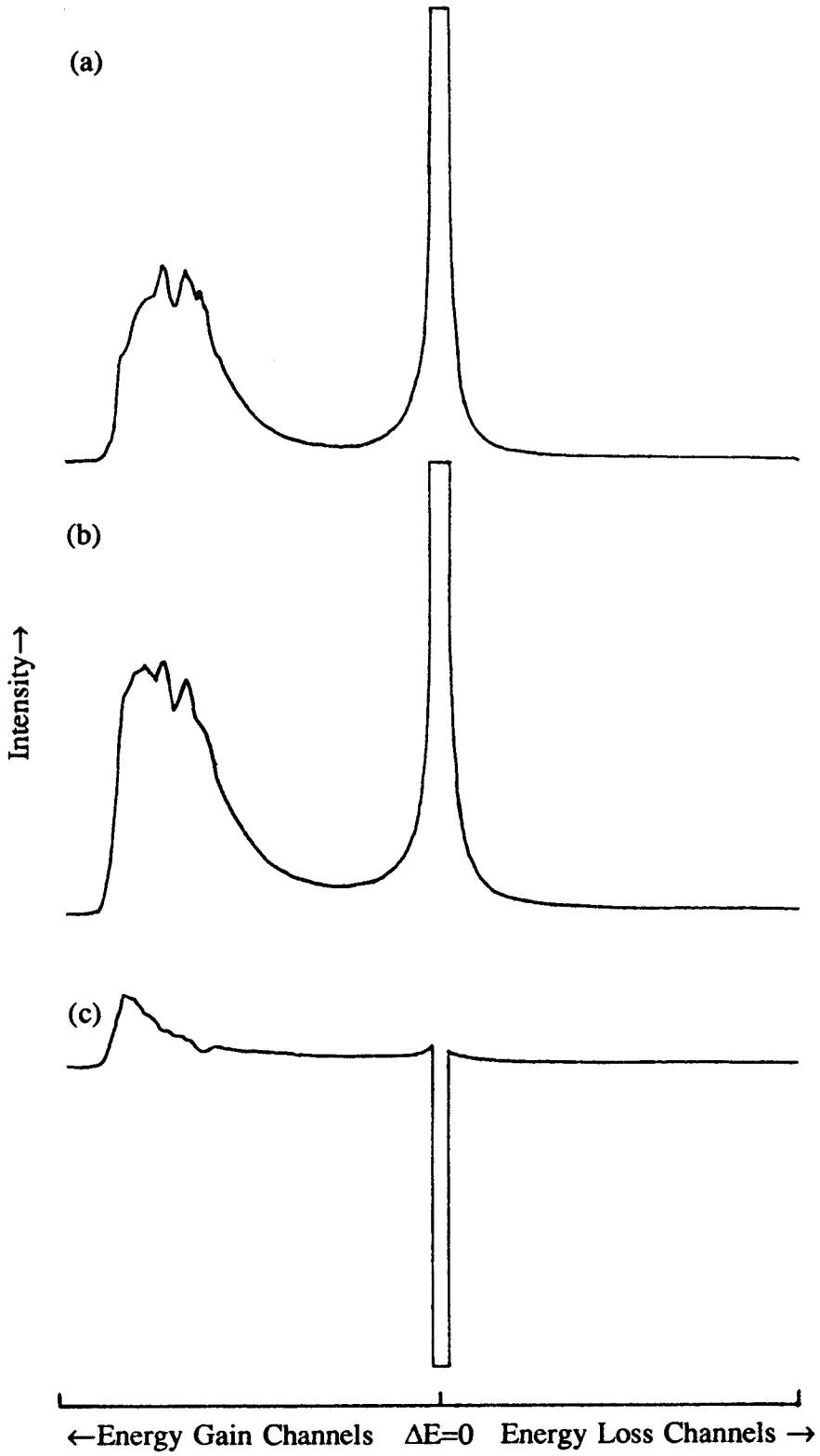

Figure 5.5 Raw inelastic neutron scattering data for $HSbO_3.0.75H_2O$ recorded at 5.9 Å, showing summed time-of-flight spectra at (a) 300 K and (b) 400 K, with (c) (not on same intensity scale) the difference of the two.

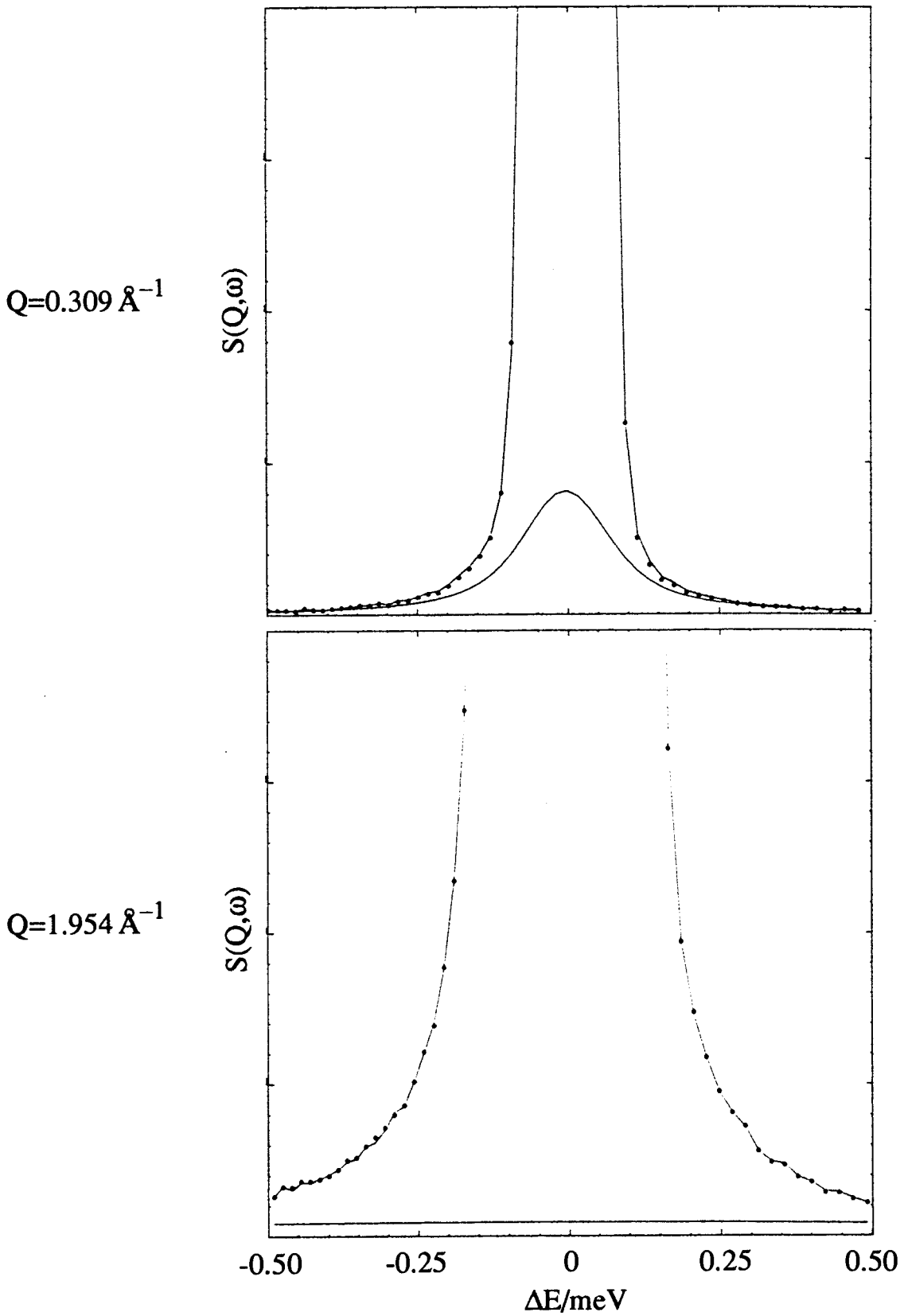

Figure 5.6 Fitted QENS spectra for $HSbO_3.0.75H_2O$ at 80 K and for Q=0.309 Å^{-1} and 1.954 Å^{-1}. Both plots show experimental data (points), fitted quasielastic component (lower continuous line) and total fitted spectrum (upper line).

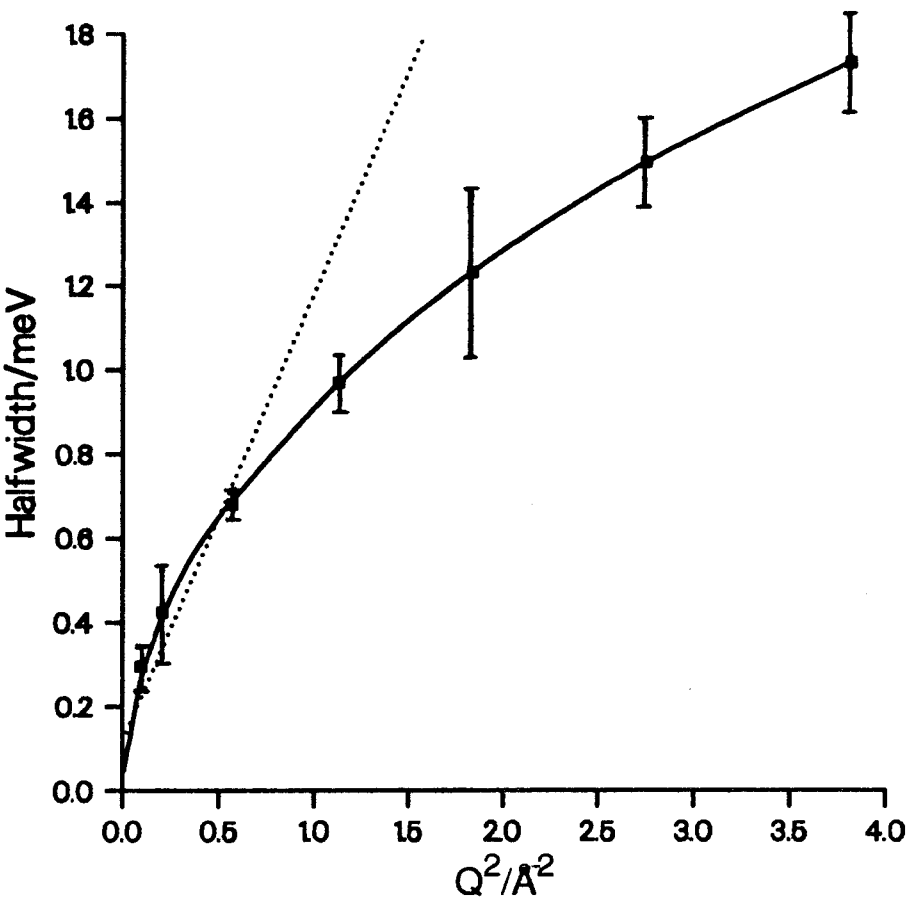

Figure 5.7 Variation of the halfwidth of the fitted quasielastic component with Q^2 for $HSbO_3.0.75H_2O$ at 80 K (error bars represent ±1 e.s.d). The linear least squares fit to points below $Q=1$ Å^{-1} is shown as a broken line.

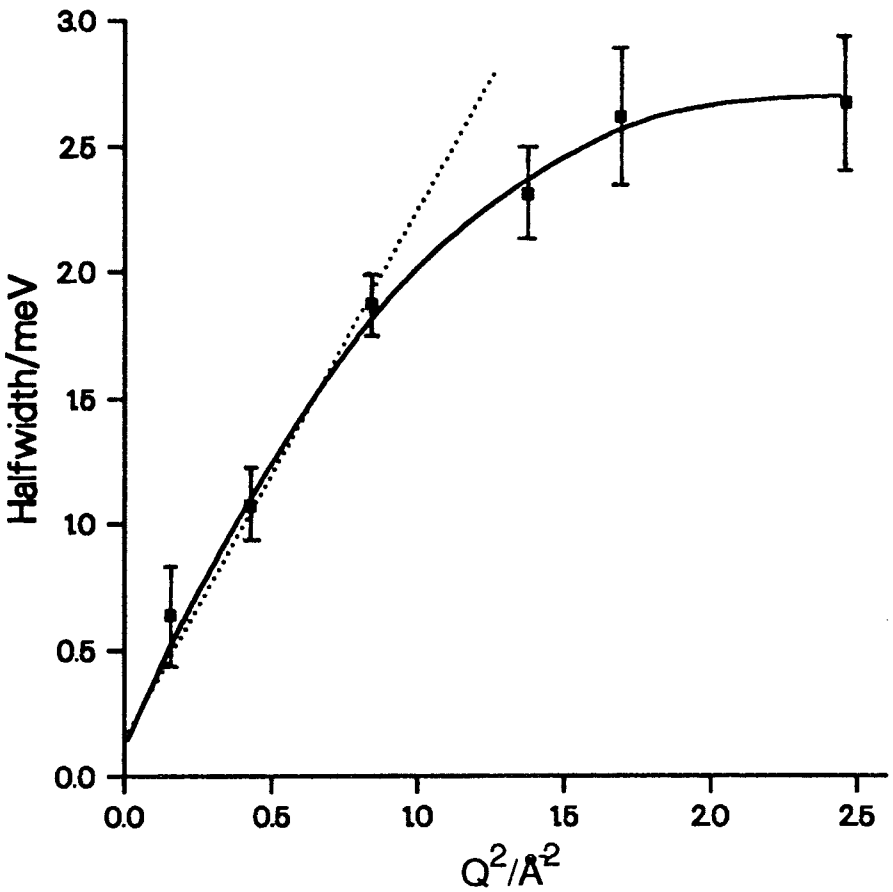

Figure 5.8 Variation of the halfwidth of the fitted quasielastic component with Q^2 for $HSbO_3.0.75H_2O$ at 300 K (error bars represent ±1 e.s.d). The linear least squares fit to points below Q=1 $Å^{-1}$ is shown as a broken line.

at 80 K $D = 2.6(\pm 0.6)\times 10^{-9}\ m^2\ s^{-1}$

at 300 K $D = 5.1(\pm 0.6)\times 10^{-9}\ m^2\ s^{-1}$

$NH_4HTa_2O_6$ and NH_4TaWO_6

Both these materials exhibited substantial temperature-dependent broadening of the elastic peak. For NH_4TaWO_6 this was observed over eight temperatures in the range 80 K to 340 K and is illustrated in figure 5.9. Again raw data are shown for 80 K and 340 K together with the difference between the two.

A similar broadening was observed for $NH_4HTa_2O_6$ over the same temperature range. For both compounds the raw data indicated that the broadening increased continuously over the whole temperature range i.e. there was no discernible "levelling off" at any particular temperature.

In the time available it was only possible to fit the data for $NH_4HTa_2O_6$ at 340 K. The plot of Lorentzian halfwidth against Q^2 is shown in figure 5.10. It can be seen that, as for $HSbO_3.0.75H_2O$, the broadenings are of the order of magnitude of 1 meV and that there is a sharp increase in the broadening with Q^2 up to $Q^2=1.5\ Å^{-2}$. The single data point at higher Q indicates that the breadth of the quasielastic component then remains roughly constant, although intermediate points would be needed to confirm this effect. Again a straight line was fitted by a least squares method to points below $Q=1\ Å^{-1}$. The calculated self-diffusion coefficient was

$$D = 2.2(\pm 0.2)\times 10^{-9}\ m^2\ s^{-1}$$

5.6 Discussion

It is apparent that in cubic $HSbO_3.0.75H_2O$ and in the ammonium-containing pyrochlores rapid protonic motion occurs, giving rise to a large quasielastic broadening. Due to the Q-dependence of the broadening it is inferred that translational

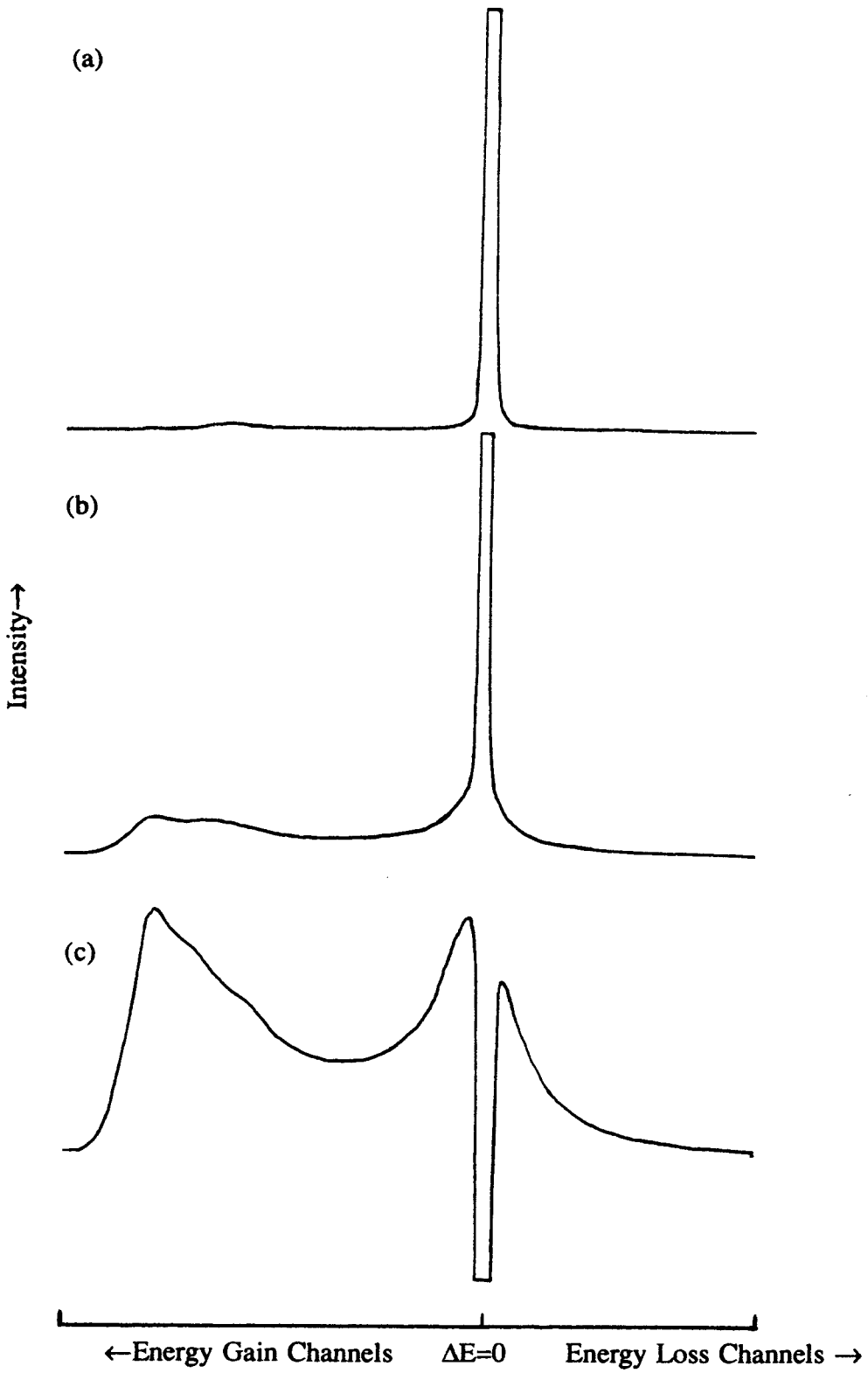

Figure 5.9 Raw inelastic neutron scattering data for NH_4TaWO_6, showing summed time-of-flight spectra at (a) 80 K and (b) 340 K, with (c) (on expanded intensity scale) the difference of the two.

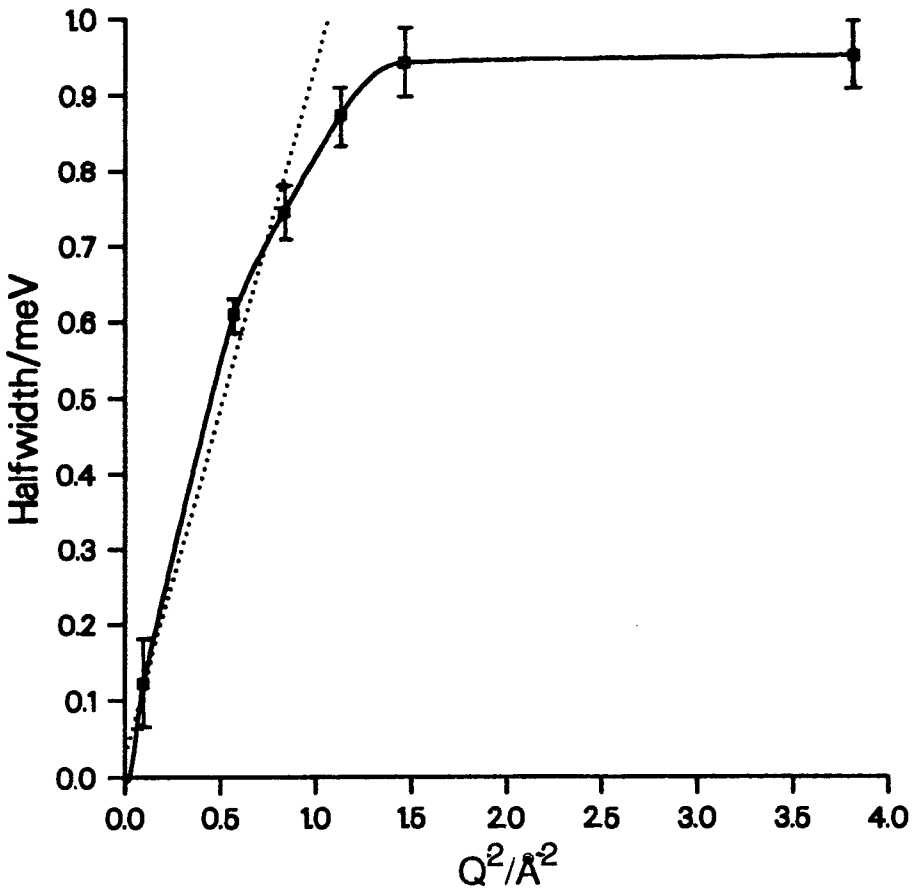

Figure 5.10 Variation of the halfwidth of the fitted quasielastic component with Q^2 for $NH_4HTa_2O_6$ at 340 K (error bars represent ±1 e.s.d). The linear least squares fit to points below Q=1 $Å^{-1}$ is shown as a broken line.

motion of protons contributes at least a part of this motion. In fact a smooth, but non-linear, increase of Γ with Q^2 is consistent with translational diffusion in a spatially restricted environment such as the interconnected cavities of the $HSbO_3$ and pyrochlore frameworks. The diffusion coefficients obtained for both compounds are larger than for the other hydrated compounds mentioned previously, being two orders of magnitude greater than in HUP and four orders of magnitude greater than in $H_3O^+\beta''$–alumina, these compounds ostensibly having similar conductivities to $HSbO_3.xH_2O$.

Normally localised rotations are found to occur on a faster timescale than translational motion. However it is possible that molecular reorientation is in some way correlated to translational motion. Indeed Kuntz et al.[18] proposed that in NH_4TaWO_6 a proton is transferred with each rotation of NH_4^+. If this is the case then in the present QENS experiment rotational and translational motion are being observed simultaneously in $NH_4HTa_2O_6$.

A simple analysis of the diffusion coefficient for this material may be performed using a jump model. It is assumed that proton hopping occurs only between equivalent sites on neighbouring ammonium ions and that the distance for this is 2.3 Å, as for NH_4TaWO_6. If each jump is accompanied by a random reorientation of NH_4^+ the number of possible equivalent jump sites is 4. Although somewhat idealised, this model yields a residence time of 1×10^{-10} s i.e. the same timescale observed by Butler and Biefeld[19] for proton motion in NH_4TaWO_6, using NMR.

In the case of $HSbO_3.0.75H_2O$ the situation is complicated by the presence of inequivalent cavity sites. As described in chapter 4, the intercavity water is distributed over two partially occupied sites, on one as H_3O^+ and on the other as H_2O, associated by hydrogen bonding to a framework-bound proton. Proton diffusion is

most likely to be facilitated by the high number of unoccupied proton sites.

With such a complex structure, a quantitative model to account for the observed QENS spectra is inappropriate. However a possible pathway to account for rapid translational of protons is here presented. Transfer of the framework-bound proton, D(4), to the water molecule (O(4) site) involves a distance of 1.2 Å to the nearest unoccupied D(2) proton site and will result in a reorientation of the water molecule. Proton transfer to the nearest possible occupied H_3O^+ site then involves a jump distance of 2.8 Å. The final step involves migration of a proton from H_3O^+ to the nearest D(4) site. It is expected that reorientation of both H_3O^+ and H_2O are relatively rapid processes. In the case of H_3O^+, rotation about its threefold axis involves no redistribution of hydrogen bonds and should have a low activation energy. For H_2O the rotational disorder of the molecule means that there are three closely-situated equivalent sites for each water proton and rotation about the C_3 axis should be similarly favoured.

Assuming that these processes present no barrier to long-range diffusion, then rapid translational motion is expected if there is a high probability of a proton jump with each molecular reorientation.

The final observation to be accounted for is the lack of evidence for proton motion in $H_2OH_2Ta_2O_6$. Unlike NH_4^+, which is thought to rotate easily due to its tetrahedral symmetry and to the weaker hydrogen bonding to the framework, the more polar H_2O will experience strong hydrogen bonding. Moreover the hydrogen bonds will have the effect of constraining the water within the plane of its atoms and therefore increase the activation energy of the C_2 rotation. In contrast to $HSbO_3.xH_2O$, where the water is situated on the sides of a large cavity, it is here in the centre of the pyrochlore cavity with a larger distance between water molecules of

4.6 Å. All this is consistent with proton diffusion being on a longer timescale than in the other compounds studied, and therefore not observed in the present QENS experiment.

In conclusion, the present experiments have provided a useful indication of the timescale of protonic motion in the materials studied. However further, and more accurate, work is required to characterise this property more fully. For $HSbO_3.xH_2O$, resolving the motions of the various protonic species will probably require measurements at a range of resolutions and access to a higher range of Q than in the present study. For the hydrated pyrochlores higher resolution is certainly required to access the expected longer timescale of the motions. The ammonium-containing pyrochlores are particularly interesting as potential proton conductors, due both to the rapid proton motion observed and to their higher thermal stability, and merit more detailed study than has been accorded to them hitherto. In addition to further neutron scattering work, a conductivity study would be worthwhile.

CHAPTER 6

MISCELLANEOUS ION-EXCHANGE AND INTERCALATION REACTIONS

PART A: Ion Exchange of Antimonophosphates

6.1 Introduction

As described in chapter 1, a series of phosphates containing potassium and antimony(V) has been synthesised by the group of Piffard. It had been found that some of these compounds were able to be ion-exchanged in acidic media to form hydrated antimonophosphates. In particular the layered material $K_3Sb_3P_2O_{14}$ may be ion-exchanged to form $H_3Sb_3P_2O_{14}.xH_2O$[1]. The amount of water that may be accommodated in the structure is high, with $0 \leq x \leq 10$. For x=10 the interlayer spacing is more than 5 Å greater than in the dehydrated compound. The highly acidic nature of the material gave rise to speculation that this and other protonated antimonophosphates might exhibit a high degree of protonic conductivity. The analogous antimonic acid $H_2Sb_4O_{11}.nH_2O$, prepared by ion exchange of $K_2Sb_4O_{11}$, was found to possess room temperature conductivities of 10^{-3} and $10^{-6}(\Omega cm)^{-1}$ for n=3 and n=2 respectively[2]. The compound $HSbP_2O_8$ was first prepared, directly from $SbCl_5$ and H_3PO_4, by Winkler and Thilo in 1966[3]. Although the exact structure of this layered acid was not known at the time, the authors demonstrated that two moles of water could be intercalated, giving rise to a 2 Å increase in the *c* lattice parameter. They also showed that it was strongly acidic, with protons being able to be replaced by alkali cations.

In the present work the three-dimensional channel-containing compound KSb_2PO_8 has been ion exchanged and characterised, and a more limited study has been carried out on the layered material $KSbP_2O_8$. The framework structures of both

these compounds are described in chapter 1.

6.2 Synthesis and Characterisation of KSb_2PO_8 and $HSb_2PO_8.xH_2O$

Synthesis

The parent compound was synthesised according to the method of Piffard et al.[4] $NH_4H_2PO_4$ (Aldrich, 99.999%), KNO_3 (BDH, AnalaR) and Sb_2O_3 (Aldrich, >99%) were ground together intimately in equimolar proportions. The white mixture was then transferred to an alumina boat and heated in air for 4 h at 200 °C to decompose the ammonium compound. The temperature was then raised to 900 °C. After a further 24 h at this temperature, the product was allowed to cool at the slow rate of 1 °C min^{-1} in order to obtain maximum crystallinity. KSb_2PO_8 appeared as a fine white crystalline powder. Typically about 8 g was produced in a single preparation.

$HSb_2PO_8.xH_2O$ was prepared by the reaction of KSb_2PO_8 with 3M HNO_3 (May & Baker, Lab. Reag.), about 120 cm^3 of the dilute acid being used with 5 g of solid. The mixture was stirred in a pyrex flask at 80 °C for 24 h, after which period the acid was changed and the reaction allowed to continue for a further 24 h. The product was then filtered off, washed with distilled water and stored in a desiccator over $CaCl_2$.

KSb_2PO_8 and $HSb_2PO_8.xH_2O$ were characterised by powder x-ray diffraction and infrared spectroscopy. In addition, KSb_2PO_8 was studied by solid state NMR and flame photometry was used to gauge the extent of the ion-exchange reaction.

Flame Photometry

The total amount of potassium in the acidic solutions, after the ion-exchange product had been separated, was determined by flame photometry. The instrument was calibrated as described previously, and the determined potassium content corresponded to 99(±3)% of that of the starting material, assuming that this was a

pure phase of KSb_2PO_8. In the absence of any direct measure of the degree of hydration the exchanged material is here referred to as $HSb_2PO_8.xH_2O$.

X-Ray Powder Diffraction

The x-ray powder pattern of KSb_2PO_8 indicated a pure crystalline phase. All the diffraction peaks could be indexed on the basis of a monoclinic unit cell of space group Cc with closely similar cell parameters to those reported by Piffard et al.[4] These parameters were refined to be

$$a=12.299(2)\,\text{Å},\ b=7.081(1)\,\text{Å},\ c=15.010(2)\,\text{Å},\ \beta=95.85(1)^\circ$$

(Literature: $a=12.306(4)\,\text{Å},\ b=7.086(2)\,\text{Å},\ c=15.037(5)\,\text{Å},\ \beta=95.82(3)^\circ$).

The diffraction pattern of the exchanged material could also be indexed in the space group Cc with the lattice parameters

$$a=12.310(3)\,\text{Å},\ b=7.088(2)\,\text{Å},\ c=15.011(3)\,\text{Å},\ \beta=95.92(2)^\circ.$$

It can be seen that the unit cell has essentially the same dimensions as that of KSb_2PO_8, although the powder pattern of $HSb_2PO_8.xH_2O$ showed a broadening of the diffraction peaks, indicating a degree of inhomogeneity in the crystalline phase and also preventing the identification of weaker reflections. It is therefore evident that the $(Sb_2PO_8)^-$ framework structure remains fundamentally unaltered during the ion-exchange proceess. The powder diffraction data for KSb_2PO_8 and $HSb_2PO_8.xH_2O$ are given in tables 6.1 and 6.2 respectively.

Infrared Spectroscopy

The infrared spectra of KSb_2PO_8 and $HSb_2PO_8.xH_2O$, recorded as pressed CsI discs, are shown in figure 6.1. It can be seen that below $1300\,cm^{-1}$, the spectrum of KSb_2PO_8 is highly complex due to the low symmetry of the unit cell, although at higher frequencies there is only a weak band at *ca.* $3460\,cm^{-1}$ due to the presence of

Table 6.1 Observed and Calculated Powder Diffraction Data for KSb_2PO_8

h k l	2θ*(obs)*	2θ*(calc)*	*h k l*	2θ*(obs)*	2θ*(calc)*
0 0 2	11.85	11.84	4 2 -3	41.73	41.71
1 1 0	14.48	14.44	5 1 -4	43.99	43.99
2 0 0	"	14.48	4 0 -6	44.51	44.50
1 1 -1	15.34	15.33	1 1 7	45.71	45.71
1 1 1	15.89	15.90	1 3 4	46.46	46.48
2 0 -2	17.78	17.77	6 0 2	47.35	47.36
1 1 2	19.20	19.18	4 2 -5	47.78	47.78
2 0 2	19.69	19.66	6 0 -4	48.61	48.61
1 1 -3	22.40	22.41	4 0 6	49.49	49.48
0 0 4	23.81	23.82	0 2 7	49.89	49.87
3 1 0	25.19	25.18	1 1 -8	50.33	50.33
3 1 -1	25.39	25.36	2 2 -7	50.85	50.85
0 2 1	25.85	25.84	6 2 -1	51.51	51.50
2 0 -4	26.64	26.66	0 4 0	51.60	51.58
1 1 -4	27.32	27.31	4 2 5	51.77	51.76
1 1 4	28.61	28.60	6 2 1	52.67	52.65
3 1 2	28.84	28.87	1 3 -6	53.46	53.46
2 0 4	29.24	29.24	7 1 -1	53.71	53.71
2 2 -1	29.44	29.43	2 4 0	53.88	53.87
3 1 -3	29.66	29.66	7 1 1	55.04	55.02
2 2 1	30.02	30.04	2 4 2	55.75	55.73
2 2 2	30.98	30.97	3 3 5	"	55.76
3 1 3	32.32	32.31	4 2 -7	56.31	56.31
4 0 2	32.73	32.72	1 1 -9	56.70	56.69
3 1 -4	33.32	33.31	6 2 -5	58.24	58.22
2 2 -3	33.53	33.52	2 4 -4	59.01	59.00
1 1 5	34.02	34.03	8 0 -2	60.49	60.49
2 2 3	35.12	35.14	0 2 9	61.73	61.69
4 0 -4	36.02	35.99	0 0 10	62.13	62.11
0 0 6	"	36.06	4 4 2	62.47	62.44
3 1 4	36.48	36.49	2 0-10	"	62.46
2 0 -6	37.59	37.57	6 2 5	63.46	63.44
1 1 -6	38.31	38.30	6 0 -8	64.05	64.05
4 2 -1	38.88	38.88	4 4 -4	64.56	64.50
1 3 1	39.42	39.43	0 4 6	"	64.55
0 2 5	"	39.44	2 2 9	65.25	65.25
5 1 -2	39.65	39.64	2 0 10	65.81	65.82
1 1 6	39.73	39.75	4 0-10	66.80	66.80
4 0 4	39.95	39.93	2 4 6	67.55	67.54
5 1 1	"	39.99	8 2 1	"	67.54
2 0 6	40.47	40.47	8 2 -5	71.45	71.47
3 1 5	41.24	41.23	6 4 2	72.59	72.61

λ=1.5406 Å

a=12.299(2) Å, b=7.081(1) Å, c=15.010(2) Å, β=95.85(1)°

Table 6.2 Observed and Calculated Powder Diffraction Data for $HSb_2PO_8.xH_2O$

h k l	*2θ(obs)*	*2θ(calc)*	*h k l*	*2θ(obs)*	*2θ(calc)*
0 0 2	11.83	11.84	3 3 0	44.34	44.26
2 0 0	14.46	14.46	4 0 0	"	44.35
1 1 -1	15.31	15.32	4 2 3	"	44.36
1 1 1	15.88	15.89	1 1 7	45.72	45.71
2 0 -2	17.74	17.75	1 3 4	46.46	46.45
1 1 2	19.20	19.18	6 0 2	47.37	47.34
2 0 2	19.64	19.66	3 3 3	48.98	48.99
1 1 -3	22.40	22.34	2 2 -7	50.84	50.82
0 0 4	23.80	23.82	4 2 5	51.76	51.76
3 1 0	25.17	25.16	7 1 -1	53.76	53.66
2 0 -4	26.63	26.63	5 3 -1	"	53.78
3 1 2	28.85	28.86	2 4 0	"	53.81
2 2 -1	29.45	29.40	4 0 -8	54.83	54.86
3 1 -3	"	29.62	2 4 2	55.69	55.68
2 2 1	29.98	30.02	4 2 -7	56.26	56.25
0 2 3	30.96	30.95	8 0 -2	60.42	60.42
3 1 3	32.30	32.31	0 2 9	61.68	61.68
4 0 2	32.69	32.72	6 2 5	63.41	63.43
3 1 -4	33.30	33.28	0 4 6	64.48	64.50
2 2 3	35.14	35.12	2 2 9	65.25	65.25
4 0 -4	36.03	35.94	4 0-10	66.81	66.76
0 0 6	"	36.06	7 1 -7	"	66.84
4 2 -1	38.84	38.84	8 2 -3	67.48	67.47
5 1 -2	39.58	39.59	1 5 -2	"	67.48
2 0 6	40.48	40.48	8 2 1	"	67.49
			2 4 6	"	67.50
			1 3 -9	68.87	68.88

λ=1.5406 Å
a=12.310(3) Å, b=7.088(2) Å, c=15.011(3) Å, β=95.92(2)°

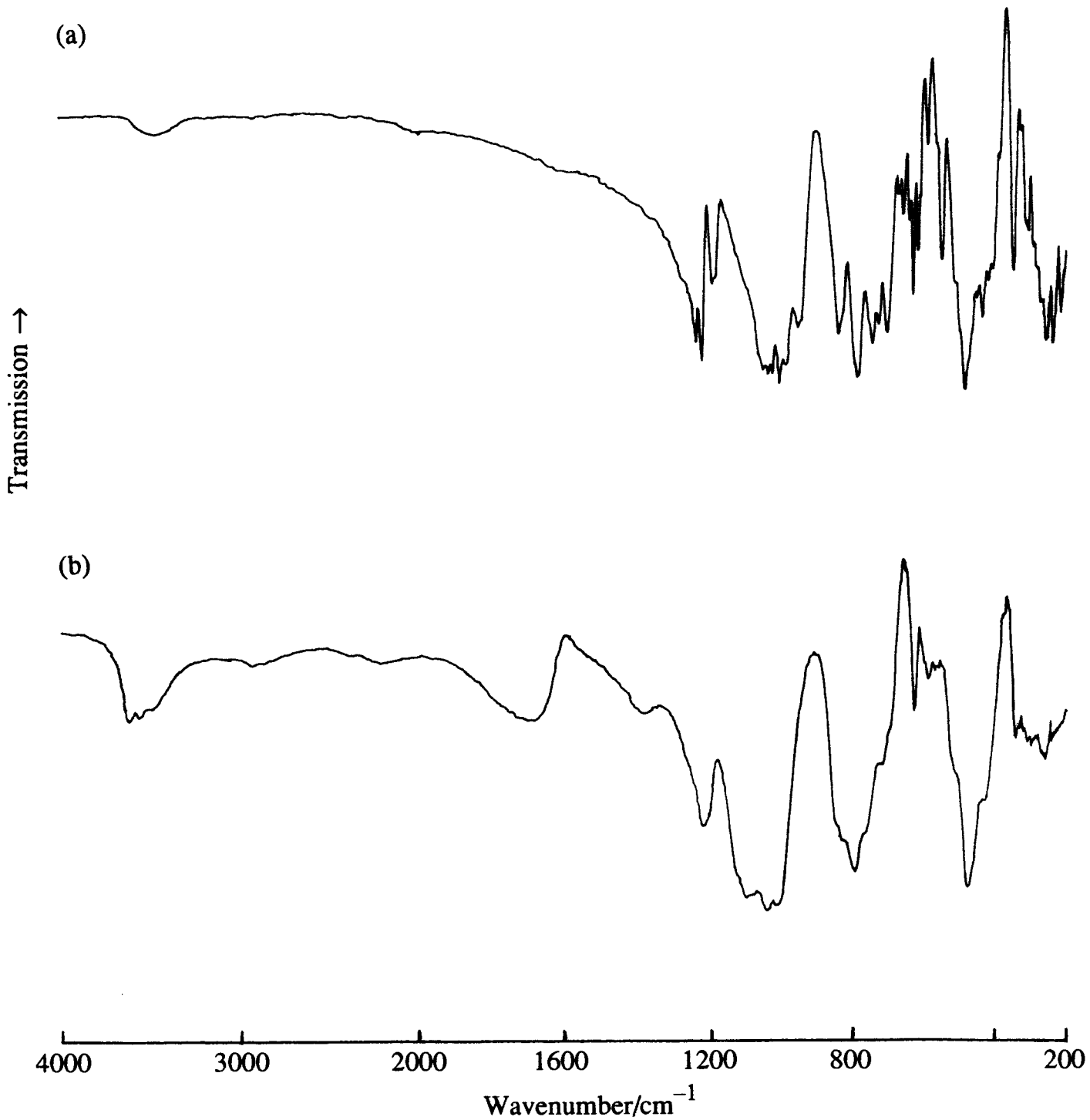

Figure 6.1 Infrared spectra of (a) $KSbP_2O_8$ and (b) $HSbP_2O_8.xH_2O$, recorded as pressed CsI discs.

some absorbed water. Since this work was carried out, an analysis of the vibrational spectra of various antimonophosphates, including the present material, has been published by Husson et al.[5] For KSb_2PO_8 285 infrared-active modes are predicted. Based on these authors' work, the observed absorption bands are assigned as follows:

Between 920 and 1240 cm^{-1} P–O stretching modes are found, with the group of bands in the region 1160-1240 cm^{-1} assigned to antisymmetric stretching of the PO_4^{3-} tetrahedron and the multiplet between 920 and 1050 cm^{-1} to symmetric modes of PO_4^{3-}. Between 670 and 840 cm^{-1} Sb–O stretching occurs, with that due to Sb–O(edge-sharing) being at higher frequencies than that due to Sb–O...Sb(corner-sharing). Below 650 cm^{-1} assignment is more complex owing to the presence of coupled O–Sb–O and O–P–O bending modes and Sb–O...P stretching.

Below 1300 cm^{-1}, the spectrum of $HSb_2PO_8.xH_2O$ is essentially identical to that of the parent compound, although less well resolved. However strong, broad absorptions at *ca.* 1680 (H_2O bending) and *ca.* 3560 cm^{-1} (O–H stretching) indicate a substantial degree of hydration as well as the presence of hydrogen bonding.

Solid State NMR

The magic angle spinning solid state ^{31}P NMR spectrum of KSb_2PO_8, recorded at 121.4 MHz, is shown in figure 6.2. A single line is observed at –25.1 ppm (referenced to δ=0 for H_3PO_4) with two weak spinning side bands. Recently published work by Taulelle et al.[6] includes an almost identical spectrum for KSb_2PO_8 together with an interpretation of the ^{31}P NMR spectra of this and other antimonophosphates. A correlation was found between the number of bridging oxygens in the PO_4^{3-} group and the observed chemical shift. In the case of KSb_2PO_8 all the phosphate oxygens fall into this category, i.e. none are "terminal" oxygens, and therefore the observed

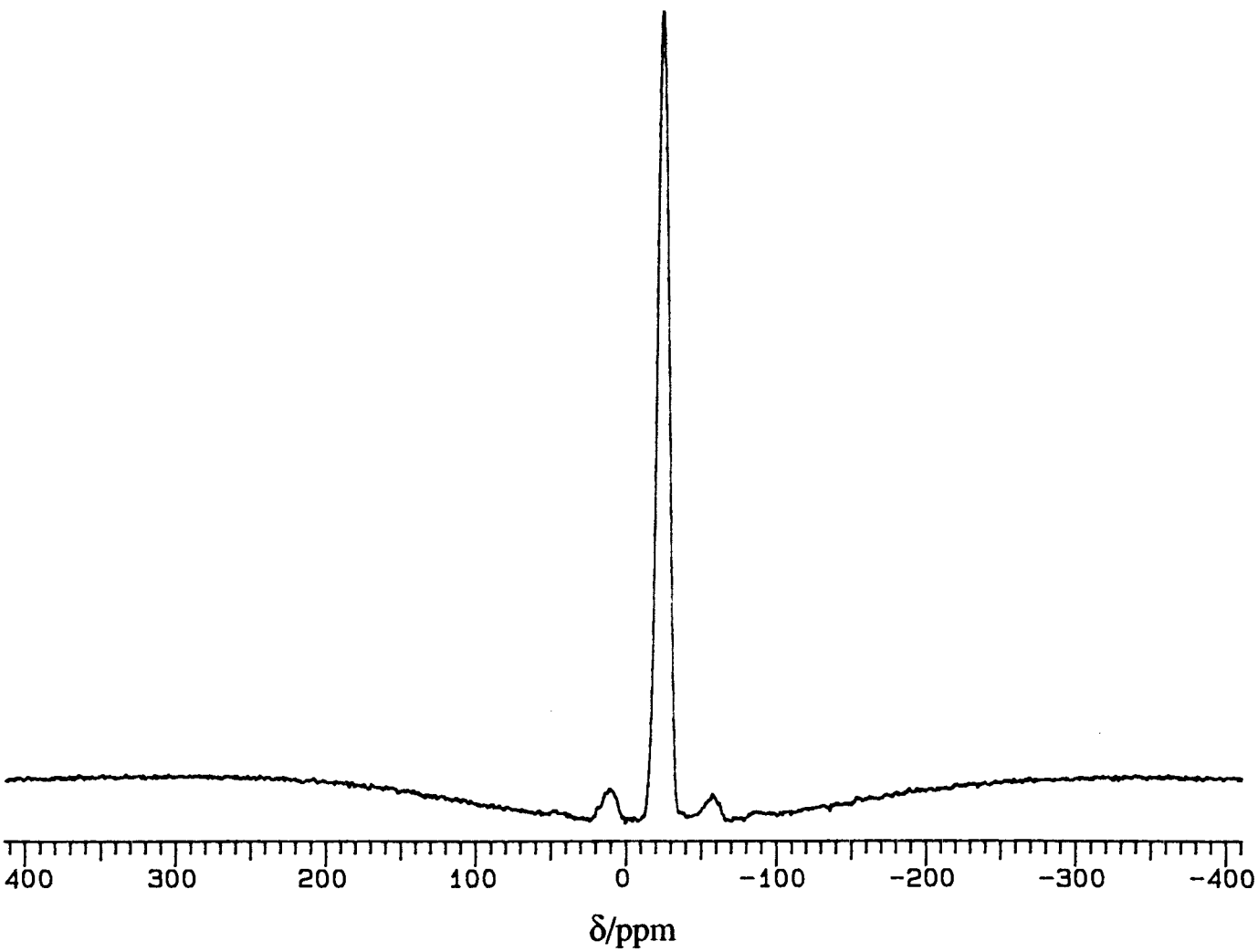

Figure 6.2 Solid State ^{31}P NMR spectrum of KSb_2PO_8 (frequency 121.4 MHz, referenced to δ=0 for H_3PO_4).

chemical shift is among the largest found in this class of compound. Although in the true symmetry of the unit cell there are two distinct P sites, the structure represents only a small deviation from the space group C2/c which includes a centre of inversion. The two P sites therefore have essentially the same chemical environment, evidenced by the single NMR peak.

6.3 Ion Exchange of $KSbP_2O_8$

$KSbP_2O_8$ was prepared, according to the method of Piffard et al.[7], from the same starting materials as KSb_2PO_8. $NH_4H_2PO_4$, KNO_3 and Sb_2O_3 were intimately ground together in the respective molar ratio 4:2:1. The mixture was heated in air for 4 h at 200 °C to decompose the ammonium compound, and then at 900 °C for a further 24 h, as previously. The product was cooled at the rate of 1 °C min^{-1}. $KSbP_2O_8$ appeared as a fine white crystalline powder.

$KSbP_2O_8$ was characterised by powder x-ray diffraction and solid state NMR. The powder diffraction pattern could be indexed in the rhombohedral space group $R\bar{3}$, with the exception of eight peaks at low angle whose intensities were of the order of 1% of that of the most intense $KSbP_2O_8$ peak. Most of these could be ascribed to the presence of $K_4P_2O_7$. The refined cell parameters of $KSbP_2O_8$ were similar to those reported by Piffard et al.:

$$a=b=4.764(1)\ \text{Å},\ c=25.426(6)\ \text{Å},\ \alpha=\beta=90°,\ \gamma=120°$$

(literature: $a=b=4.7623(4)$ Å, $c=25.409(4)$ Å, $\alpha=\beta=90°$, $\gamma=120°$).

Observed and calculated peak positions are given in table 6.3.

The solid state ^{31}P NMR spectrum of $KSbP_2O_8$ is shown in figure 6.3. Considering there is only one distinct P site in this material, the spectrum is quite complex, with the most intense peak at -18.8 ppm being surrounded by an uneven "comb" of

Table 6.3 Observed and Calculated Powder Diffraction Data for $KSbP_2O_8$

h k l	*2θ(obs)*	*2θ(calc)*	*h k l*	*2θ(obs)*	*2θ(calc)*
0 0 3	10.50	10.43	0 2 13	65.73	65.74
0 0 6	21.04	20.95	0 0 18	66.12	66.09
1 0 1	21.87	21.81	1 2 8	66.80	66.77
0 1 2	22.69	22.64	1 1 15/1 1-15	67.82	67.80
1 0 4	25.72	25.72	3 0 0	68.07	68.13
0 1 5	27.79	27.82	2 0 14	68.82	68.82
0 0 9	31.63	31.64	3 0 3/0 3 3	69.11	69.14
1 0 7	32.80	32.82	2 1 10/1 2-10	70.80	70.83
0 1 8	35.61	35.63	3 0 6/0 3 6	72.07	72.15
1 1 0	37.74	37.74	1 2 11/2 1-11	73.09	73.15
1 1 3/1 1 -3	39.25	39.26	1 0 19	74.46	74.48
1 0 10	41.69	41.69	0 2 16	75.40	75.45
0 0 12	42.61	42.64	3 0 9/0 3 9	77.05	77.06
1 1 6/1 1 -6	43.53	43.55	1 1 18/1 1-18	78.68	78.69
0 2 1	43.93	44.00	2 2 0	80.50	80.59
2 0 2	44.41	44.46	1 2 14/2 1-14	81.25	81.25
0 1 11	44.90	44.91	3 0 12/0 3 12	83.81	83.79
0 2 4	46.21	46.23	2 2 6/2 2 -6	84.40	84.41
2 0 5	47.50	47.53	1 3 1/3 1 -1	84.75	84.73
1 1 9/1 1 -9	50.00	50.05	3 1 2/1 3 2	85.05	85.05
0 2 7	50.85	50.86	1 3 4/3 1 4	86.32	86.31
1 0 13	51.63	51.68	0 2 19	86.65	86.65
2 0 8	52.84	52.87	2 1 16/1 2-16	87.59	87.59
0 0 15	54.05	54.06	2 2 9/2 2 -9	89.22	89.16
0 1 14	55.24	55.22	1 3 7/3 1 -7	89.77	89.78
0 2 10	57.51	57.48	2 0 20	90.74	90.75
1 1 12/1 1-12	58.26	58.23	3 1 8/1 3 -8	91.35	91.36
2 1 1/1 2 -1	59.36	59.33	0 0 24	93.25	93.29
2 0 11	60.11	60.07	1 3 10/3 1-10	95.21	95.16
2 1 4/1 2 -4	61.17	61.14	2 2 12/2 2-12	95.88	95.79
1 2 5/2 1 -5	62.23	62.22	0 4 2	97.00	97.05
1 0 16	62.62	62.59	3 1 11/3 1-11	97.48	97.38
2 1 7/1 2 -7	65.05	65.04	4 0 4	98.40	98.33

λ=1.5406 Å

a=b=4.764(1) Å, c=25.426(6) Å, $\alpha=\beta=90°$, $\gamma=120°$

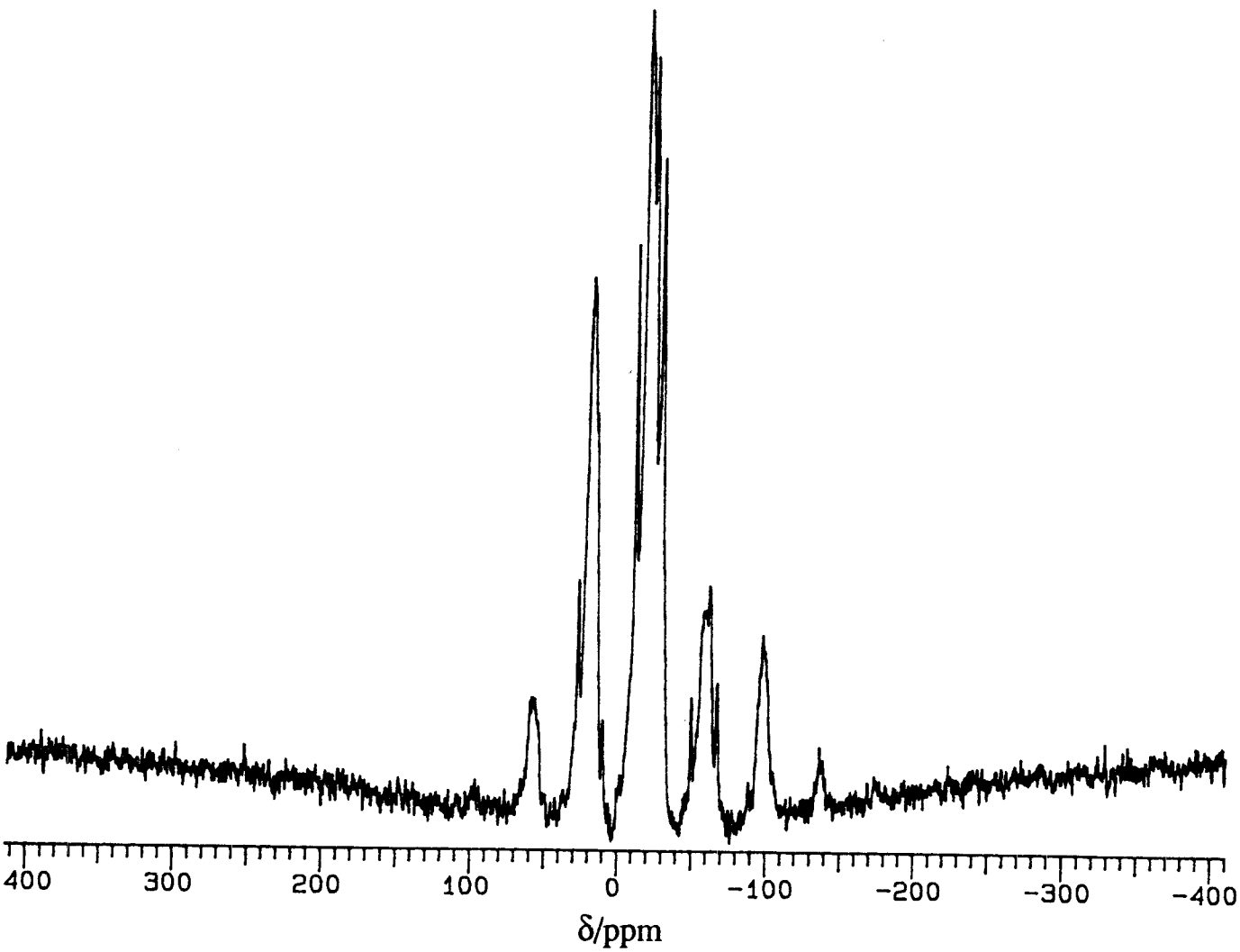

Figure 6.3 Solid State ^{31}P NMR spectrum of $KSbP_2O_8$ (frequency 121.4 MHz, referenced to δ=0 for H_3PO_4).

five other lines. Within these principal peaks finer structure is observed. Taulelle et al.[6] only observed a peak at -18.8 ppm with two spinning side bands, -18.8 being in the range expected where the PO_4^{3-} tetrahedron contains three bridging and one terminal oxygen. However they also observed that hydration of the phosphates results in shifts of the ^{31}P resonances, often to higher field. The spectrum in figure 6.3 is thus explained by the presence of partially hydrated $KSbP_2O_8$, with one or more spectra superimposed on that of the pure phase.

The attempt was made to ion-exchange $KSbP_2O_8$ in 3M HNO_3. About 5 g was stirred in 120 cm^3 of dilute acid at 80 °C for 48 h, with the acid being changed once after 24 h. The reaction was carried out a number of times with different samples of $KSbP_2O_8$. After each attempt the solid was filtered off from the solution, which was then analysed by flame photometry in order to determine the potassium content. The best figure that was obtained corresponded to 36(±3)% of the assumed K content of the $KSbP_2O_8$. Attempts to improve the degree of ion exchange by using 6M HNO_3 and by allowing the reaction to continue for several days longer produced no improvement on this result.

6.4 Discussion

Very recent work by the group of Piffard[8] has shown that $HSbP_2O_8.xH_2O$ may be prepared by reaction of $KSbP_2O_8$ with 9M HNO_3 at 50 °C. X-ray diffraction and conductivity studies were carried out on this material and on $H_3Sb_3P_2O_{14}.xH_2O$ and $H_5Sb_5P_2O_{20}.xH_2O$, together with measurements of water adsorption as a function of relative humidity. For $HSbP_2O_8.xH_2O$ it was found that the water content, x, increased to a value of 10 at 100% relative humidity. However it was evident from the measured increase in the interlayer spacing that not all the water could have been accommodated within the structure and part of it was therefore surface-adsorbed. The

material exhibited a conductivity of $10^{-2}(\Omega cm)^{-1}$ at maximum water content and room temperature. This was ascribed to interparticle water; the value for bulk conductivity was estimated to be at least three orders of magnitude smaller.

The other two compounds however exhibited conductivities which could be ascribed to bulk processes. In the case of $H_3Sb_3P_2O_{14}.xH_2O$, there was a close correlation between water content, interlayer spacing and conductivity, which increased to a value of $10^{-2}(\Omega cm)^{-1}$ for x=12. For $H_5Sb_5P_2O_{20}.xH_2O$, a bulk room temperature conductivity of $10^{-4}(\Omega cm)^{-1}$ was determined ($x \cong 5$).

In the present work, complete ion exchange of $KSbP_2O_8$ was not achieved. However the relative difficulty with which ion exchange occurs is consistent with the acid exchange product being a poor bulk proton conductor. On the other hand $HSb_2PO_8.xH_2O$, which has not yet been reported in the literature, is prepared easily by ion exchange of the potassium analogue. The material may thus be a better bulk conductor, as is the similarly three-dimensional $H_5Sb_5P_2O_{20}.xH_2O$, and conductivity studies should be a priority in any further characterisation of the compound.

PART B: Intercalation Reactions of $MoO_2HPO_4.H_2O$

6.5 Introduction

As described in chapter 1, many low-dimensional inorganic compounds are able to undergo intercalation reactions whereby guest species are inserted into the host, which retains its framework structure. In particular acidic framework oxides may react with organic bases such as alcohols and amines to form intercalates, as in the case of $Zr(HPO_4)_2.H_2O$ (α–ZrP) where high values of proton conductivity have been

found with some organic intercalants. In chapter 3 the structure of $MoO_2HPO_4.H_2O$ is presented. This proton-conducting chain-structured material is similar to α–ZrP in that it possesses an acidic P–O–H group and also a coordinated water molecule, whose protons may also participate in the conduction mechanism.

In this chapter a preliminary investigation is reported of reactions between $MoO_2HPO_4.H_2O$ and the primary alyklamines ethylamine ($EtNH_2$), *n*–propylamine ($PrNH_2$) and *n*–butylamine ($BuNH_2$).

6.6 Experimental

$MoO_2HPO_4.H_2O$ was prepared from MoO_3 and H_3PO_4 in HNO_3, as described in chapter 3.

As an initial experiment, the direct reaction between approximately 0.5 g of $MoO_2HPO_4.H_2O$ and pure $EtNH_2$ (BDH, >99.5%) was carried out by mixing the two components and leaving them in a sealed flask for 24 h, with occasional stirring. Because of the volatility of $EtNH_2$ the flask was placed in an ice bath. Although the product of this reaction was found to be stable in air and able to be characterised, the product of a similar reaction with $BuNH_2$ had a paste-like appearance and on removal from the liquid amine appeared to become more fluid, presumably due to the loss of $BuNH_2$. Subsequent reactions were carried out using solutions of the amines in toluene. This solvent was chosen due to its inertness: approximately 0.5 g of $MoO_2HPO_4.H_2O$ was stirred in 100 cm^3 of toluene (May & Baker, Lab. Reag.) for 24 h and then filtered off. The powder x-ray diffraction spectrum of the white powder so obtained was identical with that of the starting material. By contrast $MoO_2HPO_4.H_2O$ takes up water readily, even by prolonged contact with the air, eventually becoming an amorphous white paste.

Solutions of 0.050 and 0.102M $PrNH_2$ (BDH, >98%) and 0.051, 0.101, 0.202 and 0.417M $BuNH_2$ (BDH, >98%) in toluene were made up. Their concentrations were determined by titration against a solution of perchloric acid (BDH, AnalaR) in glacial acetic acid (May & Baker, Lab. Reag.) using crystal violet indicator, as described in Vogel[9]. The 0.1015M $HClO_4$ solution was itself first standardised against a solution of potassium hydrogen phthalate (Aldrich, >99.95%).

The intercalation reactions were effected by continuous stirring of approximately 0.5 g of dry, finely ground $MoO_2HPO_4.H_2O$ with 100 cm^3 of amine solution in a sealed flask at room temperature. At first reactions were allowed to continue for 24 h but subsequently the period was extended to 5 days. The products were filtered off, pumped on briefly under the suction of a water pump and then weighed. They took the form of white powders.

The intercalates were characterised by powder x-ray diffraction and infrared spectroscopy. To obtain approximate values for the amounts of intercalant taken up, measurement of the weight increase of the samples yielded fairly consistent results, although it was not possible to distinguish between the weight increase due to true intercalation and that which may have been due to physisorption. Attempts to determine by titration the amount of unreacted amine left in the solution gave results much lower than expected, presumably due to evaporation of amine during the filtering process, and this method was discontinued at an early stage of the study.

6.7 Results & Discussion

Uptake of Intercalant

Weight increase was assumed to be entirely due to intercalation or adsorption of pure amine, and the starting material was assumed to be a pure phase of

$MoO_2HPO_4.H_2O$. For each reaction, a figure could thus be obtained corresponding to the number of moles of amine taken up for each mole of $MoO_2HPO_4.H_2O$.

For the direct reaction with $EtNH_2$, it was found using molar excesses of intercalant in the range 6:1 to 60:1, that between 2.7 and 3.2 moles were taken up, with no relation between the proportion of the reactants and uptake. For $PrNH_2$ and $BuNH_2$, the molar uptakes for the various strengths of solution are tabulated in table 6.4. It is evident from the relative values that a correlation exists between the strength of solution and the amount of intercalant taken up. The results also give an indication of the timescale of intercalation, since after 24 h the reactions appear not to have progressed as far as at 5 days.

Infrared Spectroscopy

The infrared spectrum of an $EtNH_2$ reaction product is shown in figure 6.4. It can be seen that a a number of features of the the parent compound (see chapter 3) are retained, in particular the framework P–O bands at 1105, 1046, 995 and 901 cm^{-1}. Strong features are also observed at *ca.* 680 and *ca.* 550 cm^{-1}. At higher frequency, absorptions due to the intercalant are observed, with a series of lines between 1580 and 1450 cm^{-1} and two sharp bands at 1398 and 1262 cm^{-1} assigned to C–H deformations, although the 1262 cm^{-1} band may instead be C–N stretching mode. N–H stretching bands are observed at 3308 and 3225 cm^{-1} and C–H at 2925 and 2850 cm^{-1}. It is apparent that H_2O is still present in the product, with a strong band at *ca.* 1625 cm^{-1} and a very broad feature in the O–H stretching region between 2800 and 3400 cm^{-1} indicating substantial hydrogen bonding. The sharp O–H stretches observed in $MoO_2HPO_4.H_2O$ are not resolved here.

Table 6.4 Measured Uptake of Intercalant in Reactions Between $MoO_2HPO_4.H_2O$ and Various Solutions of Amine in Toluene

(in mol/mol $MoO_2HPO_4.H_2O$)

Intercalant & Solution Strength /mol.dm^3		Reaction Time 24 h	5 days
$PrNH_2$	0.05	-	2.6
	0.10	-	2.9
$BuNH_2$	0.05	-	2.1
	0.10	1.9	2.4
	0.20	-	2.7
	0.42	2.5	-

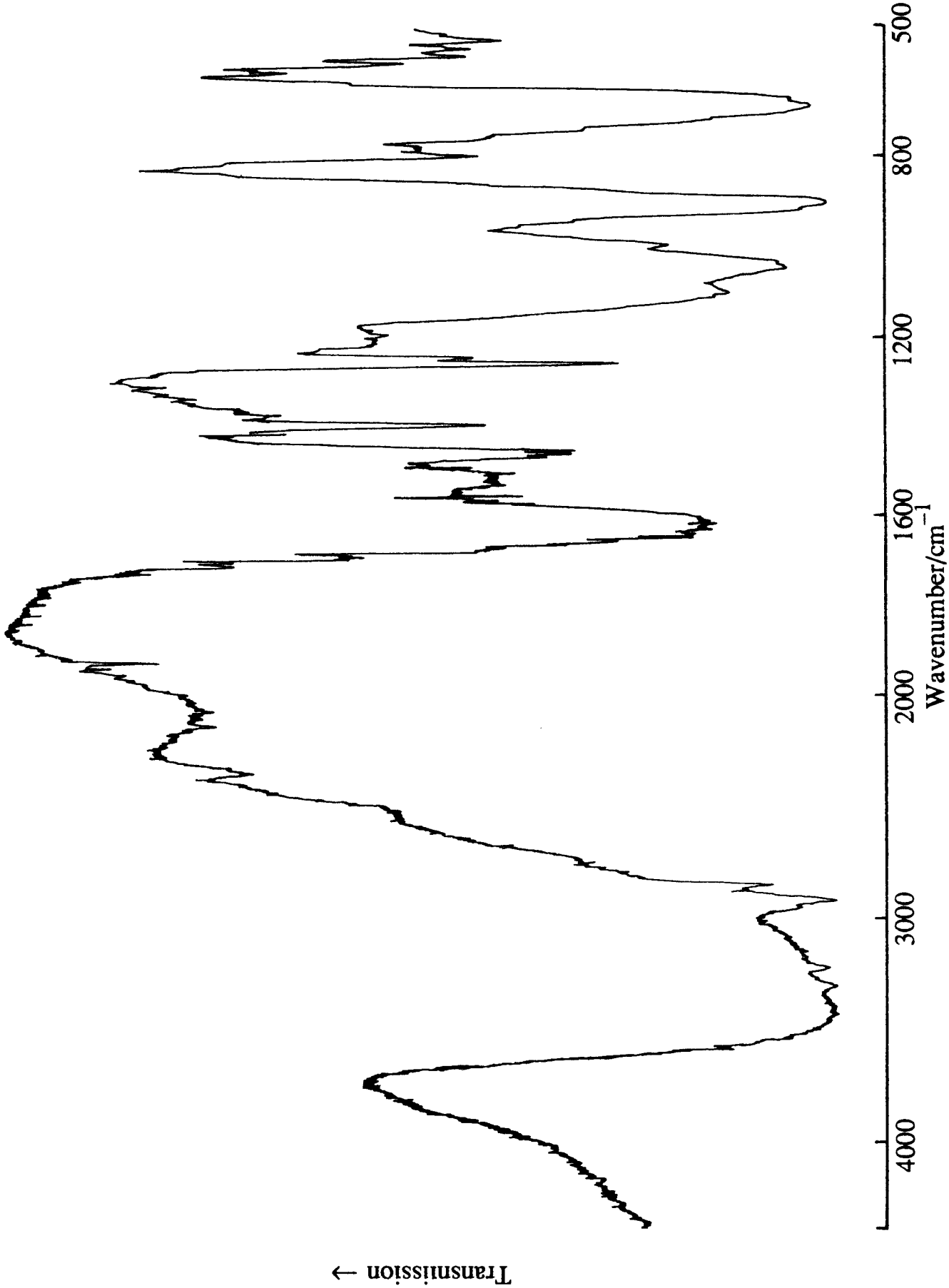

Figure 6.4 Infrared spectrum of an intercalation product of $MoO_2HPO_4.H_2O$ with ethylamine.

X-Ray Diffraction

The powder x-ray data for all the reaction products were highly complex. The large numbers of diffraction peaks observed, greater than 100 in some cases, indicated either that the products had very large unit cells or that they consisted of a mixture of crystalline phases. Among intercalates of the same amine there was however a good deal of consistency between the patterns. In particular for the $PrNH_2$ intercalates, a strong reflection was always observed at approximately 13.95° (d spacing 6.34 Å), which corresponds to the repeat distance along the molybdenyl phosphate chains. It should be noted that for $MoO_2HPO_4.H_2O$ itself this reflection is not observed since the 2_1 screw axis along *y* causes the extinction of *0k0* reflections where *k* is odd. This element of symmetry is therefore lost in the $PrNH_2$ intercalates. The $BuNH_2$ compounds also did not exhibit this feature, but instead all had a strong peak at *ca.* 22.9° (d spacing 3.88 Å). If this is taken to correspond with half the repeat distance along the framework chains, then some considerable distortion must take place on intercalation of $BuNH_2$ since it represents an increase of some 0.7 Å over the corresponding distance in pure $MoO_2HPO_4.H_2O$.

Attempts were made to index the patterns, both manually and using the Visser autoindexing program. It became apparent that none could be totally indexed on the basis of a single crystalline phase and that in each case a mixture of phases was present. For the $EtNH_2$ intercalate the best fit was obtained with a monoclinic cell of dimensions

$$a=23.895(6)\ \text{Å},\ b=12.002(3)\ \text{Å},\ c=6.623(2)\ \text{Å and}\ \beta=110.69(1)°.$$

44 of the observed 84 peaks in the chosen diffraction pattern could be indexed using this cell, as shown in table 6.5. It can be seen that the *c* parameter is some 0.25 Å

Table 6.5 Observed and Calculated Powder Diffraction Data for $MoO_2HPO_4.H_2O.xC_2H_5NH_2$

h k l	*2θ(obs)*	*2θ(calc)*	*h k l*	*2θ(obs)*	*2θ(calc)*
1 0 -1	13.36	13.40	2 5 -1	40.06	40.03
2 0 -1	13.63	13.66	10 0 0	40.33	40.31
0 0 1	14.28	14.28	7 3 1	42.56	42.59
0 2 0	14.75	14.75	7 0 -3	42.91	42.90
0 1 1	16.09	16.08	1 1 3	46.14	46.13
1 1 1	17.76	17.74	7 4 1	47.27	47.27
5 0 -1	19.94	19.95	10 0 -3	48.24	48.24
5 1 -1	21.31	21.29	9 4 -2	48.59	48.61
1 2 1	21.90	21.92	8 3 -3	50.13	50.13
2 3 0	23.57	23.60	11 0 -3	50.62	50.64
6 1 0	24.98	25.00	8 0 2	51.13	51.13
3 2 1	26.32	26.28	7 4 -3	53.07	53.07
5 0 -2	28.67	28.65	8 5 1	55.76	55.76
5 3 0	29.98	29.95	13 4 -2	59.96	59.96
6 0 -2	30.33	30.29	10 5 1	62.30	62.28
3 4 0	32.13	32.13	1 3 -4	63.05	63.05
5 2 -2	32.40	32.37	7 6 -3	64.15	64.15
7 3 -1	34.82	34.82	16 2 -2	64.58	64.58
6 2 1	35.48	35.48	9 7 0	66.18	66.17
4 0 2	37.83	37.82	10 4 2	67.28	67.29
9 1 -2	38.31	38.30	1 7 -3	70.49	70.49
7 3 -2	39.57	39.59	5 5 3	68.54	68.55

λ=1.5406 Å

a=23.895(6) Å, b=12.002(3) Å, c=6.623(2) Å, β=110.69(1)°

greater than the *b* parameter for pure $MoO_2HPO_4.H_2O$, and may represent the repeat distance of the framework chain, which has therefore become "stretched" in the intercalation compound.

In the case of most lamellar intercalates it is relatively easy to relate the increase in a single lattice parameter to the size and orientation of the intercalant molecules, particularly for linear chain organic compounds. In the present case the problem is more complex since effectively only one dimension is invariant. A simple approach is to consider the increase in volume due to intercalation. In the work of Jacobson et al.[10] intercalation of a series of *n*–alkylamines into the perovskite-like $HCa_2Nb_3O_{10}$ is reported. From the full lattice parameters and stoichiometries given for these intercalates, it is possible to derive effective volumes for the various amine molecules. On this basis the volume of an $EtNH_2$ molecule is 83 $Å^3$. The volume of the unit cell given above is 1777 $Å^3$, and that of a formula unit of $MoO_2HPO_4.H_2O$ (half the unit cell of the pure phase) 143 $Å^3$. A possible interpretation of this is to assume that there are eight formula units in the unit cell of the intercalate. The increase in volume then becomes 79 $Å^3$ per $MoO_2HPO_4.H_2O$ unit, i.e. very close to one $EtNH_2$ molecule. It could thus well be that the phase identified by x-ray diffraction has a stoichiometry close to $MoO_2HPO_4.H_2O.C_2H_5NH_2$, and that the observed weight increase was caused either by surface-adsorption or by the formation of other, more amine-rich phases.

Unfortunately it was not possible to index the patterns for the $PrNH_2$ and $BuNH_2$ intercalates, due to the probable presence of more than one phase and the likelihood that primitive unit cells even larger than than observed for the $EtNH_2$ compound are present.

6.8 Conclusion

Very recent work by Gilson and Weller[11] reports the intercalation into $MoO_2HPO_4.H_2O$ of a range of small organic species including methanol, ethanol and isopropanol. The reactions were carried out by equilibration of the solid with the vapour above the liquid intercalant. 1:1 stoichiometries were found for the isopropanol and methanol intercalates, the latter after further equilibration with the air. X-ray diffraction showed single-phase products, and in the case of the methanol intercalate enabled a structure to be proposed.

In the present work the greater success in characterising the ethylamine intercalate suggests that larger molecules present too complex a problem in studying intercalation into a chain-structured compound. It may in fact be that replacement of H_2O, rather than true intercalation, was taking place. Further work by Gilson and Weller[12] on the reaction of $MoO_2HPO_4.H_2O$ with dimethyl sulphoxide showed that replacement of water had taken place, thus altering the framework structure and making characterisation of the product difficult. In this work the x-ray diffraction results and infrared spectrum, in which many features of $MoO_2HPO_4.H_2O$ were retained, suggest however that this has not taken place in the case of the $EtNH_2$ compound.

The method of intercalation by using a solution in toluene has not yet been proven to be successful. However it may be that much longer reaction times are needed to produce homogeneous products, as in the case of the isopropanol intercalate reported by Gilson and Weller[11] which was equilibrated for three months. Further work on intercalation with the alkylamines would include longer reaction times, both in solution and, in the case of the lighter intercalates, by equlibration with vapour. Both thermogravimetric and elemental analysis should be available to study the intercalates, in order to determine the true stoichiometries of the phases.

CHAPTER 1 REFERENCES

(1) A.F.Wells, *Structural Inorganic Chemistry*, 5th ed., O.U.P., (1984).

(2) J.Hutton & R.J.Nelmes, *J. Phys. C*, **14**, 1713, (1981).

(3) P.G.Dickens & M.T.Weller, *Solid State Comm.*, **59**, 569, (1986).

(4) P.Spiegelberg, *Ark. Kemi*, **14A**, 1, (1940).

(5) S.Andersson & A.D.Wadsley, *Acta Chem. Scand.*, **15**, 663, (1961).

(6) A.D.Wadsley, *Acta Cryst.*, **17**, 623, (1964).

(7) R.B.Roof, D.T.Cromer & A.C.Larson, *Acta Cryst.*, **17**, 701, (1964).

(8) M.Seleborg, *Acta Chem. Scand.*, **20**, 2195, (1966).

(9) B.M.Gatehouse & P.Leverett, *J. Chem. Soc. A*, 1398, (1968).

(10) Y.Piffard, A.Lachgar & M.Tournoux, *Mat. Res. Bull.*, **20**, 715, (1985).

(11) Y.Piffard, A.Lachgar & M.Tournoux, *Mat. Res. Bull.*, **21**, 1221, (1986).

(12) Y.Piffard, S.Oyetola, S.Courant & A.Lachgar, *J. Solid State Chem.*, **60**, 209, (1985).

(13) Y.Piffard, A.Lachgar & M.Tournoux, *J. Solid State Chem.*, **58**, 253, (1985).

(14) A.Lachgar, S.Deniard-Courant & Y.Piffard, *J. Solid State Chem.*, **63**, 409, (1986).

(15) P.Kierkegaard, *Ark. Kemi*, **18**, 553, (1962).

(16) A.Leclaire, J.-C.Monier & B.Raveau, *J. Solid State Chem.*, **48**, 147, (1983).

(17) A.Leclaire, J.-C.Monier & B.Raveau, *J. Solid State Chem.*, **59**, 301, (1985).

(18) B.Morosin, *Acta Cryst. B*, **34**, 3738, (1978).

(19) A.Clearfield & G.D.Smith, *Inorg. Chem.*, **8**, 431, (1969).

(20) N.Kumada, O.Horiuchi, F.Muto & N.Kinomura, *Mat. Res. Bull.*, **23**, 209, (1988).

(21) L.Glasser, *Chem. Rev.*, **75**, 21, (1975).

(22) F.W.Poulsen in *High Conductivity Solid Ionic Conductors* (T.Takahashi ed.), World Publishing Co., Singapore, (1988).

(23) G.Alberti, M.Casciola & U.Constantino in *Solid State Proton Conductors III* (J.B.Goodenough, J.Jensen & A.Potier eds.), Odense University Press, (1985).

(24) P.Colomban & A.Novak, *J. Mol. Struct.*, **177**, 277, (1988).

(25) U.Chowdhry, J.R.Barkley, A.D.English & A.W.Sleight, *Mat. Res. Bull.*, **17**, 917, (1982).

(26) A.N.Fitch, A.F.Wright & B.E.F.Fender, *Acta Cryst. B*, **38**, 2546, (1982).

(27) A.N.Fitch, L.Bernard, A.T.Howe, A.F.Wright & B.E.F.Fender, *Acta Cryst. C*, **39**, 159, (1983).

(28) C.J.T. von Grotthus, *Ann. Chim.*, **58**, 54, (1806).

(29) M.G.Shilton & A.T.Howe, *Mat. Res. Bull.*, **12**, 701, (1978).

(30) P.E.Childs, T.K.Halstead, A.T.Howe & M.G.Shilton, *Mat. Res. Bull.*, **13**, 609, (1978).

(31) C.M.Johnson, M.G.Shilton & A.T.Howe, *J. Solid State Chem.*, **37**, 37, (1981).

(32) R.C.T.Slade in *Solid State Proton Conductors III* (J.B.Goodenough, J.Jensen & A.Potier eds.), Odense University Press, (1985).

(33) R.A.Huggins in *Diffusion in Solids* (A.S.Nowick & J.J.Burton eds.), Academic Press, New York, (1975).

(34) M.Bée, *Quasielastic Neutron Scattering: Principles and Applications in Solid State Chemistry, Biology and Materials Science*, Adam Hilger, Bristol, (1988).

(35) B.T.M.Willis ed., *Chemical Applications of Thermal Neutron Scattering*, O.U.P., (1973).

(36) C.T.Chudley & R.J.Elliott, *Proc. Phys. Soc.*, **77**, 353, (1960).

(37) M.S.Whittingham & A.J.Jacobson eds., *Intercalation Chemistry*, Academic Press, New York, (1982).

(38) M.S.Dresselhaus & G.Dresselhaus, *Adv. Phys.*, **30**, 139, (1981).

(39) J.M.Thomas in ref. (37).

(40) E.Michel & A.Weiss, *Z. Naturforsch. B*, **20**, 1307, (1965).

(41) A.Clearfield & R.M.Tindwa, *J. Inorg. Nucl. Chem.*, **41**, 871, (1979).

(42) M.Casciola, U.Constantino & F.Marmottini, *Solid State Ionics*, **35**, 67, (1989).

(43) U.Constantino, *J.C.S. Dalton Trans.*, 402, (1979).

(44) L.Moreno Real, R.Pozas Tormo, N.Martinez Lara & S.Bruque, *Mat. Res. Bull.*, **22**, 19, (1987).

CHAPTER 2 REFERENCES

(1) K.Yvon, W.Jeitshko & E.Parthé, *J. Appl. Cryst.*, **10**, 73, (1977).

(2) J.W.Visser, *J. Appl. Cryst.*, **2**, 89, (1969).

(3) W.I.Archer & R.D.Armstrong, *Spec. Period. Rep. Electrochem.*, **7**, 157, Chem. Soc., London, (1978).

(4) I.D.Raistrick, *Ann. Rev. Mater. Sci.*, **16**, 343, (1986).

(5) M.J.Buerger, *Contemporary Crystallography*, McGraw-Hill, New York, (1970).

(6) B.T.M.Willis & A.W.Pryor, *Thermal Vibrations in Crystallography*, C.U.P, (1975).

(7) G.E.Bacon, *Neutron Diffraction*, O.U.P, (1962).

(8) *Neutron Research Facilities at the I.L.L. High Flux Reactor*, Scientific Co-ordination and Public Relations Office, I.L.L., Grenoble, (1986).

(9) H.M.Rietveld, *J. Appl. Cryst.*, **3**, 65, (1969).

(10) M.Bée, *Quasielastic Neutron Scattering: Principles and Applications in Solid State Chemistry, Biology and Materials Science*, Adam Hilger, Bristol, (1988).

CHAPTER 3 REFERENCES

(1) I.Schulz, *Z. Anorg. Allg. Chem.*, **281**, 99, (1955).

(2) P.Kierkegaard, *Acta Chem. Scand.*, **12**, 1701, (1958).

(3) P.Kierkegaard, *Ark. Kemi*, **19**, 51, (1962).

(4) L.R.Florian & E.R.Corey, *Inorg. Chem.*, **7**, 722, (1968).

(5) N.J.Clayden, *J.C.S. Dalton Trans.*, 1877, (1987).

(6) E.R.Lippincott & R.Schroeder, *J. Chem. Phys.*, **23**, 1099, (1955).

(7) M.G.Shilton & A.T.Howe, *Mat. Res. Bull.*, **12**, 701, (1978).

CHAPTER 4 REFERENCES

(1) U.Chowdhry, J.R.Barkley, A.D.English & A.W.Sleight, *Mat. Res. Bull.*, **17**, 917, (1982).

(2) H.Watelet, J.-P.Picard, G.Baud, J.-P.Besse & R.Chevalier , *Mat. Res. Bull.*, **16**, 1131, (1981).

(3) P.G.Dickens & M.T.Weller, *Solid State Comm.*, **59**, 569, (1986).

(4) D.Groult, J.Pannetier & B.Raveau, *J. Solid State Chem.*, **41**, 277, (1982).

(5) P.Spiegelberg, *Ark. Kemi*, **14A**, 1, (1940).

(6) K.Nakamoto, *Infrared and Raman Spectra of Inorganic and Coordination Compounds*, 3rd ed., Wiley-Interscience, New York, (1978).

(7) I.D.Brown & K.K.Wu, *Acta Cryst. B*, **32**, 1957, (1976).

CHAPTER 5 REFERENCES

(1) M.Bée, *Quasielastic Neutron Scattering: Principles and Applications in Solid State Chemistry, Biology and Materials Science*, Adam Hilger, Bristol, (1988).

(2) B.T.M.Willis ed., *Chemical Applications of Thermal Neutron Scattering*, O.U.P., (1973).

(3) T.Springer in *Dynamics of Solids and Liquids by Neutron Scattering* (S.W.Lovesey & T.Springer eds.), Springer-Verlag, Berlin, (1977).

(4) C.T.Chudley & R.J.Elliott, *Proc. Phys. Soc.*, **77**, 353, (1960).

(5) W.L.Roth, M.Anne, D.Tranqui & A.Heidemann, *Fast Ion Transport in Solids* (P.Vashishta, J.N.Mundy & G.K.Shenoy eds.), 267, Elsevier North Holland, New York, (1979).

(6) C.Poinsignon, A.N.Fitch & B.E.F.Fender, *Solid State Ionics*, **9/10**, 1049, (1983).

(7) C.Poinsignon, *Solid State Ionics*, **35**, 107, (1989).

(8) H.A.Pressman & R.C.T.Slade, *Chem. Phys. Lett.*, **151**, 354, (1988).

(9) H.Watelet, J.-P.Picard, G.Baud, J.-P.Besse & R.Chevalier , *Mat. Res. Bull.*, **16**, 1131, (1981).

(10) U.Chowdhry, J.R.Barkley, A.D.English & A.W.Sleight, *Mat. Res. Bull.*, **17**, 917, (1982).

(11) A.Deschanvres, C.Michel & B.Raveau, *Bull. Soc. Chim. France*, 4805, (1968).

(12) B.Raveau & J.-C.Thomazeau, *C.R. Acad. Sci. Paris*, **266C**, 540, (1968).

(13) M.Hervieu, C.Michel & B.Raveau, *Bull. Soc. Chim. France*, 3939, (1971).

(14) P.G.Dickens & M.T.Weller, *Solid State Comm.*, **59**, 569, (1986).

(15) D.Groult, J.Pannetier & B.Raveau, *J. Solid State Chem.*, **41**, 277, (1982).

(16) B.Darriet, M.Rat, J.Galy & P.Hagenmuller, *Mat. Res. Bull.*, **6**, 1305, (1971).

(17) M.A.Butler & R.M.Biefeld, *Phys. Rev. B*, **19**, 5455, (1979).

(18) M.Kuntz, G.Tomandl & A.Hoser, *Solid State Ionics*, **25**, 121, (1987).

(19) M.A.Butler & R.M.Biefeld, *Solid State Comm.*, **29**, 5, (1979).

(20) A.R.Vogel, *Textbook of Quantitative Inorganic Analysis*, 4th ed., Longman, London, (1978).

(21) M.Anne & I.S.Anderson, *WLI: A Data Fitting Program*, I.L.L. Internal Report No. 85AN7T, I.L.L., Grenoble, (1985).

CHAPTER 6 REFERENCES

(1) Y.Piffard, A.Verbaere, A.Lachgar, S.Deniard-Courant & M.Tournoux, *Rev. Chim. Min.*, **23**, 766, (1986).

(2) H.Arribart & Y.Piffard, *Solid State Comm.*, **45**, 571, (1983).

(3) A.Winkler & E.Thilo, *Z. Anorg. Allg. Chem.*, **346**, 92,(1966).

(4) Y.Piffard, A.Lachgar & M.Tournoux, *Mat. Res. Bull.*, **20**, ,(1985).

(5) E.Husson, F.Genet, A.Lachgar & Y.Piffard, *J. Solid State Chem.*, **75**, 305, (1988).

(6) F.Taulelle, C.Sanchez, J.Livage, A.Lachgar & Y.Piffard, *J. Phys. Chem. Solids*, **49**, 299, (1988).

(7) Y.Piffard, S.Oyetola, S.Courant & A.Lachgar, *J. Solid State Chem.*, **60**, (1985).

(8) S.Deniard-Courant, Y.Piffard, P.Barboux & J.Livage, *Solid State Ionics*, **27**, 189, (1988).

(9) A.R.Vogel, *Elementary Practical Organic Chemistry*, Longmans, London, (1958).

(10) A.J.Jacobson, J.W.Johnson & J.T.Lewandowski, *Mat. Res.Bull*, **22**, 45, (1987).

(11) T.R.Gilson & M.T.Weller, *Inorg. Chem.*, **28**, 4059, (1989).

(11) T.R.Gilson & M.T.Weller, unpublished results.

APPENDIX I

Observed and Calculated Neutron Diffraction Intensities for $MoO_2DPO_4.D_2O$

h k l	2θ *(calc)*	I_{hkl} *(calc)*	I_{hkl} *(obs)*	*h k l*	2θ *(calc)*	I_{hkl} *(calc)*	I_{hkl} *(obs)*
1 1 -2	30.66	24	33	3 0 -3	50.57	118	133
2 1 -1	31.48	26914	27130	1 3 1	50.72	174	283
0 1 2	31.75	14442	14861	3 0 1	51.66	1075	1137
0 2 1	32.44	301	539	3 2 -1	51.75	2508	2579
1 2 0	32.70	384	441	1 1 3	52.52	13098	13330
2 1 0	32.81	14456	14607	0 2 3	52.54	638	652
2 0 -2	33.10	362	326	1 3 -2	52.60	148	153
1 2 -1	33.60	2578	2254	2 2 -3	52.72	706	730
1 0 2	36.07	624	0	3 1 -3	52.88	540	541
2 1 -2	36.28	5634	4168	2 3 -1	53.13	9840	9812
2 0 1	36.79	2365	0	0 3 2	53.30	11294	11487
1 2 1	37.71	1090	1039	3 2 -2	53.60	11798	11785
1 1 2	39.04	1665	1482	3 1 1	53.94	3096	3224
2 1 1	39.71	6800	7138	2 3 0	54.01	62	65
1 2 -2	40.06	25123	24622	3 2 0	54.13	638	682
1 0 -3	40.06	365	357	1 0 -4	54.55	11200	11516
2 2 -1	40.71	437	468	2 0 -4	55.41	1563	2362
0 2 2	40.92	62	30	2 3 -2	56.41	112	67
2 2 0	41.78	211	215	1 1 -4	56.75	133	142
3 0 -1	41.79	3410	3539	2 2 2	57.02	1501	1461
0 0 3	42.72	2953	3215	4 0 -1	57.12	3486	3425
1 1 -3	42.80	0	0	4 0 -2	57.46	284	269
2 0 -3	42.93	1993	1962	2 1 -4	57.59	1496	1374
3 0 -2	43.96	25899	25803	0 0 4	58.10	374	450
3 1 -1	44.44	5537	5382	1 3 2	58.41	1116	1217
3 0 0	44.57	9824	9448	2 3 1	58.91	47	64
2 2 -2	44.66	368	352	1 2 3	59.09	237	302
0 1 3	45.33	3514	2104	4 1 -1	59.25	475	510
2 1 -3	45.53	727	370	3 2 -3	59.42	3987	3944
3 1 -2	46.51	7211	7288	4 1 -2	59.58	8	8
0 3 1	46.69	8278	8505	0 1 4	60.21	2030	2003
1 3 0	46.88	31	33	0 4 0	60.38	18008	18225
1 2 2	47.01	310	335	3 2 1	60.40	288	292
3 1 0	47.10	565	611	3 0 -4	60.56	1539	1572
1 3 -1	47.55	15670	15503	4 0 0	60.74	318	339
2 2 1	47.59	7939	7873	2 0 3	61.21	40	44
2 0 2	47.88	1543	1734	1 3 -3	61.25	3524	3744
1 0 3	50.20	5600	5896	4 0 -3	61.70	1868	1859
2 1 2	50.27	204	210	3 0 2	62.01	3370	3618
1 2 -3	50.29	422	434	0 4 1	62.31	1	1

h k l	2θ *(calc)*	I_{hkl} *(calc)*	I_{hkl} *(obs)*	*h k l*	2θ *(calc)*	I_{hkl} *(calc)*	I_{hkl} *(obs)*
1 4 0	62.47	130	131	3 0 -5	73.21	5146	5591
3 3 -1	62.54	10758	10782	1 2 4	73.35	601	899
3 1 -4	62.62	8299	8367	2 3 -4	73.55	145	651
4 1 0	62.79	1734	1774	5 0 -1	73.96	13	228
1 4 -1	63.02	89	91	0 0 5	74.74	7	0
1 2 -4	63.03	2273	2309	5 1 -2	74.89	1	0
0 3 3	63.24	6000	6025	1 4 -3	74.94	100	53
2 1 3	63.25	3173	3185	3 0 3	74.97	461	302
2 3 -3	63.40	0	0	4 3 -1	75.02	55	46
4 1 -3	63.73	1463	1496	3 1 -5	75.09	6268	6171
2 2 -4	63.82	225	230	4 3 -2	75.31	233	277
3 1 2	64.05	1850	1890	4 2 1	75.55	1460	1734
3 3 -2	64.19	7112	7237	5 0 -3	75.56	278	329
3 3 0	64.66	709	588	5 1 -1	75.84	105	105
4 2 -1	65.39	310	274	0 3 4	75.88	7642	7371
1 0 4	65.61	5564	4667	3 4 -1	76.12	216	158
1 4 1	65.67	19	15	2 0 4	76.49	380	246
4 2 -2	65.70	741	577	0 1 5	76.61	1186	929
0 2 4	66.30	198	243	0 4 3	76.76	27	26
2 3 2	67.27	2	3	3 1 3	76.84	2104	2238
1 4 -2	67.28	2558	2992	2 4 -3	76.90	45	50
1 1 4	67.58	1251	1131	4 2 -4	77.00	2601	2990
2 4 -1	67.74	4	4	2 2 -5	77.42	818	878
0 4 2	67.89	677	633	5 1 -3	77.42	1534	1645
4 0 1	67.92	7622	7190	3 4 -2	77.63	8047	8104
2 4 0	68.50	1862	2060	1 2 -5	77.92	89	86
3 2 -4	68.59	883	968	3 3 -4	78.05	13796	13767
4 2 0	68.75	922	964	3 4 0	78.06	468	469
1 3 3	69.16	12344	11811	4 3 0	78.20	340	347
2 2 3	69.19	754	723	4 0 2	78.23	3606	3687
4 0 -4	69.43	29	30	2 1 4	78.34	3669	3729
3 3 -3	69.47	273	282	5 0 0	78.38	73	73
4 2 -3	69.65	840	888	2 3 3	78.62	9541	9482
4 1 1	69.86	561	561	4 3 -3	79.06	5311	5301
2 0 -5	69.87	6	6	3 3 2	79.34	4354	4254
3 2 2	69.95	1164	1124	0 5 1	79.61	29	30
3 3 1	70.37	170	203	1 5 0	79.75	1917	2008
1 0 -5	70.39	1097	1342	4 1 2	80.07	1340	1362
2 4 -2	70.60	92	151	5 1 0	80.22	7837	7865
4 1 -4	71.35	2821	2926	4 0 -5	80.23	5608	5626
2 1 -5	71.78	666	703	1 5 -1	80.25	1478	1480
1 1 -5	72.30	1	1	5 2 -2	80.45	2643	2625
1 4 2	72.38	160	144	2 4 2	80.49	17	17
1 3 -4	72.81	368	383	3 2 -5	80.65	770	778
2 4 1	72.83	1760	1836	5 2 -1	81.38	2092	1982
5 0 -2	73.01	2371	2457	5 0 -4	81.52	317	348

h k l	2θ *(calc)*	I_{hkl} *(calc)*	I_{hkl} *(obs)*	*h k l*	2θ *(calc)*	I_{hkl} *(calc)*	I_{hkl} *(obs)*
4 1 -5	82.06	3024	3192	5 0 -5	90.76	158	158
0 2 5	82.13	4140	4246	3 4 -4	90.81	1657	1627
1 4 3	82.27	193	193	4 4 0	90.96	972	915
3 2 3	82.36	8585	8678	6 0 -2	90.99	906	848
3 4 -3	82.56	737	778	0 3 5	91.21	0	0
1 3 4	82.61	3	3	2 4 3	91.37	0	0
1 5 1	82.67	451	481	1 5 -3	91.41	297	287
1 0 5	82.71	535	569	3 3 3	91.43	896	865
5 2 -3	82.94	1035	1047	4 0 3	91.54	935	896
5 1 -4	83.35	566	622	4 4 -3	91.80	618	577
3 4 1	83.41	2	3	5 3 -3	92.01	310	308
2 2 4	83.84	6897	7045	3 4 2	92.08	605	623
1 5 -2	84.16	355	345	6 0 -3	92.25	30	33
1 1 5	84.53	877	824	3 1 4	92.36	1551	1682
2 5 -1	84.58	1359	1273	3 5 -1	92.54	350	360
0 5 2	84.72	215	200	5 1 -5	92.57	4273	4348
4 3 1	84.75	369	342	6 1 -2	92.80	458	445
2 5 0	85.29	1559	1677	2 3 4	92.91	198	193
4 2 2	85.55	1587	1629	6 0 -1	93.10	1318	1306
5 2 0	85.70	1381	1367	0 5 3	93.17	1539	1532
1 4 -4	85.73	2406	2361	2 5 -3	93.31	959	955
5 0 1	86.13	413	388	4 1 3	93.35	1509	1499
4 3 -4	86.16	865	819	5 2 1	93.37	328	325
2 4 -4	86.44	156	158	0 0 6	93.49	1643	1605
2 0 -6	86.45	2	2	2 2 -6	93.70	3355	3221
2 3 -5	86.57	5155	5196	3 5 -2	94.02	757	768
1 3 -5	87.06	1009	949	4 0 -6	94.06	1754	1794
2 5 -2	87.26	2365	2283	6 1 -3	94.07	699	716
4 2 -5	87.52	4295	4348	2 0 5	94.20	2504	2612
4 4 -1	87.86	1668	1793	3 5 0	94.45	29	30
5 1 1	87.94	504	549	4 3 2	94.61	4798	4831
1 0 -6	88.14	489	541	5 3 0	94.76	1210	1201
4 4 -2	88.14	51	56	6 1 -1	94.92	8179	8042
2 1 -6	88.26	161	175	0 1 6	95.30	184	177
3 0 -6	88.43	1232	1274	1 4 4	95.31	2092	2017
0 4 4	88.69	2	2	1 2 -6	95.39	2550	2454
5 2 -4	88.79	2196	2183	3 2 -6	95.68	596	583
1 5 2	88.95	1174	1193	4 1 -6	95.88	628	639
2 5 1	89.37	1652	1562	2 1 5	96.02	1447	1517
5 3 -2	89.55	1396	1297	4 3 -5	96.58	5183	5121
3 3 -5	89.74	2536	2405	2 5 2	96.85	8	8
1 1 -6	89.95	4102	4063	6 0 -4	96.91	1598	1652
1 2 5	89.97	1001	995	5 0 2	97.19	12	14
3 1 -6	90.24	2130	2271	4 4 1	97.45	1027	1029
5 3 -1	90.46	497	543	3 2 4	97.81	338	333
3 0 4	90.54	802	863	5 3 -4	97.87	197	198

h k l	2θ *(calc)*	I_{hkl} *(calc)*	I_{hkl} *(obs)*	*h k l*	2θ *(calc)*	I_{hkl} *(calc)*	I_{hkl} *(obs)*
0 6 0	97.91	7888	8058	6 0 -5	105.08	91	87
5 2 -5	98.03	21	23	0 5 4	105.16	5	5
6 2 -2	98.26	10	12	5 1 -6	105.34	372	350
1 5 3	98.62	1022	1168	2 6 0	105.39	2190	2057
6 0 0	98.62	1764	2014	2 4 4	105.77	2977	2722
6 1 -4	98.74	304	324	6 2 0	106.03	139	136
4 2 3	98.81	17	17	2 0 -7	106.22	619	657
4 4 -4	98.87	612	624	6 1 -5	106.96	2699	2734
3 5 -3	98.91	242	246	3 0 -7	107.03	1198	1206
5 1 2	99.02	840	878	3 3 4	107.09	513	514
1 3 5	99.06	963	1025	5 3 -5	107.31	627	616
2 4 -5	99.28	197	241	3 5 -4	107.36	1605	1569
6 2 -3	99.54	825	1096	2 6 -2	107.44	88	86
0 6 1	99.62	82	109	4 5 0	107.52	956	922
1 6 0	99.76	4	6	4 4 2	107.55	3576	3443
3 5 1	99.76	665	875	6 3 -2	107.55	699	673
1 4 -5	99.78	21	28	5 4 0	107.70	71	68
1 6 -1	100.26	2	2	6 0 1	107.73	33	32
6 2 -1	100.40	1576	1543	2 5 3	107.95	351	349
6 1 0	100.45	501	478	2 1 -7	108.11	198	204
0 2 6	100.79	1	1	4 3 3	108.13	5139	5301
4 2 -6	101.37	515	245	4 5 -3	108.40	91	98
2 2 5	101.51	30	24	4 0 4	108.45	1094	1179
1 5 -4	102.12	0	0	3 5 2	108.70	86	88
5 4 -2	102.31	3764	7285	6 3 -3	108.88	2321	2226
3 4 -5	102.51	1189	1050	3 1 -7	108.93	100	95
5 3 1	102.52	3397	2998	1 6 2	109.22	329	308
1 0 6	102.59	4304	3810	1 0 -7	109.24	3482	3271
1 6 1	102.70	426	374	4 4 -5	109.62	1718	1745
2 5 -4	102.84	270	237	6 1 1	109.64	4713	4794
2 3 -6	102.85	30	26	2 6 1	109.67	13	14
5 4 -1	103.25	596	550	3 0 5	109.71	79	81
5 0 -6	103.47	86	88	6 3 -1	109.78	1528	1556
0 4 5	104.02	797	884	1 2 6	110.14	228	238
1 6 -2	104.22	1	1	0 3 6	110.19	2505	2632
3 4 3	104.25	1486	1493	4 1 4	110.37	1651	1746
6 2 -4	104.28	760	759	4 3 -6	110.80	135	126
4 5 -1	104.30	784	779	2 3 5	110.95	77	70
1 1 6	104.45	884	873	5 4 -4	110.98	1597	1458
5 2 2	104.57	3578	3543	5 2 -6	111.06	750	687
1 3 -6	104.59	30	30	1 1 -7	111.17	61	57
4 5 -2	104.59	620	614	3 1 5	111.64	1384	1473
2 6 -1	104.66	476	472	4 0 -7	111.73	2	3
0 6 2	104.80	1026	1008	1 6 -3	111.84	79	84
5 4 -3	104.84	219	214	5 0 3	112.13	512	490
3 3 -6	104.88	4099	4000	1 5 4	112.14	566	540

h k l	2θ *(calc)*	I_{hkl} *(calc)*	I_{hkl} *(obs)*	*h k l*	2θ *(calc)*	I_{hkl} *(calc)*	I_{hkl} *(obs)*
1 4 5	112.24	542	500	3 6 -3	120.15	43	46
6 2 -5	112.74	498	496	5 2 3	120.21	45	49
7 0 -2	112.99	499	518	5 0 -7	120.77	1725	1658
7 0 -3	113.07	989	1031	5 5 -1	120.90	80	76
3 6 -1	113.07	430	448	3 4 4	120.99	1130	1062
4 1 -7	113.69	892	930	7 2 -2	121.13	2608	2461
0 6 3	113.75	560	581	3 6 1	121.14	7	7
6 3 -4	113.87	310	317	5 3 -6	121.15	259	245
2 6 -3	113.91	466	475	6 0 2	121.20	756	717
2 2 -7	113.93	56	57	7 2 -3	121.21	447	424
5 1 3	114.10	4000	3947	5 4 -5	121.25	706	673
5 3 2	114.17	440	429	6 4 -2	121.51	251	247
4 5 1	114.45	0	0	0 5 5	121.77	33	34
3 6 -2	114.68	4953	4648	3 5 3	122.04	1736	1731
3 2 -7	114.79	106	100	4 4 3	122.16	3	3
7 1 -2	114.97	191	180	5 5 -3	122.71	341	325
7 1 -3	115.05	1746	1649	5 1 -7	122.90	36	35
3 6 0	115.15	736	700	6 3 -5	122.99	1829	1823
6 2 1	115.52	2433	2411	6 4 -3	123.01	608	608
6 3 0	115.73	548	559	6 1 2	123.35	1	2
5 4 1	115.97	55	58	2 5 4	123.79	1689	1769
4 5 -4	116.00	660	696	1 6 -4	123.88	3377	3383
2 0 6	116.04	1083	1147	6 4 -1	124.02	3031	2912
4 2 4	116.29	748	810	2 3 -7	124.30	863	839
2 4 -6	116.33	319	347	7 0 0	124.40	100	98
0 0 7	116.34	1158	1260	2 2 6	124.42	1277	1250
2 5 -5	116.46	199	218	0 4 6	124.49	5	5
7 0 -1	116.63	2803	2992	2 6 -4	124.73	5	5
7 0 -4	116.86	743	779	0 2 7	124.76	72	71
1 5 -5	117.01	276	288	7 0 -5	124.81	1	1
1 2 -7	117.13	84	88	7 2 -1	125.07	862	830
6 0 -6	117.32	0	0	4 4 -6	125.19	1395	1324
3 2 5	117.62	2486	2519	3 3 -7	125.25	477	449
2 6 2	117.82	1063	1084	0 7 1	125.29	269	252
2 1 6	118.07	456	471	7 2 -4	125.33	1	1
1 4 -6	118.23	562	575	2 4 5	125.36	77	72
0 1 7	118.38	35	35	1 7 0	125.47	19	18
3 4 -6	118.55	710	684	6 2 -6	125.82	69	66
7 1 -1	118.68	2	2	4 5 2	125.86	40	39
7 1 -4	118.91	1551	1464	5 5 0	126.04	2119	2063
6 1 -6	119.38	8772	8600	1 7 -1	126.07	2505	2439
4 2 -7	119.78	1761	1816	6 3 1	126.07	1003	977
1 6 3	119.82	585	608	4 6 -1	126.48	1890	1820
5 5 -2	119.84	158	165	7 1 0	126.62	27	26
3 5 -5	120.06	1420	1528	4 6 -2	126.82	622	630
1 3 6	120.15	1156	1252	4 3 4	126.92	45	47

h k l	2θ *(calc)*	I_{hkl} *(calc)*	I_{hkl} *(obs)*	*h k l*	2θ *(calc)*	I_{hkl} *(calc)*	I_{hkl} *(obs)*
7 1 -5	127.05	1490	1647	7 2 -5	134.20	76	75
0 6 4	127.51	45	66	3 1 -8	134.72	137	141
1 3 -7	127.87	27	44	2 7 -2	135.26	190	197
4 5 -5	128.32	259	343	2 1 -8	135.31	2606	2695
3 3 5	128.43	116	143	6 0 -7	135.78	3231	3266
1 0 7	128.44	740	904	5 1 4	135.96	615	621
6 4 -4	128.73	1559	1650	5 5 1	136.23	4	4
1 7 1	129.09	690	694	2 3 6	136.32	1409	1407
5 4 2	129.09	903	907	1 4 6	136.33	1275	1273
5 2 -7	129.63	3055	3135	3 0 6	136.37	6349	6324
5 5 -4	129.96	239	243	1 6 4	136.41	4150	4120
6 2 2	130.12	2677	2690	2 5 -6	136.70	35	34
3 6 -4	130.23	1102	1093	0 3 7	136.72	3082	2991
4 6 0	130.43	6	6	4 0 -8	136.77	236	228
1 1 7	130.79	6619	6370	7 3 -1	137.10	399	387
4 3 -7	130.89	288	280	7 3 -4	137.40	668	661
6 4 0	130.94	98	96	5 4 -6	137.59	75	75
2 6 3	130.97	1	1	1 7 2	137.71	24	24
1 7 -2	131.02	34	33	7 0 1	137.77	7526	7551
5 3 3	131.38	46	48	6 3 -6	138.01	12787	12853
1 5 5	131.51	1441	1531	2 7 1	138.35	26	27
4 6 -3	131.54	2	2	1 2 7	138.42	176	179
2 7 -1	131.58	1781	1900	6 1 -7	138.44	926	943
4 0 5	131.68	156	166	7 0 -6	138.48	11	11
0 7 2	131.77	402	428	1 0 -8	138.63	896	919
3 6 2	131.91	2100	2214	3 1 6	139.06	1007	1028
3 0 -8	132.23	6379	6464	1 5 -6	139.22	3202	3258
7 3 -2	132.44	1415	1396	4 1 -8	139.48	697	715
2 7 0	132.53	127	124	4 6 1	139.59	1848	1912
7 3 -3	132.54	3902	3809	3 5 -6	139.66	18	19
2 0 -8	132.79	6112	5780	6 4 -5	139.96	13	14
5 0 4	133.41	664	571	7 1 1	140.53	675	791
7 2 0	133.73	61	55	7 1 -6	141.29	650	831
4 1 5	134.16	8928	8813	1 1 -8	141.45	1737	2281

APPENDIX II

Observed and Calculated Neutron Diffraction Intensities for $DSbO_3.0.81D_2O$

h k l	2θ *(calc)*	I_{hkl} *(calc)*	I_{hkl} *(obs)*	*h k l*	2θ *(calc)*	I_{hkl} *(calc)*	I_{hkl} *(obs)*
3 1 0	30.58	4494	4567	6 4 0	73.99	24	22
1 3 0	30.58	141	143	4 6 0	73.99	1420	1269
2 2 2	33.58	5	0	6 3 3	75.64	2590	2654
2 3 1	36.36	242	307	2 7 1	75.64	7	7
3 2 1	36.36	11	14	7 2 1	75.64	0	0
4 0 0	38.98	2346	2429	5 5 2	75.64	2716	2784
4 1 1	41.45	1509	1537	4 6 2	77.28	1234	1286
3 3 0	41.45	20553	20932	6 4 2	77.28	299	311
4 2 0	43.81	1415	1419	3 7 0	78.92	8	8
2 4 0	43.81	1777	1782	7 3 0	78.92	2183	2027
3 3 2	46.07	22	0	3 7 2	82.16	329	316
4 2 2	48.24	3453	3340	6 5 1	82.16	1436	1379
1 5 0	50.35	1	0	7 3 2	82.16	496	477
3 4 1	50.35	2482	2485	5 6 1	82.16	14	13
4 3 1	50.35	2909	2912	8 0 0	83.77	1513	1389
5 1 0	50.35	969	970	7 4 1	85.37	1929	1859
2 5 1	54.38	24	23	5 5 4	85.37	4	4
5 2 1	54.38	678	661	4 7 1	85.37	1522	1467
4 4 0	56.32	426	296	8 1 1	85.37	53	51
4 3 3	58.22	1405	1323	6 4 4	86.97	81	0
5 3 0	58.22	438	413	8 2 0	86.97	6	0
3 5 0	58.22	137	129	2 8 0	86.97	2	0
6 0 0	60.08	2751	2534	5 6 3	88.57	709	728
4 4 2	60.08	343	316	6 5 3	88.57	36	37
3 5 2	61.91	1059	1130	6 6 0	90.17	5122	4942
6 1 1	61.91	1416	1512	8 2 2	90.17	117	112
5 3 2	61.91	458	489	4 7 3	91.76	8	8
2 6 0	63.70	790	804	5 7 0	91.76	1190	1225
6 2 0	63.70	409	417	7 5 0	91.76	977	1005
5 4 1	65.47	148	157	7 4 3	91.76	319	328
4 5 1	65.47	215	228	3 8 1	91.76	305	314
6 2 2	67.21	360	120	8 3 1	91.76	20	20
6 3 1	68.93	303	350	6 6 2	93.36	146	160
3 6 1	68.93	74	85	7 5 2	94.96	41	70
4 4 4	70.63	5436	5471	5 7 2	94.96	38	66
1 7 0	72.32	2871	2864	4 8 0	96.57	563	559
4 5 3	72.32	3556	3548	8 4 0	96.57	2	2
7 1 0	72.32	31	31	8 3 3	98.18	662	650
5 5 0	72.32	298	298	9 1 0	98.18	1330	1305
5 4 3	72.32	1292	1289	1 9 0	98.18	460	451

h k l	2θ *(calc)*	I_{hkl} *(calc)*	I_{hkl} *(obs)*	*h k l*	2θ *(calc)*	I_{hkl} *(calc)*	I_{hkl} *(obs)*
8 4 2	99.80	16	19	5 9 0	118.48	2	2
4 8 2	99.80	44	52	9 5 0	118.48	1490	1472
6 5 5	101.42	25	26	10 2 2	120.32	8	10
7 6 1	101.42	1082	1138	6 6 6	120.32	495	576
6 7 1	101.42	204	214	9 5 2	122.19	40	42
2 9 1	101.42	239	251	10 3 1	122.19	1488	1533
9 2 1	101.42	4	4	3 10 1	122.19	1447	1491
6 6 4	103.06	260	238	7 6 5	122.19	1169	1205
5 7 4	104.70	40	38	5 9 2	122.19	295	304
7 5 4	104.70	136	128	6 7 5	122.19	625	644
5 8 1	104.70	427	403	7 7 4	126.05	4241	4410
9 3 0	104.70	197	186	8 7 1	126.05	4	4
8 5 1	104.70	371	350	7 8 1	126.05	115	120
3 9 0	104.70	260	245	8 5 5	126.05	524	544
3 9 2	108.03	672	781	8 6 4	128.05	597	601
6 7 3	108.03	8	9	6 8 4	128.05	82	83
7 6 3	108.08	0	0	4 10 0	128.05	176	177
9 3 2	108.03	13	15	10 4 0	128.05	68	69
8 4 4	109.72	935	988	10 3 3	130.11	1017	1033
7 7 0	111.43	236	262	6 9 1	130.11	4779	4855
8 5 3	111.43	660	731	9 6 1	130.11	83	84
4 9 1	111.43	321	356	4 10 2	132.23	2327	2452
5 8 3	111.43	10	11	10 4 2	132.23	3029	3191
9 4 1	111.43	816	905	9 5 4	134.43	791	808
8 6 0	113.16	446	419	5 9 4	134.43	1965	2007
10 0 0	113.16	628	590	8 7 3	134.43	113	115
6 8 0	113.16	13	12	7 8 3	134.43	595	608
7 7 2	114.91	548	616	11 1 0	134.43	44	45
10 1 1	114.90	86	97	1 11 0	134.43	1	1
8 6 2	116.68	114	118	5 10 1	139.10	120	117
6 8 2	116.68	315	327	9 6 3	139.10	234	226
2 10 0	116.68	1277	1324	6 9 3	139.10	377	365
10 2 0	116.68	349	361	11 2 1	139.10	178	172
4 9 3	118.48	808	798	10 5 1	139.10	32	31
9 4 3	118.48	774	765	2 11 1	139.10	210	204